2017

Experimental studies on the dynamics of in-flight and impacting water droplets pertinent to aircraft icing phenomena

Haixing Li
Iowa State University

Experimental studies on the dynamics of in-flight and impacting water droplets pertinent to aircraft icing phenomena

by

Haixing Li

A dissertation submitted to the graduate faculty

in partial fulfillment of the requirements for the degree of

DOCTOR OF PHILOSOPHY

Major: Aerospace Engineering

Program of Study Committee:
Hui Hu, Major Professor
Anupam Sharma
Thomas Ward III
Alberto Passalacqua
Xinwei Wang

Iowa State University
Ames, Iowa
2017

DEDICATION

I would like to dedicate this dissertation to my foster mother, Sanying Yao, who just went to heaven in this June. Since I was in the graduating process, I could not go back home to accompany her in the last period of her life. Her support is the power for me to complete this work.

TABLE OF CONTENTS

LIST OF FIGURES

LIST OF TABLES

ACKNOWLEDGEMENTS

I would like to express my sincere gratitude and appreciation to my major advisors, Dr. Hui Hu, whose expertise, enthusiasm, and research attitude have been influencing me during my entire Ph.D. period. Without his generous guidance and support, this dissertation would not have been possible. I consider it a great honor to work with these prominent professors in the past four years.

My heartily appreciation also goes to my committee members, Dr. Anupam Sharma, Dr. Thomas Ward III, Dr. Alberto Passalacqua, and Dr. Xinwei Wang,for their generous help during my research. I would also like to thank them for evaluating my research work and giving me many insightful comments.

I am grateful to all the staff members in the Department of Aerospace Engineering, especially former and present department sectaries, Ms. Gayle Fay and Ms. Jacqueline Kester for their help on all the paperwork and many other important things.

I would like to thank Dr. Rye Waldman, and Dr. Kai Zhang for their valuable help in completing the experiments and thesis writing. I also want to thank Dr. Wenwu Zhou, Dr. Yang Liu, Mr. Morteza Khosravi, Mr. Zhe Ning, Mr. Pavithra Premaratne, Mr. Linkai Li, Mr. Hao Guo and Mr. Liqun Ma for their help and the joys shared in the past four years.

I am also hugely grateful to my father and mother, Kang Li, and Chunmei Li, who have given me this opportunity to study abroad. I cannot become who I am without their unconditional love and support throughout my life.

Finally, my deepest appreciation is reserved for my fiancee, Yan Cao, who has always been supporting me during my Ph.D. study. With her love and encouragement, I have been able to overcome many difficulties in my life.

ABSTRACT

Aircraft icing is widely recognized as a significant hazard to aircraft operations in cold weather. When an aircraft or rotorcraft flies in a cold climate, some of the super-cooled water droplet would impact and freeze on the exposed aircraft surfaces to form ice shapes, which can degrade the aerodynamic performance of an airplane significantly by decreasing lift while increasing drag, and even lead to the aircraft crash. In the present study, a series of experimental investigations were conducted to investigate dynamics and thermodynamics of in-flight and impinging water droplets in order to elucidate the underlying physics of the important micro-physical process pertinent to aircraft icing phenomena.

A novel lifetime-based molecular tagging thermometry technique (MTT) is developed to achieve simultaneous measurements of droplet size, flying velocity and transient temperature of in-flight water droplets to characterize the dynamic and thermodynamic behaviors of the micro-sized in-flight droplets pertinent to aircraft icing phenomena. By using high-speed imaging and infrared thermal imaging techniques, a comprehensive experimental study was conducted to quantify the unsteady heat transfer and phase changing processes as water droplets impinging onto frozen cold surfaces under different test conditions (i.e., with different Weber numbers, Reynolds numbers, and impact angles of the impinging droplets, different temperature, hydrophobicity and roughness of the test plates) to simulate the scenario of super-cooled water droplets impinging onto the frozen cold wing surfaces. A novel digital image projector (DIP)

technique was also developed to achieve time-resolved film thickness measurements to quantify the dynamic impinging process of water droplets (i.e., droplet impact, rebounding, splashing and freezing process). An impact droplet maximum spreading diameter model and a damped harmonic oscillator model were proposed based on precise measurement of the impact droplet 3D shape. A better understanding of the important micro-physical processes pertinent to aircraft icing phenomena would lead to better ice accretion models for more accurate prediction of ice formation and accretion on aircraft wings as well as to develop more effective and robust anti-/de-icing strategies for safer and more efficient operation of aircraft in cold weather.

CHAPTER 1
GENERAL INTRODUCTION

1.1 Background and Motivation

Aircraft icing is widely recognized as a significant hazard to aircraft operations in cold weather. When an aircraft or rotorcraft flies in certain climates, some of the supercooled droplets in the air would impact and freeze on the exposed aircraft surfaces and form ice shapes. Ice may accumulate on every exposed frontal surface of an airplane, not only on the wing, propeller and windshield, but also on the antennas, vents, intakes, and cowlings. Icing accumulation can degrade the aerodynamic performance of an airplane significantly by decreasing lift while increasing drag. In moderate to severe conditions, an airplane could become so iced up that continued flight is impossible. The airplane may stall at much higher speeds and lower angles of attack than normal. It could roll or pitch uncontrollably, and recovery may be impossible. Ice can also cause engine stoppage by either icing up the carburetor or, in the case of a fuel-injected engine, blocking the engine's air source. The importance of proper ice control for aircraft operation in cold climate was highlighted by many aircraft crashes in recent years like the ATR-72 aircraft of American Eagle flight crashed in Roselawn, Indiana due to ice buildup on its wings killing all 66 people aboard on October 31, 1994. After investigation, it was found that the aircraft encountered the supercooled large droplets (SLD) icing environment, which didn't be defined in Appendix C of Part 25 of Federal Aviation Regulations (FAR25 Appendix C), and the aircraft crashed for the abnormal icing on airfoils[1]. The study of atmosphere shows that the abnormal icing condition wasn't defined in the FAR 25 Appendix C[2], thus

the deicer equipment designed based on the FAR 25 Appendix C is not suitable for the abnormal icing environment. For expanding the airworthiness regulations application scope of icing environment, it is important and necessary to elucidate the underlying physics of the abnormal icing.

As the basis of the aircraft icing phenomenon, the droplet impact and icing is a complicated process relating to a series fluid dynamic theories and thermodynamics theories. To elucidate the underlying physics, a series of investigation were desired.

1.1.1 In-flight droplet temperature, velocity and size measurement

The temperature, impact velocity and size of the droplet can severely influence the droplet impact and icing process, thus, a technique that can simultaneously measure the droplet temperature, velocity and size before impacting is desired.

It is well known that both fluorescence and phosphorescence are molecular photoluminescence phenomena. Compared with fluorescence, which typically has a lifetime on the of order nanoseconds, phosphorescence can last as long as microseconds, even minutes. Since emission intensity is a function of the temperature for some substances, both fluorescence and phosphorescence of tracer molecules may be used for temperature measurements. While fluorescence (LIF) techniques have been widely used for temperature measurements of liquid droplets in spray flows [3–5], Laser-induced phosphorescence (LIP) techniques have also been suggested recently to conduct temperature measurements of ‘‘in-flight” or levitated liquid droplets [6,7]. Compared with LIF-based thermometry techniques, the relatively long lifetime of LIP has been used to prevent interference from scattered/reflected light and any fluorescence from other

substances (such as from solid surfaces for the near surface measurements) that are present in the measurement area, by simply putting a small time delay between the laser excitation pulse and the starting time for phosphorescence image acquisitions [8]. Furthermore, LIP was found to be much more sensitive to temperature compared with LIF [6,7], which is favorable for the accurate temperature measurements of small liquid droplets.

According to quantum theory [9], with unsaturated laser excitation, the intensity of a photoluminescence process (either fluorescence or phosphorescence) decays exponentially. For simplicity, only a signal-exponential process is considered here. As described in Hu and Koochesfahani (2006; 2011), for a diluted solution and unsaturated laser excitation, the collected phosphorescence signal (S_p) by using a gated imaging detector with integration starting at a delay time t_o after the laser excitation pulse and a gate period of δt can be given by:

$$S_p = AI_i C\varepsilon \Phi_p \left(1 - e^{-\delta t/\tau}\right) e^{-t_o/\tau} \tag{1.1}$$

where A is a parameter representing the detection collection efficiency, I_i is the local incident laser intensity, C is the concentration of the phosphorescent dye (the tagged molecular tracer), ε is the absorption coefficient and Φ_p is the phosphorescence quantum efficiency. The emission lifetime τ refers to the time at which the intensity drops to 37% (i.e., 1/e) of the initial intensity. For an excited state, the deactivation processes may involve both radiative and nonradioactive pathways and the lifetime of the photoluminescence process, τ, is determined by the sum of all the deactivation rates, i.e. $\tau^{-1} = k_r + k_{nr}$, where k_r and k_{nr} are the radiative and non-radiative rate constants, respectively. According to photoluminescence kinetics, the non-radiative rate constant is, in general,

temperature dependent (Ferraudi, 1988), and the resulting temperature dependence of the phosphorescence lifetime is the basis of the present technique for temperature measurement.

It should also be noted that the absorption coefficient ε, and quantum yield Φ_p are usually temperature dependent in general [12], resulting in a temperature-dependent phosphorescence signal (S_p). Thus, in principle, the collected phosphorescence signal (S_p) may be used to measure temperature if the incident laser intensity and the concentration of the phosphorescent dye remain constant (or are known) in the region of interest.

As shown in Equation (1.1), the collected phosphorescence signal (S_p) is also a function of the incident laser intensity (I_i) and the concentration of the phosphorescent dye (C), thus, the spatial and temporal variations of the incident laser intensity and the non-uniformity of the phosphorescent dye (such as due to photo bleaching and/or the changes of the dye concentration in liquid droplets during evaporation process) in the region of interest would have to be corrected separately in order to derive quantitative temperature data from the acquired phosphorescence images. In practice, however, it is very difficult, if not impossible, to ensure a non-varying incident laser intensity distribution and a constant dye concentration within liquid droplets due to evaporation process, which may cause significant errors in the temperature measurements. To overcome this problem, Hu and Koochesfahani (2003; 2006; 2011) developed a lifetime-based Molecular Tagging Thermometry (MTT) technique， which can eliminate the effects of incident laser intensity and concentration of phosphorescent dye on temperature measurements effectively.

$$\tau = \frac{\Delta t}{\ln(S_1 / S_2)} \tag{1.2}$$

Where τ is the phosphorescence lifetime, Δt is the time delay of two successive image, and S_1/S_2 is the phosphorescence intensity ratio.

As described in Hu and Koochesfahani (2006, 2011) and Hu et al (2010), since the photoluminescence lifetime is temperature dependent for some molecular tracers, with the conditions of diluted solution and unsatuated laser exciation, the temperature distribution in a fluid flow can be derived from the distribution of the intensity ratio of the two photoluminescence images acquired after the same laser excitation pulse. For a given molecular tracer and fixed Δt value, Equation (1.2) defines a unique relation between phosphorescence intensity ratio (R) and fluid temperature T, which can be used for thermometry as long as the temperature dependence of phosphorescence lifetime of the molecular tracers is known. This ratiometric approach eliminates the effects of any temporal and spatial variations in the incident laser intensity (due to pulse-to-pulse laser energy variations) and non-uniformity of the dye concentration (e.g., due to photobleaching or concentration change of the tracer molecules within liquid droplets due to evaporation at a high temperature environment).

In addition to measuring the transient temperature of liquid droplets, droplet size and flying velocity of the in-flight droplets can also be determined simultaneously based on the acquired phosphorescence image pair. With a pre-calibrated scale ratio between the image plane and the object plane for the phosphorescence image acquisition, the size of the in-flight droplets can be determined quantitatively by measuring the dimension of the

droplets in the acquired phosphorescence images via an image processing procedure. Furthermore, a particle-tracking algorithm can be used to determine the displacement vectors of the in-flight droplets between the two phosphorescence image acquisitions. Since the time delay Δt between the two image acquisition is known for a specific experiment, the flying velocities of the in-flight droplets can also be estimated based on the measured displacement vectors of the in-flight droplets between the two phosphorescence image acquisitions.

The objective of present study is to develop a molecular tagging technique for achieving simultaneous measurements of droplet size, flying velocity and transient temperature of in-flight liquid droplets.

1.1.2 Droplet impact and icing

In recent year, the frequently used de-icing systems on aircraft are based on two techniques, the mechanical technique, as the de-icing boots, and the other one is the heating technique, as the electrical heater mats. While both of these two ways would expand the power from aircraft, a passive de-icing technique which can help reduce the ice accretion on aircraft is desired. The recent researches on superhydrophobic surfaces demonstrated that the superhydrophobic coatings have ice phobic properties [16], as the droplets can bounce off of cold superhydrophobic surfaces without freezing [17] and the superhydrophobicity directly implies anti-icing functionality [18]. Therefore, utilizing the superhydrohopbic surfaces could be a reasonable way to manage the water runback phenomenon and decrease or eliminate the back-part icing on airfoil. Superhydrophobic surfaces have been extensively studied because they exhibit a number of interesting

properties such as extremely high static contact angles (e.g., >150˚), small contact angle hysteresis, droplets rolling off at shallow surface angles, and droplets bouncing on impact [19–23]. These properties of superhydrophobic surfaces leads to self-cleaning behavior, whereby water droplets quickly roll off the surface and carry with them any other contaminates-including other droplets-they encounter. The superhydrophobicity of the surface results from a combination of chemical hydrophobicity with a micro or nano textured surface. The structure of the surface plays an important role both in the wettability of the surface and in the ability of the surface to resist ice accretion [16]. Since the superhydrobic surface demonstrates ice phobic properties, an investigation of the surface's influence to droplet impact and icing process is desired.

Droplet impact, such as the fingering of an inkblot or a coffee stain, is familiar to everyone. Droplet impact, which has been studied extensively since 1876[24], has a very wide range of applications, including atomization processes[25], raindrop dynamics[26], inkjet printing[27], blood pattern and drop trajectories[28], and micro-fabrication[29]. While it also involves most of the key issues of surface flows, droplet impact is characteristic of multiphase flows[30]. In the previous studies, a typical droplet impact process usually includes an early contact stage that considers the central bubble[31] and skating on air[32], a spreading or splash stage[33,34], and a receding or rebounding stage[35,36]. While most of the previous studies were concentrated on the air layer radius or thickness[12,13], maximum spreading radius[35,36,37], minimal thickness of the water layer[38], and whether the impacting droplet would splash[34,39] or rebounding[35,36], very few studies considered the droplet shape evolution during the impact process. Since the droplet shape evolution during the impact

process can directly influence the final shape of the impact droplet under icing conditions[40], e.g. droplet impact and icing on the airfoil, and then influence the impact surface for the subsequent droplet, the accurate measurement of the droplet shape or the film thickness of the impact droplet could help reveal the underlying physics and improve the theoretical physics models used in the airfoil icing.

The most frequently-used method to measure the droplet shape is using high speed camera to record the impact process from the side view[41,42]. When a droplet normally impacts on a flat surface, it is acceptant to assume that the impact droplet is axially symmetric, and a 2-D profile can represent the real shape of the droplet. However, if the impact direction was not perpendicular to the impact surface, or the surface was not flat enough, then the real droplet shape during the impact process would be much more complicated, and a 2-D profile cannot represent of the real shape[41]. Moreover, in some moments during the droplet impact process, especially during the droplet spreading stage, the central region of the droplet is lower than the outer region[43], and thus the central region information is blocked by the outer region, which leads to the failure of obtaining droplet shape information by side view. A method which can record real 3-D shape information of impact droplet is needed. At present, there are several techniques can collect the thickness information of objects, e.g., using multi-transducer ultrasonic pulse-echo technique was used to measure the film flow thickness[44], and using space-time-resolved Fourier transform profilometry technique (FTP) to measure the 3-D shape of objective[45,46]. The ultrasonic pulse-echo technique can just do point thickness measurement, while the FTP technique need several different successive fringe patterns to achieve high accuracy

measurement, which leads to the limitation of the time resolution. Since the droplet impact process, especially the spreading stage is quite fast and needs high time resolution 3-D shape information to analyze the dynamics during the impact process, a method which can achieve both thickness measurement of the full droplet and high time resolution is needed.

As a very important parameter during droplet impact process, the maximum spreading diameter can directly influence the ice collection efficient on the aircraft since it dominates the ice area of the impact droplet. To predict the maximum spreading diameter of the impact droplet, a large number of different models have been proposed for the maximum spreading factor β_{max}. For example, Scheller & Bousfield[47] proposed an empirical law based on experimental results; Pasandideh-Fard et al.[48] developed a spreading factor model based on detailed energy balance between the initial droplet prior impact and the droplet at the maximum spreading; Ukiwe & Kwok[49] extended the above model with an approximated static contact angle and a cylinder assumption; Clanet et al.[50] came up with a spreading factor scale by considering the mass balance using the impact capillary length; Roisman[51] and Eggers et al.[52] raised the spreading factors using dynamical model for the spreading of the droplet involving a viscous boundary layer. Comparing with those spreading factor models based on mass balance or using dynamical model, the spreading factor models based on detailed energy balance give explicit values, while most of the others give scales and need more conditions and analyses to obtain the explicit values. However, those spreading factors based on the energy balance need more accurate experimental data instead of assumptions to improve the prediction accuracy. For example, Pasandideh-Fard et al.[48] assumed that the shape of the droplet at the maximum spreading

was a circle, while Ukiwe & Kwok[49] assumed it as a cylinder, while the real shape of the droplet at the maximum spreading was much more complex than just a circle or cylinder, especially under low Reynolds and Weber numbers impacting conditions. To increase the prediction accuracy, a method is needed to precisely measure the shape of the impact droplet at the maximum spreading.

The droplet impact and icing process is a combination of dynamic and thermodynamic process, thus, a high precise prediction of droplet impact dynamics as the flatness factor during the oscillating stage of a droplet can help increase the prediction accuracy of aircraft icing. When predicting the dynamic droplet behavior, the computational modeling is an attractive means, however, the process is challenging as it requires accurate tracking and prediction of the continuously deforming gas-liquid interface. Moreover, the contact line velocity along with impact substrate and liquid properties has not been universally successful in achieving the level of accuracy that is needed for simulations. Thus, a simple model that can predict the dynamic behaviors during oscillating stage is desirable. A few previous studies already proposed some models, for example, for example, Manglik developed a damped harmonic system model to predict the dimensionless spread factor β $(= \mathrm{D}/D_0)$ and flatness factor δ $(= \mathrm{h}/D_0)$, where D and h are the droplet diameter and the height of upper surface central point of the droplet during the droplet post-impact process, and D_0 is the initial diameter of the droplet before impacting. In this damped harmonic system model, the damping coefficient and frequency of the oscillation were calculated based on semi-empirical models derived from measured

experimental results, and the Reynolds number and Weber number as in equation 6.1 and 6.2 were set as the variables in the semi-empirical models.

The objectives of the present study are:

1. Investigate the superhydrophobic surface's influence to the droplet impact and icing process;

2. Develop a method to obtain the time resolved 3D shape of impacting droplets during the whole impact process to quantify the dynamic impacting process of droplets;

3. Propose a droplet maximum spreading diameter model based on energy conservation during the impact process;

4. Analyze the droplet dynamics during the oscillating stage, and propose a model that can predict the flatness factor of the droplet during the oscillating stage.

1.2 Thesis Organization

The dissertation includes seven chapters in total. A general introduction (Chapter 1) is given at the beginning, and the conclusions and future work are provided as the last chapter of the dissertation (Chapter 7).

Chapter 2 describes the development of the molecular tagging technique, which is used to be used in the measurements of in-flight droplet temperature, flying velocity and size. To validate the accuracy of the temperature measurement, the results measured by the lift time based molecular tagging technique were compared with the predicted results.

Chapter 3 presents an experimental investigation of the droplet impact and icing on normal (hydrophilic surface) and superhydrophobic surface. A high-speed imaging

technique was used to recording the droplet profile variation, while a thermometry imaging technique was implemented to achieve temporally and spatially resolved temperature distribution measurements of the droplet during the impact process. The comparison of the dynamics and temperature of the droplets impacting on these two surfaces were discussed in detail.

Chapter 4 introduces the development of the digital image projector (DIP) technique to measure the 3D shape of the impact droplet during the impact process. Based on the measured results, the droplet impact process can be divided into three distinct stages: spreading stage, receding stage, and oscillating stage. The measured results helped validate the models proposed in previous studies. By comparing the droplet shape evolution under different impact velocities, the dynamics of droplet impact under different Weber numbers or Reynolds numbers was analyzed in detail.

Chapter 5 described a revised impact droplet maximum spreading diameter model based on detailed energy conservation during the impact process by precisely measure the droplet 3D shape. A combination of digital image technique and “side-view” technique helped precisely measure the 3D shape of the droplet when the droplet reaches the maximum spreading diameter. To validate the prediction precise, the predicted results were compared with the experimental data in present study and that in several previous researches, meanwhile, several prediction models proposed in previous studies were analyzed as well.

Chapter 6 presented an analysis of the droplet dynamics during the oscillating stage, and introduce the development of a damped harmonic oscillator model that can predict the

flatness factor of the droplet during the oscillating stage. To validate the prediction accuracy, the predicted results of the model were compared with the experimental results in the present study.

References

[1] Report, A. A., "National Transportation Safety in-Flight Icing Encounter and Loss of Control," vol. 1, 1994.

[2] Cober, S. G., Isaac, G. A., and Ratvasky, T. P., "Assessment of aircraft icing conditions observed during AIRS," *AIAA 40th Aerospace Sciences Meeting & Exhibit, Reno, NE*, 2002.

[3] Zhang, Y., Zhang, G., Xu, M., and Wang, J., "Droplet temperature measurement based on 2-color laser-induced exciplex fluorescence," *Experiments in Fluids*, vol. 54, Jul. 2013, p. 1583.

[4] Castanet, G., Lavieille, P., Lemoine, F., Lebouché, M., Atthasit, A., Biscos, Y., and Lavergne, G., "Energetic budget on an evaporating monodisperse droplet stream using combined optical methods," *International Journal of Heat and Mass Transfer*, vol. 45, Dec. 2002, pp. 5053–5067.

[5] Lavieille, P., Lemoine, F., Lavergne, G., and Lebouché, M., "Evaporating and combusting droplet temperature measurements using two-color laser-induced fluorescence," *Experiments in Fluids*, vol. 31, Jul. 2001, pp. 45–55.

[6] Omrane, A., Juhlin, G., Ossler, F., and Aldén, M., "Temperature measurements of single droplets by use of laser-induced phosphorescence," *Applied optics*, vol. 43, 2004, pp. 3523–3529.

[7] Omrane, A., Santesson, S., Alden, M., and Nilsson, S., "Laser techniques in acoustically levitated micro droplets.," *Lab on a chip*, vol. 4, Aug. 2004, pp. 287–91.

[8] Hu, H., and Huang, D., "Simultaneous measurements of droplet size and transient temperature within surface water droplets," *AIAA journal*, vol. 47, 2009, pp. 813–820.

[9] Ramamurthy, V., and Schanze, K. S., *Organic and inorganic photochemistry*, 1998.

[10] Hu, H., and Koochesfahani, M. M., "Thermal effects on the wake of a heated circular cylinder operating in mixed convection regime," *Journal of Fluid Mechanics*, vol. 685, Oct. 2011, pp. 235–270.

[11] Hu, H., and Koochesfahani, M. M. M., "Molecular tagging velocimetry and thermometry and its application to the wake of a heated circular cylinder," *Measurement Science and Technology*, vol. 17, Jun. 2006, pp. 1269–1281.

[12] Kim, H. J., Kihm, K. D., and Allen, J. S., "Examination of ratiometric laser induced fluorescence thermometry for microscale spatial measurement resolution," *International Journal of Heat and Mass Transfer*, vol. 46, Oct. 2003, pp. 3967–3974.

[13] Hu, H., and Koochesfahani, M., *A Novel Technique for Quantitative Temperature Mapping in Liquid by Measuring the Lifetime of Laser Induced Phosphorescence*, 2003.

[14] Hu, H., and Koochesfahani, M., "Molecular tagging velocimetry and thermometry and its application to the wake of a heated circular cylinder," *Measurement Science and Technology*, vol. 17, 2006, pp. 1269–1281.

[15] Hu, H., Jin, Z., and Nocera, D., "Experimental investigations of micro-scale flow and heat transfer phenomena by using molecular tagging techniques," *Measurement Science and Technology*, vol. 21, 2010, p. 085401 (14pp).

[16] Cao, L., Jones, A. K., Sikka, V. K., Wu, J., and Gao, D., "Anti-Icing superhydrophobic coatings," *Langmuir*, vol. 25, 2009, pp. 12444–12448.

[17] Maitra, T., Tiwari, M. K., Antonini, C., Schoch, P., Jung, S., Eberle, P., and Poulikakos, D., "On the nanoengineering of superhydrophobic and impalement resistant surface textures below the freezing temperature (Supporting Material)," *Nano Letters*, vol. 14, 2014, pp. 172–182.

[18] Vorobyev, A. Y., and Guo, C., "Multifunctional surfaces produced by femtosecond laser pulses," *Journal of Applied Physics*, vol. 117, 2015, p. 033103.

[19] Antonini, C., Villa, F., and Marengo, M., "Oblique impacts of water drops onto hydrophobic and superhydrophobic surfaces: outcomes, timing, and rebound maps," *Experiments in Fluids*, vol. 55, 2014, p. 1713.

[20] Bartolo, D., Bouamrirene, F., Verneuil, É., Buguin, A., Silberzan, P., and Moulinet, S., "Bouncing or sticky droplets: Impalement transitions on superhydrophobic micropatterned surfaces," *Europhysics Letters (EPL)*, vol. 74, 2006, pp. 299–305.

[21] Blossey, R., “Self-cleaning surfaces--virtual realities.,” *Nature materials*, vol. 2, 2003, pp. 301–306.

[22] Dorrer, C., and Rühe, J., “Some thoughts on superhydrophobic wetting,” *Soft Matter*, vol. 5, 2009, p. 51.

[23] Miwa, M., Nakajima, A., Fujishima, A., Hashimoto, K., and Watanabe, T., “Effects of the surface roughness on sliding angles of water droplets on superhydrophobic surfaces,” *Langmuir*, vol. 16, 2000, pp. 5754–5760.

[24] Worthington, “On the forms assumed by drops of liquids falling vertically on a horizontal plate,” 1876, pp. 261–272.

[25] Eggers, J., and Villermaux, E., “Physics of liquid jets,” vol. 71, 2008.

[26] Planchon, O., “A Physical Model for the Action of Raindrop Erosion on Soil Microtopography,” vol. 74, 2010.

[27] Minemawari, H., Yamada, T., Matsui, H., Tsutsumi, J., Haas, S., Chiba, R., Kumai, R., and Hasegawa, T., “Inkjet printing of single-crystal films,” *Nature*, vol. 475, 2011, pp. 364–367.

[28] Attinger, D., Moore, C. B., Donaldson, A., and Stone, H. A., “Fluid dynamics topics in bloodstain pattern analysis : Comparative review and research opportunities,” 2013.

[29] Antkowiak, A., Audoly, B., and Josserand, C., “Instant fabrication and selection of folded structures using drop impact,” vol. I.

[30] Rein, M., “Phenomena of liquid drop impact on solid and liquid surfaces,” vol. 12, 1993, pp. 61–93.

[31] Engineering, M., Drive, E., and Engineering, E., “The air bubble entrapped under a drop impacting on a solid surface,” vol. 545, 2005, pp. 203–212.

[32] Street, G., and Street, G., “Air cushioning with a lubrication/inviscid balance,” vol. 482, 2003, pp. 291–318.

[33] Eggers, J., Fontelos, M. A., Josserand, C., Zaleski, S., Eggers, J., Fontelos, M. A., Josserand, C., and Zaleski, S., “Drop dynamics after impact on a solid wall : Theory and simulations Drop dynamics after impact on a solid wall : Theory and simulations,” vol. 062101, 2016.

[34] Chr. Mundo, M. Sommerfeld, C. T., “Droplet-Wall Collisions: Experimental Studies of the Deformation and Breakup Process,” vol. 21, 1995.

[35] Rioboo, R., Heat, E., and Sa, P., “Outcomes from a Drop Impact on Solid Surfaces,” 2001.

[36] Statistique, P., and Lhomond, R., “Retraction dynamics of aqueous drops upon impact on non-wetting surfaces,” vol. 545, 2005, pp. 329–338.

[37] Roisman, I. V, Berberović, E., Tropea, C., Roisman, I. V, Berberovi, E., and Tropea, C., “Inertia dominated drop collisions . I . On the universal flow in the lamella Inertia dominated drop collisions . I . On the universal flow in the lamella,” vol. 052103, 2016.

[38] Lagubeau, G., Fontelos, M. A., Josserand, C., Maurel, A., Pagneux, V., and Petitjeans, P., “Spreading dynamics of drop impacts,” 2012, pp. 50–60.

[39] Xu, L., Zhang, W. W., and Nagel, S. R., “Drop Splashing on a Dry Smooth Surface,” vol. 184505, 2005, pp. 1–4.

[40] Zhang, C., and Liu, H., “Effect of drop size on the impact thermodynamics for supercooled large droplet in aircraft icing Effect of drop size on the impact thermodynamics for supercooled large droplet in aircraft icing,” vol. 062107, 2016.

[41] Josserand, C., and Thoroddsen, S. T., “Drop Impact on a Solid Surface,” pp. 365–393.

[42] Bartolo, D., Josserand, C., and Bonn, D., “Singular Jets and Bubbles in Drop Impact,” vol. 124501, 2006, pp. 1–4.

[43] Li, H., Waldman, R. M., and Hu, H., “An Experimental Investigation on Unsteady Heat Transfer and Transient Icing Process upon Impingement of Water Droplets,” 2016, pp. 1–18.

[44] Liu, Y., Chen, W., Bond, L. J., and Hu, H., “An experimental study on the characteristics of wind-driven surface water film flows by using a multi-transducer ultrasonic pulse-echo technique An experimental study on the characteristics of wind-driven surface water film flows by using a multi-transducer ultrasonic pulse-echo technique,” vol. 012102, 2017.

[45] Hu, H., Wang, B., and Zhang, K., “Quantification of transient behavior of wind-driven surface droplet / rivulet flows using a digital fringe projection technique,” *Journal of Visualization*, 2015, pp. 705–718.

[46] Dai, J., Li, B., and Zhang, S., “High-quality fringe pattern generation using binary pattern optimization through symmetry and periodicity,” *Optics and Lasers in Engineering*, vol. 52, 2014, pp. 195–200.

[47] Scheller, B. L., and Bousfield, D. W., “Newtonian Drop Impact with a Solid Surface,” vol. 41, 1995, pp. 1357–1367.

[48] Fard, M. P., Qiao, Y. M., Chandra, S., Mostaghimi, J., Qiao, Y. M., Chandra, S., and Mostaghimi, J., “Capillary effects during droplet impact on a solid surface Capillary effects during droplet impact on a solid surface,” vol. 650, 1996.

[49] Ukiwe, C., and Kwok, D. Y., “On the Maximum Spreading Diameter of Impacting Droplets on Well-Prepared Solid Surfaces,” 2005, pp. 666–673.

[50] CLANET, C. S., BE´GUIN, C. D., RICHARD, D., and QU ´ ER ´E, D., “Maximal deformation of an impacting drop ´,” vol. 517, 2004, pp. 199–208.

[51] Roisman, I. V, and Roisman, I. V, “Inertia dominated drop collisions . II . An analytical solution of the Navier – Stokes equations for a spreading viscous film Inertia dominated drop collisions . II . An analytical solution of the Navier – Stokes equations for a spreading viscous film,” vol. 052104, 2010.

[52] Eggers, J., Fontelos, M. A., Josserand, C., and Zaleski, S., “Drop dynamics after impact on a solid wall : Theory and simulations,” 2010, pp. 1–13.

CHAPTER 2
SIMULTANEOUS MEASUREMENT OF SIZE, FLYING VELOCITY AND TRANSIENT TEMPERATURE OF IN-FLIGHT DROPLETS BY USING A MOLECULAR TAGGING TECHNIQUE

2.1 Introduction

The characterization of in-flight liquid droplets in spray flows is of great interests for a wide range of engineering applications, which include combustion, spray cooling, spray drying, and fire extinction. The heat and mass transfer processes from or to liquid droplets are important control variables in many of such applications. For examples, the process of breaking up or atomization of liquid fuel into droplets in the form of a fine spray plays a pivotal role in improving energy efficiency and suppressing pollutant formation for various gas turbines and internal combustion (IC) engines. A detailed definition of the dynamic and thermodynamic behaviors of in-flight fuel droplets is essential for the optimization of liquid fuel injectors/atomizers in order to maximize energy efficiency, minimize pollutant emissions, and meet the operability requirements of a particular application [1]. Spray cooling, as an effective technique to remove heat from a hot surface, has been used widely to control quenching rates in metallurgical industry [2] and to achieve fast cooling of hot electronics components [3]. As reported in[4], while the size and initial temperature of liquid droplets influence the amount of sensible heating that can be removed in spray cooling, the behavior of the small in-flight liquid droplets would be affected by the rising hot gas or vapor resulting from the evaporation at the hot surface, inhibiting any subcooling effect. Thus, the quantitative information to describe the

dynamic and thermodynamic characteristics of the small in-flight droplets is indispensable for the design optimization to augment the heat transfer from the hot surface in spray cooling applications.

The dynamic and thermodynamic characteristics of in-flight droplets in spray flows are usually quantified in the terms of droplet size, flying velocity, and temperature of the droplets. While the size and flying velocity of liquid droplets may affect the heat and mass transfer processes between the droplets and the surrounding gas flows via convection, droplet temperature is actually one of the most important properties, which is directly related to the heat and mass transfer from or to the liquid droplets through atomization or/and evaporation process. Among various parameters of interest in characterizing the dynamic and thermodynamic behavior of droplets in spray flows, droplet temperature is the one of the least investigated due to the lack of suitable non-intrusive measurement techniques.

Global rainbow thermometry (GRT) technique, which is based on the rainbow position and its dispersion as a function of the refractive index dependent on temperature, has been developed to measure the size and temperature of liquid droplets in spray flows[5,6]. Since liquid droplets are assumed to be perfectly spherical in GRT, non-spherical droplets may cause significant systematic errors in GRT measurements [6,7]. While Wilms et al.[8] proposed an approach to improve GRT technique by filtering out the non-spherical droplets to reduce biased errors, the inevitable presence of refractive index gradients induced by the non-uniform temperature distributions within liquid droplets would still cause significant biased errors in GRT measurements[5,6].

Laser induced fluorescence (LIF) technique has also been used for temperature measurement of liquid droplets in spray flows. LIF-based thermometry techniques are based on the temperature dependence of LIF intensity for some fluorescent tracer molecules premixed within the liquid droplets. In applying LIF-based thermometry techniques to measure temperature of liquid droplets, two detecting bands from the fluorescence spectra (i.e., 2-colors LIF-based thermometry) were usually chosen in order to minimize the effects of the non-uniformities of the illuminating laser intensity and fluorescence dye concentration on the temperature measurements [9–11]. To implement 2-color LIF-based thermometry techniques, two cameras with various optical filters are usually required, along with a very careful image registration or coordinate mapping procedure in order to get the quantitative spatial relation between the two acquired LIF images. In addition, other complications also need to be carefully considered, such as the relatively low temperature sensitivity, the spectral conflicts to cause re-absorption of fluorescent emission, and photo bleaching of the fluorescence dyes in using 2-color LIF-based thermometry approaches for the temperature measurements of in-flight droplets [9,11,12].

While several other measurement techniques, which include Raman scattering[13–15], thermochromics liquid crystal thermometry[16–18] and infrared imaging thermography[19,20], have also been used to measure the temperatures of liquid droplets, almost of them have relatively poor measurement accuracy and require complicated experimental setup to achieve quantitative temperature measurements of small in-flight liquid droplets. More recently, Lemoine & Castanet[21] provide a comprehensive review of various optical

techniques for quantitative measurements of temperature and chemical composition of droplets.

Simultaneous measurements of droplet size, flying velocity, and transient temperature of in-flight droplets are highly desirable to characterize the dynamic and thermodynamic behaviors of liquid droplets in spray flows. While some of the measurement techniques described above can measure the droplet size and temperature of the liquid droplets in spray flows, none of those techniques can provide quantities measurements of the flying velocity of the in-flight droplets simultaneously. Those techniques are required to combine with other velocimetry techniques such as laser Doppler velocimetry (LDV) or particle imaging velocimetry (PIV) in order to achieve simultaneous measurements of droplet size, flying velocity and temperature of the liquid droplets in spray flows, which would complicate the experimental setup and add extra burdens on the instrumentation cost for the measurements.

In the present study, we report the progress made in our recent efforts to develop a novel molecular tagging technique for simultaneous measurements of droplet size, flying velocity and transient temperature of liquid droplets in spray flows. The molecular tagging technique described here is a Laser Induced phosphorescence (LIP) based technique, which can be considered an extension of the molecular tagging velocimetry and thermometry technique developed by Hu & Koochesfahani[22]. For the molecular tagging measurements, a pulsed laser is used to "tag" phosphorescent tracer molecules premixed within liquid droplets (i.e., water droplets for the present study). The long-lived LIP emission is imaged at two successive times after the same laser excitation pulse. The size

of the liquid droplets is determined quantitatively based on the acquired droplet images with a pre-calibrated scale ratio between the image plane and the object plane. A particle-tracking algorithm is used to determine the displacement vectors of the in-flight droplets between the two LIP image acquisitions, thereby, to estimate the flying velocities of the liquid droplets. The transient temperature of the in-flight droplets is derived by taking advantage of the temperature dependence of the phosphorescence lifetime, which is estimated from the phosphorescence intensity ratio of the droplets in the two interrogations.

It should be noted that, while molecular tagging techniques have been developed and successfully applied to achieve flow velocity and temperature measurements in single-phase flows[23,24] and stationary surface droplets[25,26], the work presented here will deal with a multiphase spray flow system involving in-flight liquid droplets with transient temperature change and unsteady heat transfer with ambient gas phase flows. The work described here, to our knowledge, is the first of its nature that is capable of achieving simultaneous measurements of droplet size, flying velocity and transient temperature of in-flight liquid droplets in spray flows. No similar work has ever been published/reported before. It can be implemented with only a single intensified CCD camera, a single-pulsed Ultraviolet (UV) laser and phosphorescent molecules for the simultaneous measurements of multiple important properties in spray flows, which offers significant advantages over other flow diagnostic techniques to characterize spray flows.

In the following sections, the technical basis of a lifetime-based molecular tagging thermometry (MTT) technique for the transient temperature measurements of in-flight droplets is described briefly at first. Then, the related physical properties of the

phosphorescent 1-BrNp·Mβ-CD·ROH triplex for the molecular tagging measurements is introduced. The feasibility and implementation of the molecular tagging technique are demonstrated by conducting simultaneous measurements of droplet size, flying velocity and transient temperature of micro-sized water droplets exhausted from a piezoelectric droplet generator into ambient air at different test conditions in order to characterize the dynamic and thermodynamic behaviors of the micro-sized in-flight droplets. The unsteady heat transfer process between the in-flight droplets and the ambient air is also analyzed theoretically by using the Lumped Capacitance method to predict the dynamic temperature changes of the in-flight water droplets along their flight trajectories. The measured temperature data are compared with the theoretical analysis results quantitatively to validate the measurement results.

2.2 Technical Basis of the Molecular Tagging Technique

2.2.1 Technical basis of molecular tagging technique for droplet temperature measurement

It is well known that both fluorescence and phosphorescence are molecular photoluminescence phenomena. Compared with fluorescence, which typically has a lifetime on the of order nanoseconds, phosphorescence can last as long as microseconds, even minutes. Since emission intensity is a function of the temperature for some substances, both fluorescence and phosphorescence of tracer molecules may be used for temperature measurements. While fluorescence (LIF) techniques have been widely used for temperature measurements of liquid droplets in spray flows [9–11], Laser-induced phosphorescence (LIP) techniques have also been suggested recently to conduct

temperature measurements of ‘‘in-flight” or levitated liquid droplets [27,28]. Compared with LIF-based thermometry techniques, the relatively long lifetime of LIP has been used to prevent interference from scattered/reflected light and any fluorescence from other substances (such as from solid surfaces for the near surface measurements) that are present in the measurement area, by simply putting a small time delay between the laser excitation pulse and the starting time for phosphorescence image acquisitions [25]. Furthermore, LIP was found to be much more sensitive to temperature compared with LIF [27,28], which is favorable for the accurate temperature measurements of small liquid droplets. The molecular tagging technique described here is a LIP based technique.

According to quantum theory [29], with unsaturated laser excitation, the intensity of a photoluminescence process (either fluorescence or phosphorescence) decays exponentially. For simplicity, only a signal-exponential process is considered here. As described in Hu and Koochesfahani[22,24], for a diluted solution and unsaturated laser excitation, the collected phosphorescence signal (S_p) by using a gated imaging detector with integration starting at a delay time t_o after the laser excitation pulse and a gate period of δt can be given by:

$$S_p = AI_i C\varepsilon \Phi_p \left(1 - e^{-\delta t/\tau}\right) e^{-t_o/\tau} \tag{2.1}$$

where A is a parameter representing the detection collection efficiency, I_i is the local incident laser intensity, C is the concentration of the phosphorescent dye (the tagged molecular tracer), ε is the absorption coefficient and Φ_p is the phosphorescence quantum efficiency. The emission lifetime τ refers to the time at which the intensity drops to 37% (i.e., 1/e) of the initial intensity. For an excited state, the deactivation processes may

involve both radiative and nonradioactive pathways and the lifetime of the photoluminescence process, τ, is determined by the sum of all the deactivation rates, i.e. $\tau^{-1} = k_r + k_{nr}$, where k_r and k_{nr} are the radiative and non-radiative rate constants, respectively. According to photoluminescence kinetics, the non-radiative rate constant is, in general, temperature dependent (Ferraudi, 1988), and the resulting temperature dependence of the phosphorescence lifetime is the basis of the present technique for temperature measurement.

It should also be noted that the absorption coefficient ε, and quantum yield Φ_p are usually temperature dependent in general [30], resulting in a temperature-dependent phosphorescence signal (S_p). Thus, in principle, the collected phosphorescence signal (S_p) may be used to measure temperature if the incident laser intensity and the concentration of the phosphorescent dye remain constant (or are known) in the region of interest.

As shown in Equation (2.1), the collected phosphorescence signal (S_p) is also a function of the incident laser intensity (I_i) and the concentration of the phosphorescent dye (C), thus, the spatial and temporal variations of the incident laser intensity and the non-uniformity of the phosphorescent dye (such as due to photo bleaching and/or the changes of the dye concentration in liquid droplets during evaporation process) in the region of interest would have to be corrected separately in order to derive quantitative temperature data from the acquired phosphorescence images. In practice, however, it is very difficult, if not impossible, to ensure a non-varying incident laser intensity distribution and a constant dye concentration within liquid droplets due to evaporation process, which may cause significant errors in the temperature measurements. To overcome this problem, Hu

and Koochesfahani[22,24,31] developed a lifetime-based Molecular Tagging Thermometry (MTT) technique， which can eliminate the effects of incident laser intensity and concentration of phosphorescent dye on temperature measurements effectively.

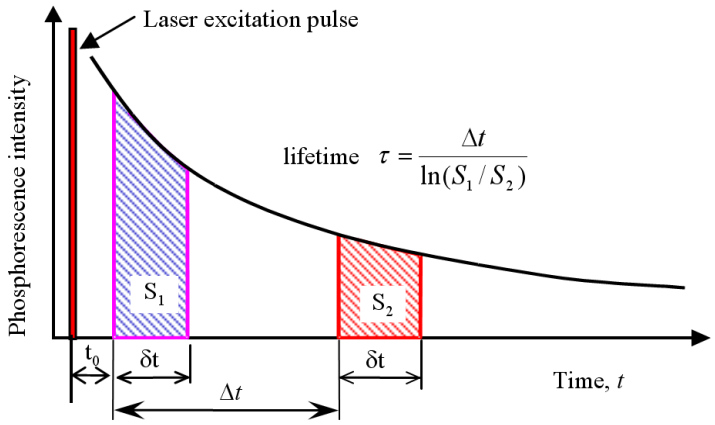

Figure 2.1 Timing chart of lifetime-based MTT technique

The lifetime-based MTT technique works as follows: As illustrated in figure 2.1, a pulsed laser is used to "tag" phosphorescent tracer molecules premixed within working liquids (i.e., water for the present study). LIP emission is interrogated at two successive times after the same laser excitation pulse. The first image is detected at the time $t = t_o$ after laser excitation for a gate period δt to accumulate the phosphorescence intensity S_1, while the second image is detected at the time $t = t_o + \Delta t$ for the same gate period to accumulate the phosphorescence intensity S_2. As described in Hu & Koochesfahani[22,24,31], by taking integration of Equation (2.1) on the temporal window Δt, the accumulated phosphorescence intensities S_1 and S_2 can determined, and the ratio of the two phosphorescence signals (*R*) can be expressed as:

$$R = S_2 / S_1 = \frac{AI_i C\varepsilon\Phi_p \left(1-e^{-\delta t/\tau}\right) e^{-(t_o+\Delta t)/\tau}}{AI_i C\varepsilon\Phi_p \left(1-e^{-\delta t/\tau}\right) e^{-t_o/\tau}} = e^{-\Delta t/\tau} \tag{2.2}$$

It indcates that the intensity ratio of the two successive phosphorescence images (R) is only a funtion of the phosphorescence lifetime τ and the time delay Δt between the two image acqusitions, which is a controllable parameter. Based on Equation (2.2), the phosphorescence lifetime of the molecular tracers can be calculated according to

$$\tau = \frac{\Delta t}{\ln(S_1 / S_2)} \tag{2.3}$$

As described in Hu and Koochesfahani (2006, 2011) and Hu et al (2010), since the photoluminescence lifetime is temperature dependent for some molecular tracers, with the conditions of diluted solution and unsatuated laser exciation, the temperature distribution in a fluid flow can be derived from the distribution of the intensity ratio of the two photoluminescence images acquired after the same laser excitation pulse. For a given molecular tracer and fixed Δt value, Equation (2.2) defines a unique relation between phosphorescence intensity ratio (R) and fluid temperature T, which can be used for thermometry as long as the temperature dependence of phosphorescence lifetime of the molecular tracers is known. This ratiometric approach eliminates the effects of any temporal and spatial variations in the incident laser intensity (due to pulse-to-pulse laser energy variations) and non-uniformity of the dye concentration (e.g., due to photobleaching or concentration change of the tracer molecules within liquid droplets due to evaporation at a high temperature environment).

To implement the lifetime-based MTT technique described above, only one laser pulse is required to excite or 'tag' the tracer molecules for each instantaneous temperature measurement. The two successive acquisitions of the photoluminescence image of the tagged tracer molecules can be achieved using a dual-frame intensified CCD camera. Compared to the two-color LIF thermometry techniques described above [9–11], which usually require two CCD cameras with proper optical filters to acquire two fluorescent images simultaneously for each instantaneous temperature measurement, the present lifetime-based MTT technique is much easier to implement and can significantly reduce the burden on the instrumentation and experimental setup. Furthermore, since LIF emission is short lived with the emission lifetime on the order of nanoseconds, LIF images are usually acquired when the incident laser illumination is still on; therefore, they are vulnerable to the contaminations of scattered/reflected light and any fluorescence emission from other substances. For the lifetime-based MTT technique describe here, as schematically indicated in figure 2.1, the small time delay between the illumination laser pulse and the phosphorescence image acquisition can effectively eliminate all the effects of scattered/reflected light and any fluorescence from other substances that are present in the measurement region. Since only the phosphorescence emission of the tagged phosphorescent molecules was acquired for the MTT measurements, the acquired phosphorescence images of the water droplet are quite "clean", in comparison with LIF images.

2.2.2 Simultaneous measurements of droplet size and flying velocity of in-flight droplets

In addition to measuring the transient temperature of liquid droplets, droplet size and flying velocity of the in-flight droplets can also be determined simultaneously based on the acquired phosphorescence image pair. With a pre-calibrated scale ratio between the image plane and the object plane for the phosphorescence image acquisition, the size of the in-flight droplets can be determined quantitatively by measuring the dimension of the droplets in the acquired phosphorescence images via an image processing procedure. Furthermore, a particle-tracking algorithm can be used to determine the displacement vectors of the in-flight droplets between the two phosphorescence image acquisitions. Since the time delay Δt between the two image acquisition is known for a specific experiment, the flying velocities of the in-flight droplets can also be estimated based on the measured displacement vectors of the in-flight droplets between the two phosphorescence image acquisitions.

Further technical details about the simultaneous quantification of droplet size and flying velocity, in addition to the transient temperature measurements, of the in-flight droplets, will be described in the "Results and Discussions" section of the present study.

2.2.3 Phosphorescence molecular tracer used in the present study

It is well known that laser-induced phosphorescence techniques usually surfer from oxygen quenching to phosphorescence emission. In the present study, a specially designed phosphorescent triplex (1-BrNp·Mβ-CD·ROH) was used as the molecular tracer for the molecular tagging measurements. The phosphorescent 1-BrNp·Mβ-CD·ROH triplex is actually the mixture compound of three different chemicals, which are lumophore

(indicated collectively by 1-BrNp), maltose-β-cyclodextrin (indicated collectively by Mβ-CD) and alcohols (indicated collectively by ROH). According to Hartmann et al (1996) and Gendrich et al (1997), the special molecular structures of the phosphorescent triplex (1-BrNp·Mβ-CD·ROH) would form a molecular shell to prevent laser-induced phosphorescence emission of the excited 1-BrNp molecules from oxygen quenching effects.

Figure 2.2(a) shows the normalized absorption and emission spectra of the phosphorescent 1-BrNp·Mβ-CD·ROH triplex. The fluorescence and phosphorescence spectra are both shown in the plot, and the phosphorescence emission is significantly red-shifted relative to fluorescence. It should be noted that, because of the large red shift as shown in the figure, there is no overlap between the phosphorescence emission and absorption spectra, which suggests that the phosphorescence does not get re-absorbed with the phosphorescent triplex (1-BrNp·Mβ-CD·ROH) as the molecular tracer for flow measurements. Figure 2.2(b) shows the emission spectra of the 1-BrNp·Mβ-CD·ROH solution at different temperatures. As shown clearly in the figure, while the phosphorescence emission of the triplex is very temperature sensitive, its fluorescence is almost independent of temperature. The fluorescence lifetime of 1-BrNp·Mβ-CD·ROH triplex is within 20 ns, while its phosphorescence lifetime is found to be much longer, on the order of several milliseconds, as reported in Hu et al (2006) and Hu & Koochesfahani (2006, 2011). Further information about the chemical and photoluminescence properties of the phosphorescent triplex (1-BrNp·Mβ-CD·ROH) is available at Hartmann et al (1996) and Gendrich et al (1997).

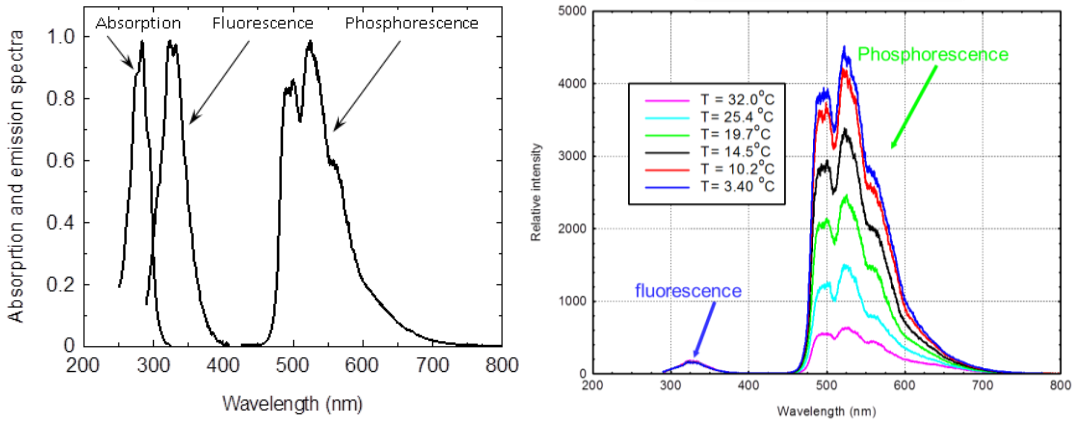

Figure 2.2 Absorption and emission spectra of 1-BrNp·Gβ-CD·ROH triplex [34].
(a) Normalized absorption & emission spectra. (b) Emission spectra at different temperatures.

Upon the pulsed excitation of a UV laser (i.e., quadrupled wavelength of Nd:YAG laser at 266nm for the present study), the phosphorescence lifetime of the phosphorescent triplex (1-BrNp·Mβ-CD·ROH) molecules in an aqueous solution was found to change significantly with temperature. Figure 2.3 shows the measured phosphorescence lifetimes of the 1-BrNp·Mβ-CD·ROH molecules as a function of temperature, which were obtained through a calibration experiment similar as those described in Hu & Koochesfahani (2006). It can be seen clearly that phosphorescence lifetime of 1-BrNp·Mβ-CD·ROH molecules varies greatly with increasing temperature, decreasing from about 2.7 ms to 1.9 ms as the temperature changes from 10.0ºC to 20.0ºC. The relative temperature sensitivity of the phosphorescence lifetime is about 3.3% per degree Celsius, which is much higher than those of fluorescent dyes used for LIF-based thermometry measurements. For comparison, the temperature sensitivity of Rhodamine B widely used for LIF-based thermometry is less than 2.0% per degree Celsius[12,34].

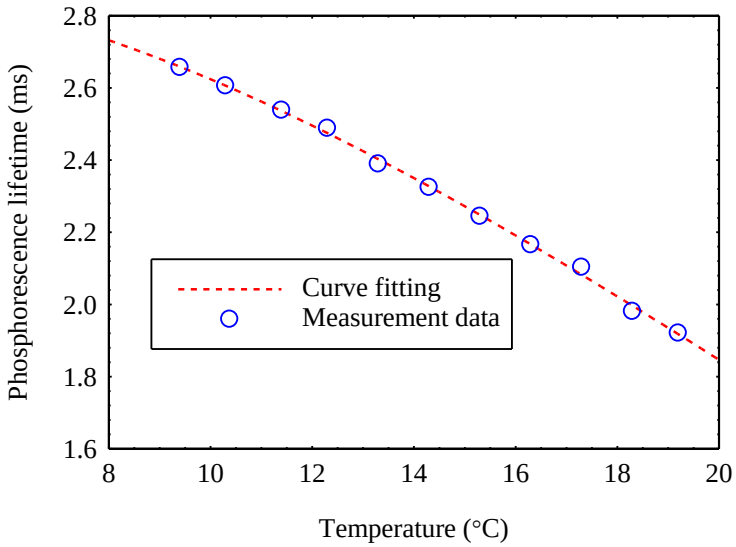

Figure 2.3 Variation of droplet temperature versus phosphorescence lifetime (Neopentyl alcohol was used to make 1-BrNp·Mβ-CD·ROH triplex)

In the present study, we used a concentration of 2×10^{-4} M for Mβ-CD, a saturated (approximately 1×10^{-5} M) solution of 1-BrNp, and a concentration of 0.03M for Neopentyl alcohol (ROH) in making 1-BrNp·Mβ-CD·ROH triplex. It should be noted that, while Cyclohexanol alcohol was widely used to make 1-BrNp·Mβ-CD·ROH triplex for molecular tagging measurements in the previous studies [24,31,34,35], Neopentyl alcohol used in the present study was found to increase the phosphorescence intensity of the 1-BrNp·Mβ-CD·ROH triplex significantly. However, the phosphorescence lifetime of 1-BrNp·Mβ-CD·ROH triplex was found to become much shorter when the Neopentyl alcohol was used in making 1-BrNp·Mβ-CD·ROH triplex. For example, at the room temperature of T=20°C, the phosphorescence lifetime of 1-BrNp·Mβ-CD·ROH triplex with Cyclohexanol alcohol would be about 3.7ms as reported in Hu et al. (2010). However,

it becomes only about 1.9 ms when Neopentyl alcohol was used to make 1-BrNp·Mβ-CD·ROH triplex, as shown in figure 2.3.

2.2.4 Experimental setup for demonstration experiments

Figure 2.4 shows the schematic of the experimental setup used in the present study to demonstrate the feasibility and implementation of the molecular tagging technique described above to achieve simultaneous measurements of droplet size, flying velocity and transient temperature of in-flight droplets. Water is used as the working fluid in the present study, and phosphorescent triplex (1-BrNp·Mβ-CD·ROH) was premixed with water in a reservoir tank. As shown schematically in figure 2.4, a high-pressure gas cylinder was used to press the water inside the reservoir tank flow into a pipeline connected to a piezoelectric droplet generator. By applying square-wave-shaped signals to drive the piezoelectric actuator inside the droplet generator, water droplets would be generated and exhausted from the droplet generator into ambient air in a mono-sized water droplet stream. By changing the nozzle diameter of the piezoelectric droplet generator, the diameter of the water droplets exhausted from the droplet generator was adjustable in the range of 200 μm to 1000 μm (i.e., ~450 μm in diameter for the test cases of the present study). The velocity of the micro-sized water droplets exhausted from the droplet generator ranged from 0.1 m/s to 10 m/s by varying the gas pressure applied to the water reservoir tank. During the experiments, while the temperature of the ambient air was maintained at a constant room temperature of T_∞ = 22 ˚C, the temperature of the water (i.e., along with 1-BrNp·Mβ-CD·ROH triplex) inside the reservoir tank, monitored by using a thermocouple, was kept constant at a pre-selected low temperature level (i.e.,

ranged from 3˚C to 15˚C) by using a Constant Temperature Bath Circulator. As a result, the temperature of the water droplets out of the droplet generator was lower than the ambient air temperature, and the micro-sized droplets in the water droplet stream would be convectively heated up while flying in the ambient air. Thus, the temperature of the in-flight water droplets would increase monotonically along their flying trajectories.

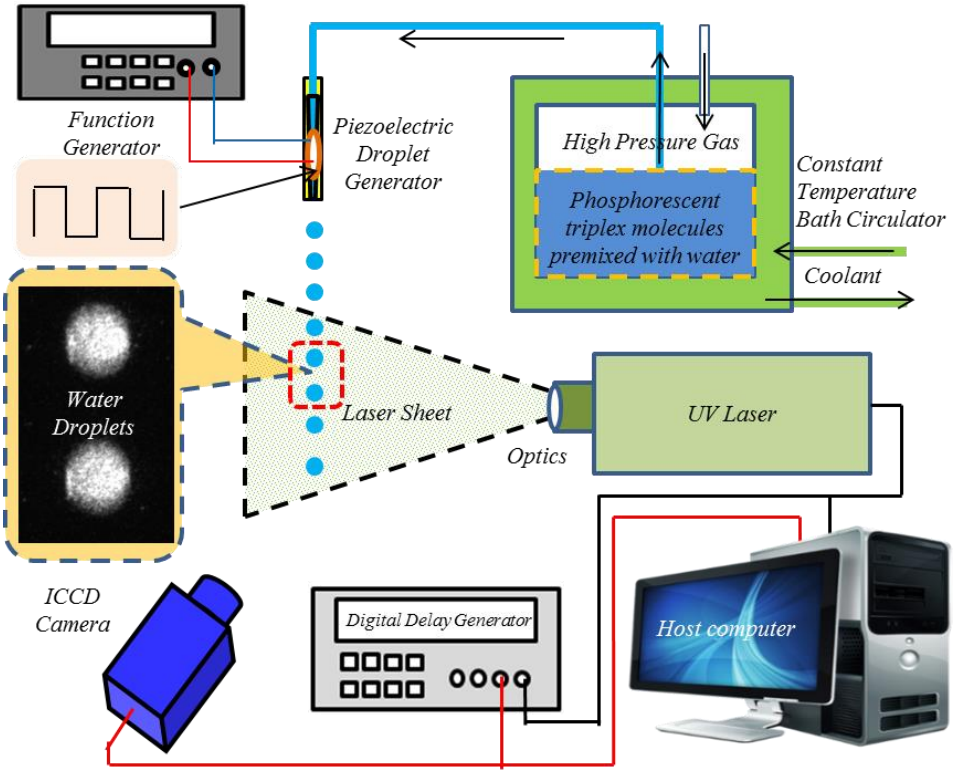

Figure 2.4 Experiment Setup Used for the Demonstration Experiments

In the present study, a pulsed Nd:YAG laser at a quadrupled wavelength of 266 nm (5ns pulse duration) was used to excite or 'tag' the molecules of 1-BrNp·Mβ-CD·ROH triplex within the water droplets. A set of optical lenses and mirrors were used to shape the laser beam into a laser sheet of ~ 500 μm in thickness to illuminate the mono-sized droplet stream along the central plane of the droplet generator exit. A dual-fame intensified

CCD camera (PCO DICAM-Pro, Cooke Corporation, 1280 pixels ×1024 pixels in resolution) with a fast-decay phosphor (P46) was used to acquire the phosphorescence images at two successive times after the same laser excitation pulse, as shown schematically in figure 2.1. For the molecular tagging measurement results given in the present study, the first phosphorescence image of the in-flight droplets was acquired at 230μs after the laser excitation pulse with an exposure time of 100μs. The second phosphorescence image was acquired at 1.1*ms* later after the same laser pulse with the same exposure time (i.e., $\Delta t=1.1ms$ between the image pair). The laser and the camera were synchronized using a digital delay generator (SRS-DDG535), which controlled the timing of the laser sheet illumination and the intensified camera data acquisition.

It is also noted that since a low concentration of the phosphorescent 1-BrNp·Mβ-CD·ROH triplex was used for the present study, the effects of the molecular tracers on the physical properties of water are believed to be small and are assumed to be negligible. During the experiments, the energy level of the pulse laser used to tag the molecular tracers within water droplets was below 0.5 mJ/pulse. The repetition rate of the pulsed laser excitation was set to be 1 Hz. The energy deposited by the excitation laser into the water droplets was very small, and the temperature rise of the water droplets due to the energy deposition of the laser excitation was estimated to be very small and is also assumed to be negligible.

2.3 Measurement Results and Discussions

2.3.1 Determination of droplet size from the acquired phosphorescence images

As shown schematically in figure 2.1, to implement the molecular tagging technique described above, a pulsed laser was used to "tag" 1-BrNp·Mβ-CD·ROH triplex molecules premixed within the water droplets, and the "tagged" phosphorescent molecules were imaged at two successive times within the phosphorescence lifetime of the tagged tracer molecules. Figure 2.5 shows a typical acquired phosphorescence image pair (i.e., the first phosphorescence image was acquired at 0.23 ms after the laser excitation pulse and the second phosphorescence image at 1.33 ms after the same laser pulse with the same exposure time of 0.1 ms) for the molecular tagging measurements. It can been seen that, since the time delay (i.e., 0.23ms for the present study) between the laser excitation pulse and the phosphorescence image acquisition can eliminate the scattered/reflected light from the droplet surfaces and any fluorescence from other substances (e.g., the transparent side walls of the test rig) near the measurement region effectively, the phosphorescence images of the water droplets are quite ''clean" even though no optical filter was used in the present study for the phosphorescence image acquisition.

To implement the molecular tagging technique described above, the image size of the droplets should be consistent with the physical scale to be solved. Similar as LIF-based technique, the dynamic range of the droplet size (i.e., the range from the smallest droplet to the largest droplet) to be measured accurately is limited by the resolution of the digital camera used for the phosphorescence image acquisition. While the upper limit of the droplet size (i.e., the largest droplet to be measured accurately using molecular tagging

technique) is set by the total pixel number of the digital camera, the lower limit of the droplet size (i.e., the smallest droplet to be measured accurately) is set by a single pixel of the digital camera (i.e., the largest water droplets with its image size being only 1 pixel in the acquired phosphorescence image.

Based on the acquired phosphorescence images as those shown in figure 2.5, the sizes of the water droplets can be measured quantitatively. Since the phosphorescence, images of the in-flight droplets are ‘‘clean”, the outer boundaries of the water droplets can be identified easily in the acquired phosphorescence images by using Matlab-based image processing software developed “in house”. As shown schematically in figure 2.5(a), a typical threshold intensity value of 250 for the acquired 12-bit phosphorescence images was selected in order to determine the outer boundary of a randomly selected water droplet in the droplet stream, and the diameter of the water droplet was found to be 60 pixels, i.e., $D_0 = 60$ pixels, in the acquired phosphorescence images. In the present study, a parametric study was conducted by using different threshold intensity values (i.e., the threshold intensity value was changed from 150 to 350) in identifying the outer boundaries of water droplets in the acquired 12-bit phosphorescence images. The standard deviation of the measured droplet size in the mono-sized droplet stream was found to be about 2.3 pixels, which is about 4% of the droplet size.

With the pre-calibrated scale ratio between the image plane and the object plane as given in figure 2.5(b), the size of the randomly selected droplet can be determined quantitatively, which was measured to be about 450μm.

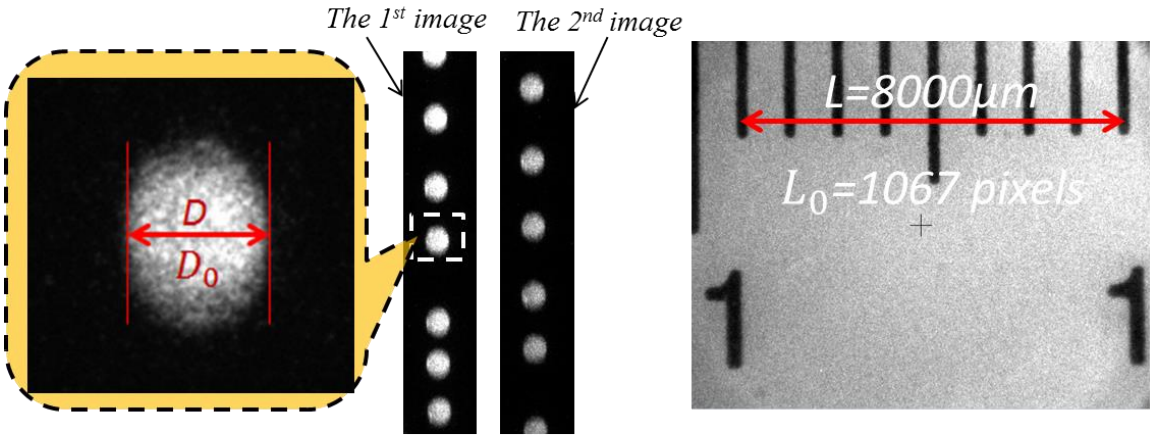

(a). Acquired phosphorescence image pair of the in-flight droplets

(b). Scale ratio between the image plane and the object plane

Figure 2.5 Determination of in-flight droplet size from the acquired phosphorescence images

2.3.2 Determination of flying velocity of the in-flight water droplets

By twisting the square-wave shaped signals supplied to the piezoelectric actuator inside the droplet generator, the distance between the neighboring droplets in the droplet stream exhausted from the droplet generator can be manipulated. The information was used to identify the displacements of any pre-selected droplets in the mono-sized water droplet stream between the acquired phosphorescence image pair, thereby, the flying velocity of the droplets can be determined quantitatively from the acquired phosphorescence image pair. As described above, once the outer boundaries of the droplets were determined for droplet size measurements, the center locations of the in-flight droplets in the acquired phosphorescence images as shown in figure 2.6 can be easily identified by using the Matlab-based image processing software developed “in-house”. The correspondence of the water droplets in the acquired phosphorescence image pair can be determined based on the information encoded in the distances among the neighboring

droplets, which is similar to the cross-correlation based particle tracking algorithm used by Saga et al (2001) for particle tracking velocimetry (PTV) applications.

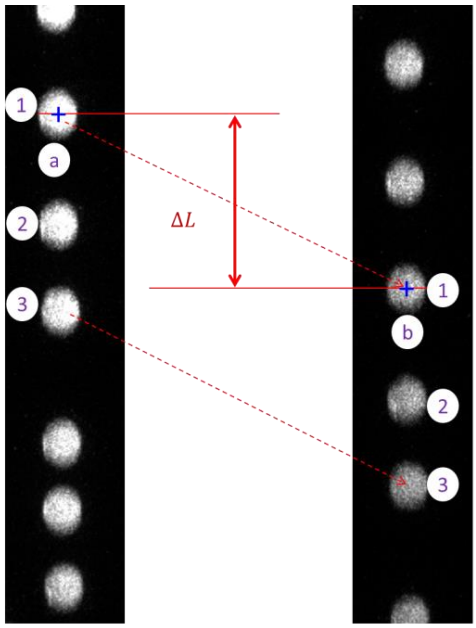

(a). The first image taken at 0.23ms after the laser pulse

(b). The second image taken at 1.33ms later after the same laser pulse

Figure 2.6 Determination of the flying velocity of the droplets from the phosphorescence images.

As shown schematically in figure 2.6, for a pre-selected droplet "*#1*" located at the position of "*a*" in the first image, the corresponding position of the same droplet, i.e., the new position "*b*", in the second image can be determined easily based on its unique identification information encoded in the distances from the droplet to the neighboring droplets. Then, the displacement vector, $\overrightarrow{\Delta L}$, of the pre-selected droplet from its original position "*a*" in the first image to its new position *"b"* in the second image can be determined quantitatively. In order to improve measurement accuracy in determining the flying velocities of the water droplets, a "sub-pixel interpolation" process, which is similar as that described in Hu et al. (1998) for PIV image processing, was used in the present

study to locate the centers of the flying droplets at a sub-pixel level. Based on the statics of the measured flying velocity of the water droplets in the droplet stream, the standard deviation of the measured flying velocity of the mono-sized water droplets was found to be about 3.2 pixels, which is about 1.1% of the displacement of the water droplets between the acquired phosphorescence image pair (i.e., averaged displacement of the water droplets given in figure 2.6 is 295.5 pixels. With the time delay between the acquired phosphorescence image pair known as Δt =1.1ms and the pre-calibrated scale ratio between the image plane and the object plane as that in figure 2.5(b), the flying velocity of the water droplet "*#1*" can be calculated as $V = \overrightarrow{\Delta L}/\Delta t$ For example, for the test case shown in figure 2.6, the flying velocity of the pre-selected droplet "*#1*" was measured as *V*= 2.03 m/s.

2.3.3 Determination of the transient temperature of the in-flight droplets

After the corresponding positions of the in-flight droplets in the acquired phosphorescence image pair are determined, the intensity ratio of the same droplets in the two phosphorescence images can be used to calculate the phosphorescence lifetime of the 1-BrNp·Mβ-CD·ROH triplex molecules within the water droplets by using Equation (2.3). With the calibration profile of the phosphorescence lifetime vs. temperature as that shown in figure 2.3, the instantaneous temperature of the in-flight water droplet can be derived quantitatively from the acquired phosphorescence image pair. For the image processing of the lifetime-based MTT technique to calculate intensity ratio of the acquired phosphorescence pair (i.e., S1/ S2), selecting the interrogation windows in the 1st and 2nd phosphorescence images will be consistent with the scales of the water droplets to be

measured. As shown theoretically in Equation (2.3), since the intensity ratio of the acquired phosphorescence pair, thereby, the lifetime of the phosphorescence emission, is only the function of the temperature of the tagged phosphorescent tracer molecules, the dynamic size change of the in-flight droplets due to evaporation would have no effect on the intensity ratio of the acquired phosphorescence pair. Figure 2.7 gives the phosphorescence intensity distributions of typical acquired phosphorescence images of the droplet stream (the black marks/circles on the images indicate the centers of the flying water droplets) along with the instantaneous temperature of the in-flight droplets derived from the phosphorescence image pair. As shown in figure 2.7, the instantaneous temperatures of the in-flight droplets in the center of the measurement window was found to be 11.9°C, 12.6°C and 11.6°C, respectively.

Based on the time sequence of the measured instantaneous temperature distributions of the water droplets as those shown in figure 2.7, the dynamic and thermodynamics characteristics of the in-flight water droplets along their flying trajectories can be revealed quantitatively, which will be discussed in detail in the following sections.

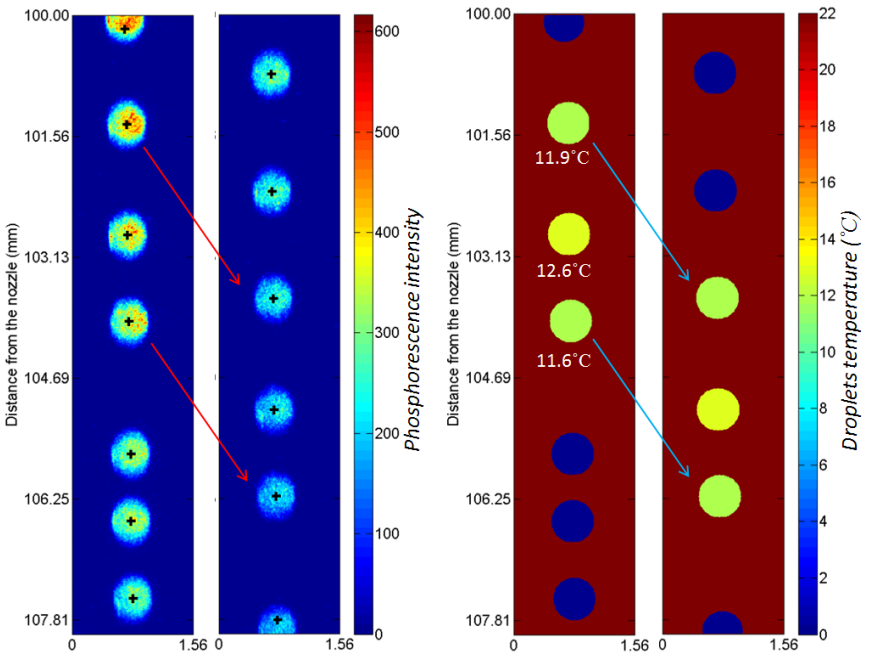

Figure 2.7 Simultaneous measurements of droplet size, flying velocity and transient temperature of the in-flight droplets by using molecular tagging technique

2.3.4 Theoretical analysis on the unsteady heat transfer process between the in-flight droplets and ambient air

As described above, since the initial temperature of the water droplets out of the droplet generator was set to be lower than the temperature of ambient air, the small water droplets will be convectively heated up while they fly through the ambient air. A theoretical analysis was performed in the present study by using the Lumped Capacitance Method to examine the unsteady heat transfer process between the in-flight water droplets and the ambient air to predict the temperature variations of the in-flight droplets along their flying trajectories.

The following assumptions are made in the theoretical analysis to examine the unsteady heat transfer process between the in-flight water droplets and the ambient air:

1. The water droplets are assumed to keep their spherical shape while flying in the ambient air.

2. Negligible radiation effects due to the relatively low temperature of the water droplets.

3. Negligible small thermal resistance at the droplet surface, and negligible small temperature change of ambient air around the in-flight water droplet.

4. Since only the spatially-averaged temperature of the water droplets is considered in the present study and the Biot number of the tiny water droplets (i.e., ~450μm in diameter) considered here is very small (i.e., $Bi = h.D/K << 0.1$), the in-flight water droplets are considered as isothermal spheres with the temperature differences within the micro-sized water droplets being neglected.

By using the Lumped Capacitance Method described in the heat transfer textbook of Incropera and Dewitt (2002), the balance of the heat transfer in and out of a control volume around an in-flight water droplet can be expressed as:

$$-hA_s(T - T_\infty) = \rho\, Vol\, C_p \frac{dT}{dt} \tag{2.4}$$

Where h is the convection coefficient of air around the surface of the in-flight water droplet; A_s is the surface area of the spherical droplet; T is the transient temperature of the in-flight droplet to be determined; T_∞ is the temperature of ambient air, which is a constant for the present study; ρ is the density of the water droplet, C_p is the specific heat of the droplet; Vol is the volume of the droplet; and t is the time after the water droplet leaves the droplet generator.

Introducing the temperature difference: $\theta = T - T_\infty$, and recognizing that $\frac{dT}{dt} = \frac{d\theta}{dt}$, Equation (2.4) can be re-written as:

$$\frac{\rho Vol\ C_p}{hA_s}\frac{d\theta}{dt} = -\theta \tag{2.5}$$

Separating the variables and integrating from the intial condition, for which at $t = 0$ and $T = T_i$, it can be derived that

$$\frac{\rho Vol\ C_p}{hA_s}\int_{\theta_i}^{\theta}\frac{d\theta}{\theta} = -\int_o^t dt \tag{2.6}$$

Where $\theta_i = T_i - T_\infty$.

Evaluating the integral, it can be expresed as

$$\frac{\rho Vol\ C_p}{hA_s}\ln(\frac{\theta_i}{\theta}) = t \tag{2.7}$$

or

$$\frac{\theta}{\theta_i} = \frac{T - T_\infty}{T_i - T_\infty} = \exp[-(\frac{hA_s}{\rho Vol\ C_p})t] \tag{2.8}$$

Since $Vol = \frac{1}{6}\pi D^3$ and $A_s = \pi D^2$ for the present study, it can be derived that

$$T = [T_i - T_\infty + T_\infty \exp(\frac{6ht}{\rho DC_p})]/\exp(\frac{6ht}{\rho DC_p}) \tag{2.9}$$

where *D* is the diameter of the water droplet.

The convection coefficient *h* is defined by

$$h = Nu_D\frac{k}{D} \tag{2.10}$$

Where, Nu_D is the Nusselt number, and k is the thermal conductivity of air.

As described in Whitaker (1972), the Nusselt number Nu_D around a sphere in air can be expressed as

$$Nu_D = 2 + (0.4\,\mathrm{Re}_D^{1/2} + 0.06\,\mathrm{Re}_D^{2/3})\,\mathrm{Pr}^{0.4}(\frac{\mu}{\mu_s})^{1/4} \tag{2.11}$$

Where Re_D is the Reynolds number of the flying droplet in air, Pr is the Prandtl number, μ is the dynamic viscosity of air at T_i, and u_s is the mean dynamic viscosity of air during the droplet heating process.

The Reynold number Re_D is defined as

$$\mathrm{Re}_D = \frac{VD}{\upsilon} \tag{2.12}$$

Where, V is the flying velocity of the water droplet, and υ is the kinematic viscosity of air.

Based on the Equations (2.9) to (2.12) given above, the transient temperature of the in-flight water droplets along their flying trajectories can be predicted theoretically with the known droplet diameter *D*, flying velocity *V*, droplet initial temperature T_i and ambient air temperature T_∞ .

2.3.5 Comparison of measurement results with the theoretical predictions

In the present study, a set of experiments were conducted to examine the unsteady heat transfer process between the in-flight water droplets and the ambient air at different test conditions. The molecular tagging technique described above was used to achieve simultaneous measurements of droplet size, velocity and temperature of the in-flight droplets. The measured temperature data was compared with the theoretical analysis

results quantitatively to validate the measurement results. The measured temperature data was compared with the theoretical analysis results quantitatively to characterize the dynamic and thermodynamic behaviors of the in-flight droplets.

Since the experiment is designed mainly to demonstrate the implemented procedure of the molecular tagging technique, a relatively small temperature range (i.e., between 10°C and 20°C) was chosen for the experiment in order to simplify the experimental setup. During the experiments, while the ambient air temperature was kept constant at T_∞ = 22°C, the initial temperature of the water droplet exhausted from the droplet generator exit was adjusted from T_i =11°C to 18°C. The micro-sized water droplets were convectively heated up after they were exhausted from the droplet generator into the ambient air. The measurement window was set to locate at about 100mm away from the exit of the droplet generator. As shown in figure 2.5 to figure 2.7, the diameter of the water droplets exhausted from the droplet generator was measured to be about 450 μm with the flying velocity at about 2.03 m/s. It should be noted that the methodology of the molecular tagging technique is rather general, and applicable for a much wider temperature range, depending on the molecular tracers and solutions used for the molecular tagging measurements (e.g., 0 ~ 100^{o}C for the phosphorescent triplex (1-BrNp·Mβ-CD·ROH) premixed in the water droplets). I think we need to do something to improve our ability to increase the working of the anti-water surface.

Based on 50 frames of the instantaneous measurements as those shown in figure 2.7, the average temperature of the micro-sized in-flight water droplet at the center of the measurement window was calculated. Figure 2.8 shows the measured temperature of the

in-flight water droplets at 100mm away from the droplet generator as a function of the initial temperature of the water droplets. The error bars given in the plot represent the standard deviation values based on the 50 frames of instantaneous temperature measurements at each test conditions. The predicted temperature values of the in-flight droplets at different test conditions were also given in the same plot for quantitative comparison. The predicted temperature values were obtained based on the theoretical analysis procedure described above (i.e., in section 3.3) with the measured droplet size (i.e., 450μm in diameter), droplet flying velocity (i.e., V=2.03m/s in flying velocity) and the initial temperature of the water droplets measured at the exit of the droplet generator (i.e., T_i =11°C to 18°C) as the input parameters. As shown in figure 2.8, the measured temperatures of the in-flight droplets were found to agree well in general with the theoretically predicted values. The differences between the measured droplet temperatures and the predicted values were found to be within 0.5˚C, which is comparable to the standard derivation values (i.e., indicated as the error bars in the plot) of the instantaneous temperature measurements.

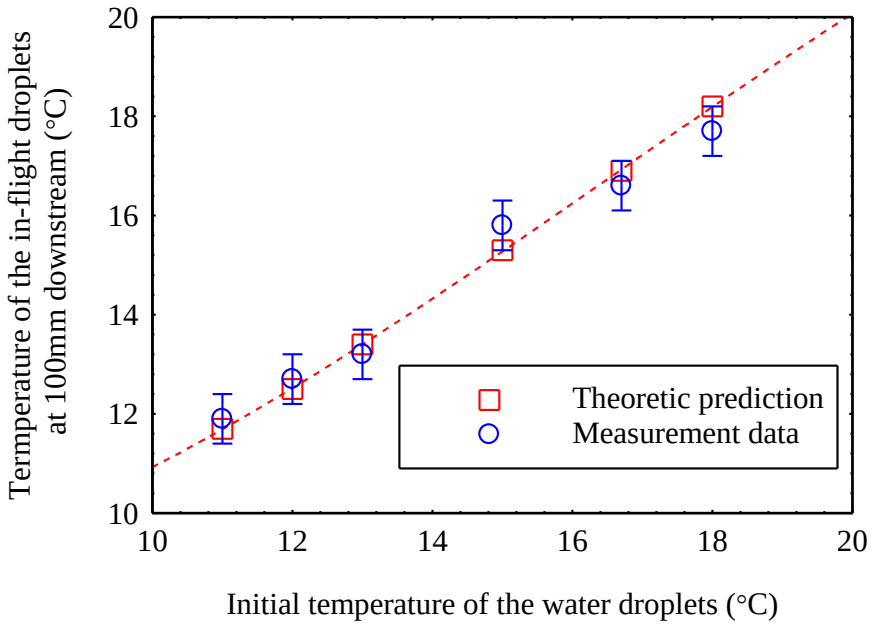

Figure 2.8 The temperature of the in-flight droplets at 100mm away from the droplet generator as a function of the initial temperature of the water droplets

In the present study, the temperature variations of the in-flight water droplets as a function of the flying distance in ambient air were also investigated by moving the measurement window further away from the exit of the droplet generator. During the experiments, the ambient air temperature was kept constant at T_∞ =22 °C, and the initial temperature of the water droplet exhausted from the droplet generator exit was set at T_i =11°C. Figure 2.9 shows the measured temperatures of in-flight water droplets at different time after exhausted from the exit of the droplet generator in comparison with the theoretical predictions. As expected, the temperature of the in-flight water droplets was found to increase monotonically with the increasing flying time in the ambient air due to the convective heat transfer between the in-flight water droplets and the ambient air. While the measured temperature data and the predicted results show a similar tendency as the flying time increases, the rate of increase of the measured temperature data was found

to be slightly higher than that of the theoretical predictions. As a result, the differences between the measured temperature data and the predicted results were found to increase gradually as the flying time increases. The maximum difference between the measured temperature data and the predicted results was found to be about 1.0˚C with the micro-sized water droplets flying about 0.2s after exhausted from the exit of the droplet generator. It should be noted that, in addition to the measurement uncertainty, the simplified theoretic model that neglects the thermal gradients within the water droplets can also contribute the differences between the theoretic predictions and the measurement results.

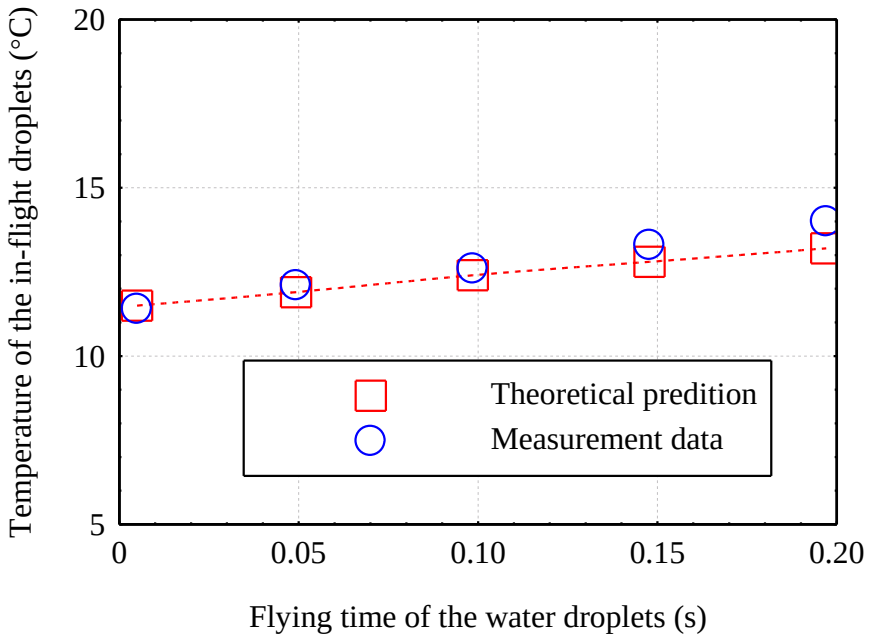

Figure 2.9 The temperature of the in-flight droplets as a function of flying time

2.4 Conclusions

We presented the progress made in developing a molecular tagging technique for achieving simultaneous measurements of droplet size, flying velocity and transient temperature of in-flight liquid droplets. Phosphorescent 1-BrNp·Mβ-CD·ROH triplex

molecules, which can be turned into long-lasting glowing marks upon excitation by photons of appropriate wavelength, were used as the molecular tracers for the quantitative measurements. A pulsed UV laser was used to 'tag' the phosphorescent triplex molecules premixed within in-flight droplets to emit long-lived laser-induced phosphorescence (LIP). After the same laser excitation pulse, the tagged phosphorescent triplex molecules were imaged at two successive times within the phosphorescent lifetime of the tracer molecules. While the size of the in-flight droplets was determined quantitatively based on the acquired droplet images with a pre-calibrated scale ratio between the image plane and the object plane, the displacements of the droplets between the two image acquisitions were used to estimate the flying velocity of the in-flight droplets. The transient temperature of the in-flight droplets was derived simultaneously by taking advantage of the temperature dependence of the phosphorescence lifetime, which is estimated from the phosphorescence intensity ratio of the two interrogations.

The feasibility and implementation of the molecular tagging technique was demonstrated by conducting simultaneous measurements of droplet size, flying velocity and transient temperature of micro-sized water droplets exhausted from a piezoelectric droplet generator at different test conditions. During the experiments, while the ambient air temperature was kept constant at 22°C, the initial temperature of the micro-sized water droplet at the droplet generator exit was set at a lower temperature range from 11°C to 18°C. After injected into the ambient air, the micro-sized water droplets were convectively heated up as they flew through the ambient air, which caused the transient temperature of the micro-sized water droplets to vary dynamically along their flight trajectories. The

unsteady heat transfer process between the in-flight water droplets and the ambient air were also analyzed theoretically by using the Lumped Capacitance method to predict the temperature of the in-flight water droplets along their flight trajectories. The measured temperature data was compared quantitatively with the theoretical analysis results, and the discrepancies between the measured temperature data and the theoretical prediction results were found to be within 0.80˚C.

References

[1] Schulz, C., and Sick, V., "Tracer-LIF diagnostics: quantitative measurement of fuel concentration, temperature and fuel/air ratio in practical combustion systems," *Progress in Energy and Combustion Science*, vol. 31, Jan. 2005, pp. 75–121.

[2] Hall, D. D., and Mudawar, I., "Experimental and numerical study of quenching complex-shaped metallic alloys with multiple, overlapping sprays," *International Journal of Heat and Mass Transfer*, vol. 38, May 1995, pp. 1201–1216.

[3] Salazar, V. M., González, J. E., and Rivera, L. A., "Measurement of Temperatures on In-Flight Water Droplets by Laser Induced Fluorescence Thermometry," *Journal of Heat Transfer*, vol. 126, Apr. 2004, p. 279.

[4] González, J. E., and Black, W. Z., "Study of Droplet Sprays Prior to Impact on a Heated Horizontal Surface," *Journal of Heat Transfer*, vol. 119, May 1997, p. 279.

[5] van Beeck, J. P., and Riethmuller, M. L., "Nonintrusive measurements of temperature and size of single falling raindrops.," *Applied optics*, vol. 34, 1995, pp. 1633–1639.

[6] van Beeck, J. P., Giannoulis, D., Zimmer, L., and Riethmuller, M. L., "Global rainbow thermometry for droplet-temperature measurement.," *Optics letters*, vol. 24, 1999, pp. 1696–1698.

[7] Vetrano, M. R., Gauthier, S., van Beeck, J., Boulet, P., and Buchlin, J.-M., "Characterization of a non-isothermal water spray by global rainbow thermometry," *Experiments in Fluids*, vol. 40, Sep. 2005, pp. 15–22.

[8] Wilms, J., Gréhan, G., and Lavergne, G., "Global Rainbow Refractometry with a Selective Imaging Method," *Particle & Particle Systems Characterization*, vol. 25, Apr. 2008, pp. 39–48.

[9] Zhang, Y., Zhang, G., Xu, M., and Wang, J., "Droplet temperature measurement based on 2-color laser-induced exciplex fluorescence," *Experiments in Fluids*, vol. 54, Jul. 2013, p. 1583.

[10] Castanet, G., Lavieille, P., Lemoine, F., Lebouché, M., Atthasit, A., Biscos, Y., and Lavergne, G., "Energetic budget on an evaporating monodisperse droplet stream using combined optical methods," *International Journal of Heat and Mass Transfer*, vol. 45, Dec. 2002, pp. 5053–5067.

[11] Lavieille, P., Lemoine, F., Lavergne, G., and Lebouché, M., "Evaporating and combusting droplet temperature measurements using two-color laser-induced fluorescence," *Experiments in Fluids*, vol. 31, Jul. 2001, pp. 45–55.

[12] Coppeta, J., and Rogers, C., "Dual emission laser induced fluorescence for direct planar scalar behavior measurements," *Experiments in Fluids*, vol. 25, Jun. 1998, pp. 1–15.

[13] Schweiger, G., "Raman scattering on single aerosol particles and on flowing aerosols: a review," *Journal of Aerosol Science*, vol. 21, 1990, pp. 483–509.

[14] Müller, T., Grünefeld, G., and Beushausen, V., "Rapid communication High-precision measurement of the temperature of methanol and ethanol droplets using spontaneous Raman scattering," vol. 158, 2000, pp. 155–158.

[15] Hopkins, R. J., Symes, R., Sayer, R. M., and Reid, J. P., "Determination of the size and composition of multicomponent ethanol/water droplets by cavity-enhanced Raman scattering," *Chemical Physics Letters*, vol. 380, 2003, pp. 665–672.

[16] Nozaki, T., Mochizuki, T., Kaji, N., and Mori, Y. H., "Application of liquid-crystal thermometry to drop temperature measurements," *Experiments in Fluids*, vol. 18, 1995, pp. 137–144.

[17] Richards, C. D., Richards, R. F., and Boltzman, S., "Transient temperature measurements in a convectively cooled droplet," vol. 25, 1998.

[18] Mochizuki, T., Nozaki, T., Mori, Y. H., and Kaji, N., "Heat transfer to liquid drops passing through an immiscible liquid medium between tilted parallel-plate electrodes," *International Journal of Heat and Mass Transfer*, vol. 42, 1999, pp. 3113–3129.

[19] Tuckermann, R., Bauerecker, S., and Cammenga, H. K., "IR-Thermography of Evaporating Acoustically Levitated Drops," *International Journal of Thermophysics*, vol. 26, Sep. 2005, pp. 1583–1594.

[20] Wulsten, E., and Lee, G., "Surface temperature of acoustically levitated water microdroplets measured using infra-red thermography," *Chemical Engineering Science*, vol. 63, 2008, pp. 5420–5424.

[21] Lemoine, F., and Castanet, G., "Temperature and chemical composition of droplets by optical measurement techniques : a state-of-the-art review," 2013.

[22] Hu, H., and Koochesfahani, M. M. M., "Molecular tagging velocimetry and thermometry and its application to the wake of a heated circular cylinder," *Measurement Science and Technology*, vol. 17, Jun. 2006, pp. 1269–1281.

[23] Gendrich, C., Koochesfahani, M., and Nocera, D., "Molecular tagging velocimetry and other novel applications of a new phosphorescent supramolecule," *Experiments in fluids*, vol. 23, 1997, pp. 361–372.

[24] Hu, H., and Koochesfahani, M. M., "Thermal effects on the wake of a heated circular cylinder operating in mixed convection regime," *Journal of Fluid Mechanics*, vol. 685, Oct. 2011, pp. 235–270.

[25] Hu, H., and Huang, D., "Simultaneous measurements of droplet size and transient temperature within surface water droplets," *AIAA journal*, vol. 47, 2009, pp. 813–820.

[26] Hu, H., Jin, Z., and Nocera, D., "Experimental investigations of micro-scale flow and heat transfer phenomena by using molecular tagging techniques," *Measurement Science and Technology*, vol. 21, 2010, p. 085401 (14pp).

[27] Omrane, A., Juhlin, G., Ossler, F., and Aldén, M., "Temperature measurements of single droplets by use of laser-induced phosphorescence," *Applied optics*, vol. 43, 2004, pp. 3523–3529.

[28] Omrane, A., Santesson, S., Alden, M., and Nilsson, S., "Laser techniques in acoustically levitated micro droplets.," *Lab on a chip*, vol. 4, Aug. 2004, pp. 287–91.

[29] Ramamurthy, V., and Schanze, K. S., *Organic and inorganic photochemistry*, 1998.

[30] Kim, H. J., Kihm, K. D., and Allen, J. S., "Examination of ratiometric laser induced fluorescence thermometry for microscale spatial measurement resolution," *International Journal of Heat and Mass Transfer,* vol. 46, Oct. 2003, pp. 3967–3974.

[31] Hu, H., and Koochesfahani, M., *A Novel Technique for Quantitative Temperature Mapping in Liquid by Measuring the Lifetime of Laser Induced Phosphorescence*, 2003.

[32] Hu, H., and Koochesfahani, M., "Molecular tagging velocimetry and thermometry and its application to the wake of a heated circular cylinder," *Measurement Science and Technology,* vol. 17, 2006, pp. 1269–1281.

[33] Hartmann, W., Gray, M., and Ponce, A., "Substrate induced phosphorescence from cyclodextrin· lumophore host-guest complexes," *Inorganica Chimica Acta*, vol. 234, 1996, pp. 239–248.

[34] Hu, H., Koochesfahani, M., and Lum, C., "Molecular tagging thermometry with adjustable temperature sensitivity," *Experiments in fluids,* vol. 40, 2006, pp. 753–763.

[35] Hu, H., and Jin, Z., "An icing physics study by using lifetime-based molecular tagging thermometry technique," *International Journal of Multiphase Flow,* vol. 36, 2010, pp. 672–681.

[36] Saga, T., Kobayashi, T., Segawa, S., and Hu, H., "Development and evaluation of an improved correlation based PTV method," *Journal of Visualization,* vol. 4, Mar. 2001, pp. 29–37.

[37] Incropera, F., and Dewitt, D., "Introduction to heat transfer, 1996," *John WHey & Sons. New York. NY*.

[38] Whitaker, S., "Forced convection heat transfer correlations for flow in pipes, past flat plates, single cylinders, single spheres, and for flow in packed beds and tube bundles," *AIChE Journal*, vol. 18, Mar. 1972, pp. 361–371.

CHAPTER 3
AN EXPERIMENTAL INVESTIGATION ON THE EFFECTS OF SURFACE HYDROPHOBICITY ON THE ICING PROCESS OF IMPACTING WATER DROPLETS

3.1 Introduction

Aircraft icing is widely recognized as a significant hazard to aircraft operations in cold weather. When an aircraft or rotorcraft flies in certain climates, some of the supercooled droplets in the air would impact and freeze on the exposed aircraft surfaces and form ice shapes. Ice may accumulate on every exposed frontal surface (under some conditions, the ice even accumulate at the back part of the airfoil) of an airplane, not only on the wing, propeller and windshield, but also on the antennas, vents, intakes, and cowlings. Icing accumulation can degrade the aerodynamic performance of an airplane significantly by decreasing lift while increasing drag. In moderate to severe conditions, an airplane could become so iced up that continued flight is impossible. The airplane may stall at much higher speeds and lower angles of attack than normal. It could roll or pitch uncontrollably, and recovery may be impossible. Ice can also cause engine stoppage by either icing up the carburetor or, in the case of a fuel-injected engine, blocking the engine's air source. The importance of proper ice control for aircraft operation in cold climate was highlighted by many aircraft crashes in recent years like the ATR-72 aircraft of American Eagle flight crashed in Roselawn, Indiana due to ice buildup on its wings killing all 66 people aboard on October 31, 1994. After investigation, it was found that the aircraft encountered the supercooled large droplets (SLD) icing environment, which didn't be defined in Appendix

C of Part 25 of Federal Aviation Regulations (FAR25 Appendix C), and the aircraft crashed for the abnormal icing on airfoils[1]. The study of atmosphere shows that the diameter of droplet in the SLD icing environment could vary from 40μm to 1000μm, and it is far beyond 40μm that defined in FAR25[2]. The deicer equipment designed based on the FAR 25 Appendix C is not suitable for the SLD icing environment. For expanding the airworthiness regulations application scope of icing environment, it is important and necessary to elucidate the underlying physics of SLD icing.

The recent researches on superhydrophobic surfaces demonstrated that the superhydrophobic coatings have ice phobic properties[3], as the droplets can bounce off of cold superhydrophobic surfaces without freezing[4] and the superhydrophobicity directly implies anti-icing functionality[5]. Therefore, utilizing the superh ydrohopbic surfaces could be a reasonable way to manage the water runback phenomenon and decrease or eliminate the back-part icing on airfoil. Superhydrophobic surfaces have been extensively studied because they exhibit a number of interesting properties such as extremely high static contact angles (e.g., >150˚), small contact angle hysteresis, droplets rolling off at shallow surface angles, and droplets bouncing on impact[6–10]. These properties of superhydrophobic surfaces leads to self-cleaning behavior, whereby water droplets quickly roll off the surface and carry with them any other contaminates-including other droplets-they encounter. The superhydrophobicity of the surface results from a combination of chemical hydrophobicity with a micro or nano textured surface. The structure of the surface plays an important role both in the wettability of the surface and in the ability of the surface to resist ice accretion[3].

Current ice prediction tools for airfoil icing like LEWICE and FENS AP-ICE make use of simple classical models that ignore many details of the important micro-physical processes that responsible of the icing formation and accretion on airfoil[11,12]. Developing the technology for safe operation in SLD icing condition requires a better understanding of the important micro-physical phenomena pertinent to SLD icing. Several studies have been carried out recently to simulate ice accretion on airfoil icing through icing wind tunnel testing or calculations. NASA Glenn icing research tunnel analyzed the ice sharp profiles in different icing conditions by measuring the ice accretion on NACA 0012 airfoil[13]. Iowa State icing wind tunnel researched the ice accretion process, the heat transfer process, and the surface water transport process over an icing accreting NACA 0012 airfoil[14,15,16]. Wright and Potapczuk simulate ice accretion on airfoil thought calculation[17] by importing droplet impinging tentative mass model[18]. Very few studies could be found in literature to elucidate the underlying physics of SLD icing. The fundamental studies of SLD icing process could provide detailed information to analyze ice formation and ice-growth physical processed such as SLD dynamics, unsteady heat transfer process within supercooled water or ice crystals, which are highly desirable in elucidate the underlying physics associated with the micro-physical processes.

In the present study, an experimental investigation was conducted to quantify the unsteady heat transfer and phase change process of icing while droplet impinging onto different kinds of icing plate as hydrophilic and hydrophobic substrates in order to elucidate underlying physics to improve our understanding of the important micro-physics processes pertinent to SLD icing on aircraft wings. The high speed imaging technique was

implemented to record the dynamic phase changing process while the infrared thermometry imaging technique was implemented to achieve temporally-and-spatially resolved temperature distribution measurements to reveal the time evolution of the unsteady heat transfer within SLD in the course of icing. A better understanding of the important micro-physical processes would enable us to improve current icing accretion models for more accurate prediction of ice formation and ice accretion on aircraft wings and to develop effective and robust anti-/de-icing strategies to ensure safer and more efficient operation of aircraft in cold weather.

3.2 Experimental Methods

3.2.1 Experimental setup

Figure 3.1 shows the schematic of the experimental setup used in present study to implement the high speed imaging technique and infrared thermometry imaging technique to quantify unsteady heat transfer and phase change process during droplet impact process to elucidate underlying physics of micro-physical process of droplet impact and icing phenomena.

The experimental setup was comprised of several subsystems, a droplet generator system, a droplet impact substrate system, a high speed imaging system, an infrared imaging system.

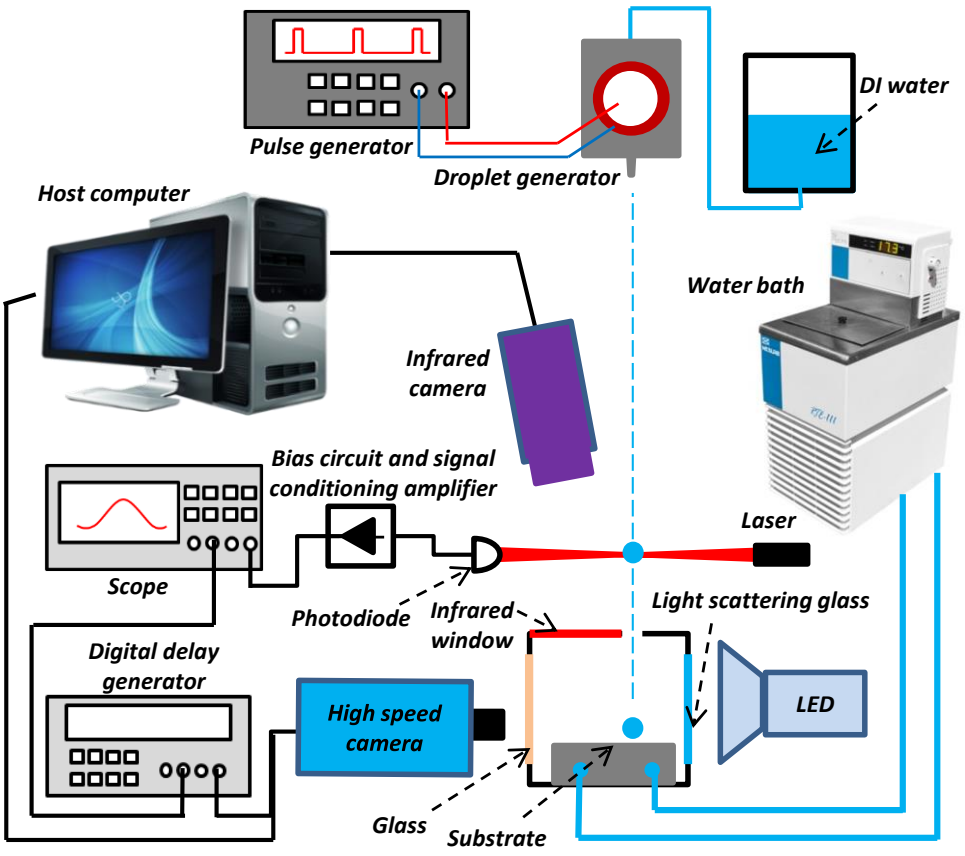

Figure 3.1 Schematic of the experimental setup for measuring droplet impingement and ice accretion

3.2.2 Droplet generator system

A volume type of droplet generator system was used to generate the mono water droplet needed in the experiment. The system includes three parts – main part, pulse generator, and water supplement bottle. As shown in figure 3.2, the main part of the droplet generator system was combined by a water cavity, a piezoelectric plate and a nozzle. The water cavity and nozzle were made by 3-D printer. The water cavity was covered by the piezoelectric plate, and connected with the water supplement bottle with a water tube. During experiment, the water upper surface in the bottle was controlled at a level which is

a little higher than the nozzle of the generator to ensure that the water cavity was full of water, while the water was not outflow from nozzle due to the capillary effect of the nozzle. After receiving signal from the pulse generator, the piezoelectric plate would warp and squeeze the water cavity, and then the droplet was ejected from the nozzle. With suitable pulse voltage and frequency, the droplet generator can eject only one droplet with one single pulse. The droplet size was controlled by the nozzle inner diameter and the pulse voltage while the droplet impact velocity was controlled by the initial ejective velocity when droplet leaving the nozzle and the perpendicular distance between the droplet generator and the solid impact substrate. The droplet size can vary from about 0.5mm to 2.5mm by using different inner diameter nozzles and different pulse voltages, while the impact velocity of the droplet can vary from about 1m/s to 5m/s. To avoid the impurities', disturb to the impact and icing process, the water used in the experiment was deionized water.

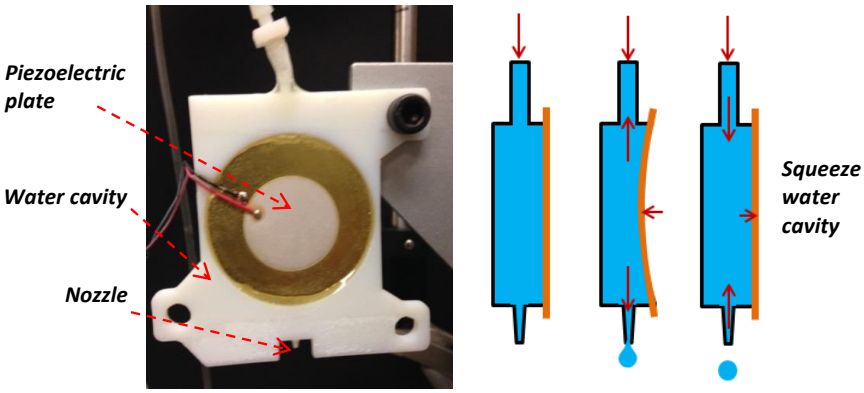

Figure 3.2 Main part of the droplet generator system

3.2.3 Droplet impact substrate system

The droplet impact substrate system was combined by an impact substrate and a cooling plate. As shown in figure 3.3, the cooling plate was connected with a water bath

(NESLAB RTE-211). by two tubes covered by heat adiabatic layer. With the help of the cyclic coolant, the cooling plate temperature was controlled by the water bath. The impact substrate was set on the cooling plate and connected each other by thermally conductive silicone, so that the substrate surface temperature can also be controlled, and the temperature was controlled precisely from -8˚C to 20˚C.

Condensation can effectively change the wettability of a solid surface[19,20]. In order to avoid condensation on the solid substrate and to control the substrate temperature more precisely, the substrate was mounted in a relatively closed experimental cell, as shown in figure 3.1. A light scattering glass was mounted at the rear part of the experimental cell, a high transmitting glass was mounted at the front part of the cell, and an infrared window was mounted at the top part of the cell. The only opening of the experimental cell was used for the entry of the in-flight droplet.

Since the impact substrate was connected with the cooling plate by thermally conductive silicone, it is easy to change the substrate surface properties by using different substrates. Both of the hydrophilic and superhydrophobic surfaces were used for investigation of droplet impact and icing. The hydrophilic surface was coated in a wet-sanded Rustoleum finished with a static water contact angle of 65˚. The superhydrophobic surface was given the Hydrobead (Hydrobead.com) superhydrophobic treatment, and the static contact angle is about 157˚.

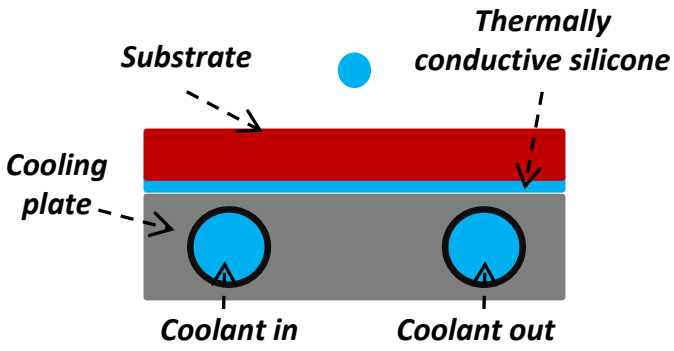

Figure 3.3 Schematic of the droplet impingement solid substrate

3.2.4 High speed imaging system

The high speed imaging system was combined by a high speed camera and a laser detecting system. As shown in figure 3.1, a high-speed camera (PCO tech dimax HS) with a micro lens (Nikon Nikkor 60mm 2.8/D) was configured parallel to the surface of the solid substrate. Diffuse backlighting was provided by a 20W LED spotlight and the light scattering glass at the rear part of the experimental cell. The laser detecting system includes five parts – a laser, a photodiode, a bias circuit and signal conditioning amplifier, a digital storage oscilloscope (Rigol 1074Z), and a digital delay generator. When a droplet was released from the droplet generator, it crossed the diode laser beam, disrupting the signal to the photodiode whose signal was amplified and read out by the digital storage oscilloscope. The trigger from the oscilloscope initialed the digital delay generator that controlled timing and exposure of the high-speed camera. The frame rate was set as 10000 fps while the image resolution is 624 by 608 pixels.

3.2.5 Infrared imaging system

A FLIR A600 serious infrared camera was used to measure the droplet temperature variation during the droplet impact and icing process. The frame rate was set as 200 fps

while the image resolution is 640 by 120 pixels. The infrared camera was mounted above the solid substrate at a distance of 200mm, and the infrared radiation from the substrate surface and water/ice can be transmitted through the infrared window with a transmission coefficient of 0.82. The emissivity coefficients of hydrophilic and superhydrophobic surfaces, water, and ice are listed in Table 3.1, respectively. It shows that the emissivity of the hydrophilic surface, the superhydrophobic surface, water and ice are nearly same. For the infrared camera, a calibration was done by using thermocouple. A correlation coefficient of 99.94% was achieved, validating the infrared tomography in achieving accurate temperature measurements over the surface of the impingement droplet surface.

Table 3.1 Emissivity coefficients of materials used in the measurements

Material	Emissivity
Hydrophilic surface	0.96
Superhydrophobic surface	0.96
Water	0.95-0.963
Ice	0.966(smooth) ~ 0.985(rough)

3.3 Measurement Results and Discussions

3.3.1 Characteristics of the two compared propeller surfaces with significant different wettability

As described above, the two different kinds impact substrates with significant differences in surface wettability were prepared for the present study. The contact angles of sessile water droplets over the two compared surfaces were measured by using the

similar procedure as described in Waldman et al.[21]. As shown clearly in figure 3.4(a), the contact angle of the water droplets sitting on the hydrophilic surface is obviously smaller than 90° (i.e., measured $\theta \approx 65°$). The measured contact angle of water droplets on the superhydrophobic surface was found to be about 157° as shown in figure 3.4(b).

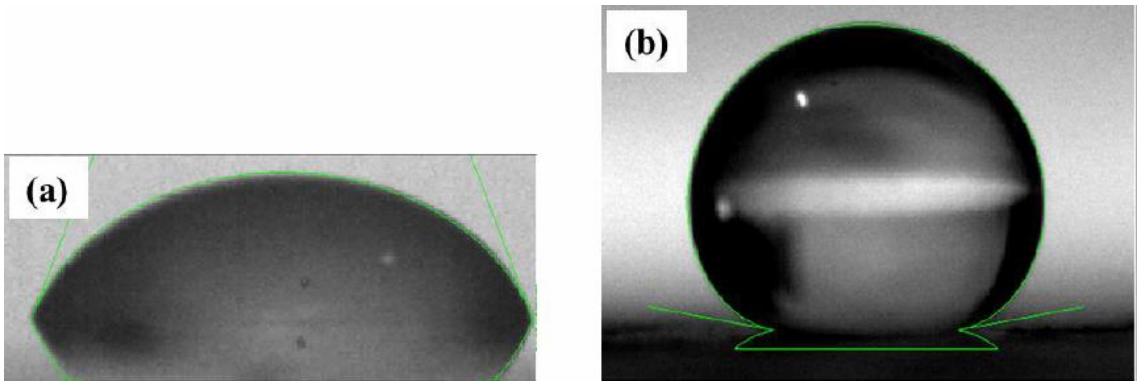

Figure 3.4 Water droplets on compared surfaces: (a) Hydrophilic surface; (b) Superhydrophobic surface.

By using a similar needle-in-the-sessile-drop method as described in Korhonen et al.[22], the advancing and receding angles of water droplets (i.e., $\theta_{advancing}$ and $\theta_{receding}$) over the two compared impact surfaces were also measured in the present study. Table 3.2 summarizes the measured advancing and receding angles of the water droplets on the two studies surfaces. While the contact angle hysteresis (i.e., the difference between the advancing and receding contact angles of the water droplet, $\Delta\theta = \theta_{advancing} - \theta_{receding}$) for the hydrophilic surface was found to be greater than 50°, the contact angle hysteresis for the superhydrophobic surface was found to be very small, which is smaller than 5° (i.e., $\Delta\theta < 5°$).

Table 3.2 The measured surface properties of the two impact substrates

Compared surface Wettability	**Static contact angle** θ_{static}	**Advancing contact angle** $\theta_{advancing}$	**Receding contact angle** $\theta_{receding}$	**Hysteresis** $\Delta\theta = \theta_{advancing} - \theta_{receding}$
Hydrophilic	~45°	~85°	~30°	>50°
Superhydrophobic	~157°	~159°	~154°	<5°

3.3.2 Droplet impact on hydrophilic and superhydrophobic surfaces under normal temperature

In this part, the normal temperature water droplet (i.e. $T_s = 23.5℃$) dynamic impact process recorded by using high speed imaging technique and the impact water droplet upper surface temperature variation process recorded by using thermometry imaging technique during the impact and cooling processes on the non-icing temperature (i.e. $T_s = 5℃$) hydrophilic and superhydrophobic substrates would be discussed. Both of the environment temperature (air in the experimental cell) and droplet temperature before impacting were measured as 23.5℃. The droplet diameter is 1.64mm with an impact velocity of 3.7m/s, which made the Reynolds number and Weber number be 6109 and 319, respectively. The Reynolds number and Weber number are defined as:

$$\mathrm{Re} = \frac{\rho U_0 D_0}{\mu} \tag{3.1}$$

$$We = \frac{\rho U_0^{\,2} D_0}{\gamma} \tag{3.2}$$

Where *Re* is the Reynolds number, ρ is the water droplet density, U_0 is the droplet velocity before impacting on the substrates, D_0 is the droplet initial diameter, μ is the

droplet dynamic viscosity, *We* is the Weber number, γ is the droplet surface tension at the interface between water and air.

The impact of the water droplet begins at the time when the droplet starting contacting the substrate. As shown in figure 3.5(a) at the time of 0s, the impact droplet started contacting the substrate, and then the central part of the droplet kept decreasing while the bottom part kept expanding until it reached the maximum spreading diameter at the time of 0.0012s, and this process was called spreading process. After the bottom part of the droplet reached the maximum spreading diameter, the outside part of the droplet would recede back to the central part, thus, the central part would increase while the outside part would decrease, and this process was called receding process. The receding process would end at the time when the droplet central part reaches a maximum height, as shown in figure 3.5(a), the receding process ended at 0.008s. The dynamic process of the impact droplet after the receding process can be considered as switches between spreading and receding processes until the droplet was finally be static on the impact substrate. During this process, the central part of the droplet would decrease and increase again and again, while the outside part would increase and decrease again and again, while the increase and decrease phenomenon become less and less obvious. As shown in figure 3.5(a), the whole time used for the droplet dynamic process was about 0.8s.

As shown in figure 3.5(b), when the droplet impact on the superhydrophobic surface, the spreading process was similar to that on the hydrophilic surface, and the droplet would reach the maximum spreading diameter at a similar time of 0.0012s as that on hydrophilic surface. However, the receding process was much more different comparing with that on

hydrophilic surface. For example, a much more obvious droplet receding and rebounding phenomenon was found when droplet impact on the superhydrophobic surface. These different receding processes are due to the huge gap between the capillary forces at the contact line of water droplet, air and solid substrate on hydrophilic and superhydrophobic surface. As described in Bartolo D et al. (), the capillary force dominating receding phenomenon can be calculated as:

$$F_c = \pi\gamma D_{\max}\left(1-\cos\theta_r\right) \tag{3.3}$$

where F_c is the capillary force, γ is the surface tension at the interface between water droplet and air, D_{max} is the maximum spreading diameter, θ_r is the receding contact angle on the surface. Since the maximum diameters of the droplet has similar initial diameter and impact velocity water droplet are similar, thus, the maximum difference of the capillary force on hydrophilic and superhydrophobic surface is due to the receding contact angle θ_r. Based on the measured receding contact angles given in Table 3.2, the ratio between the capillary forces acting at the contact line on the hydrophilic and superhydrophobic surfaces can be estimated with euqition 3.3, which can be expressed as:

$$\frac{F_{c,superhydrophobic}}{F_{c,hydrophilic}} \approx \frac{\left[1-\cos\theta_r\right]_{superdrophobic}}{\left[1-\cos\theta_r\right]_{hydrophilic}} \approx 14 \tag{3.4}$$

It reveals clearly that, in comparison with those acting on water droplets on the hydrophilic surface, the capillary forces acting on the water droplets with same maximum spreading diameter over superhydrophobic surface were found to be much bigger (i.e. 14 times). Therefore, with a much bigger capillary force, the droplet could recede back much easier, and the recorded images even showed that the droplet rebounded from the impact

substrate. Comparing with that on hydrophilic surface, the dynamic time for the droplet on superhydrophobic surface was much shorter, as shown in figure 3.5 (b), the time was only 0.2s, which is just $1/4^{th}$ of that on hydrophilic surface.

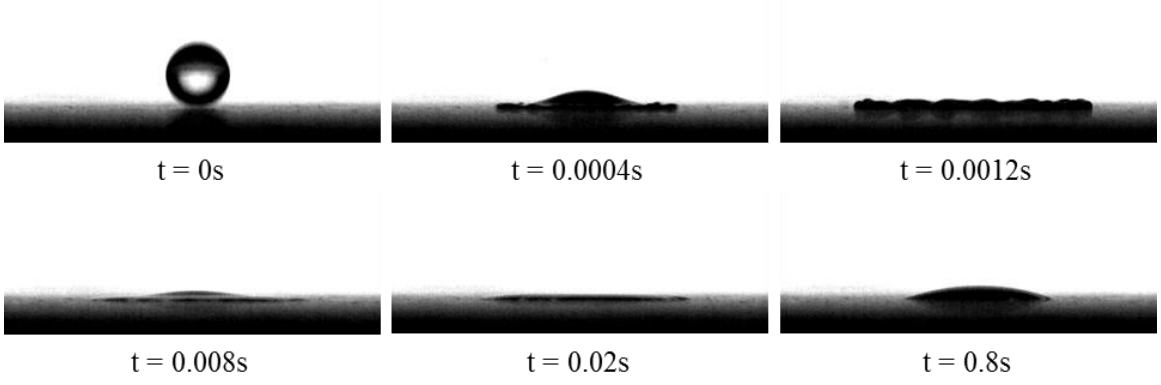

(a) Hydrophilic surface

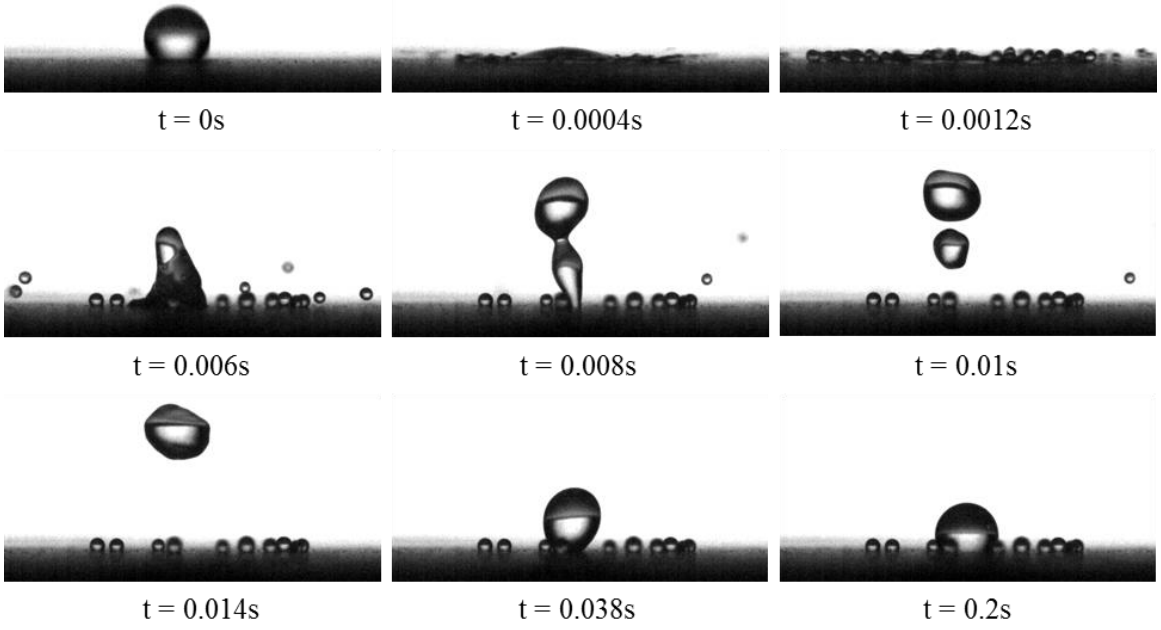

(b) Superhydrophobic surface

Figure 3.5 Droplet impact process on the normal temperature substrates

Figure 3.6(a) shows the surface temperature variation of the impact droplet on the hydrophilic surface under normal temperature. It is needed to note that the frame rate of the infrared images was only 200fps, so that the time delay between each recorded adjacent thermometry image is 0.02s, which is longer than the spreading process (i.e. 0.0012s) of the droplet impact in the present study, thus, the thermometry image cannot show the temperature variation clearly during the spreading process. The infrared images in Figure 3.6(a) showed that the surface temperature of the impingement droplet decreased gradually and the time needed to cool all the droplet to substrate temperature is about 1.5s. Figure 3.7(a) shows the circumferentially-averaged surface temperature of the droplet versus the radial position. While the average temperature is defined as:

$$\bar{T}(t) = 1/(2\pi)\int_0^{2\pi} T(r,\theta,t)d\theta \tag{3.5}$$

where r and θ are the usual cylindrical coordinates, t is the time after the onset of the droplet impact. It shows that the temperature at the outside surface part (shorter distance to the cool substrate) of the droplet surface decreased faster than that at the central part (longer distance to the cool substrate), and the central point was the last point to decrease to 5˚C, which certified that the heat transfer direction is from the warmer upper part of the droplet to the cooler bottom part of the droplet, and then to the cool substrate. The time for cooling the droplet is about 2 times of the droplet dynamic impact time.

Figure3.6(b) shows the surface temperature variation of the impact droplet on the superhydrophobic surface under normal temperature. The contact angle of water on the superhydrophobic surface is about 157˚, so that the lower part of the droplet was blocked by the upper part for the thermometry images. Although the infrared images can just show

the temperature variation of the upper part of the droplets, it still clearly shows the droplet splash phenomenon. For the small droplets generated during the droplet splash process, the time needed to cool is much shorter than that of the main droplet. For example, the small droplet temperature already decreased to 5˚C at about 2.63s, while the main droplet did not cool to 5˚C until after 10s. Figure 3.7(b) shows circumferentially-averaged surface temperature of the main droplet generated after splash versus the radial position on the superhydrophobic surface. It shows that the surface temperature decrease gradually, and the time for the heat transfer is more than 50 times of the droplet dynamic impact time.

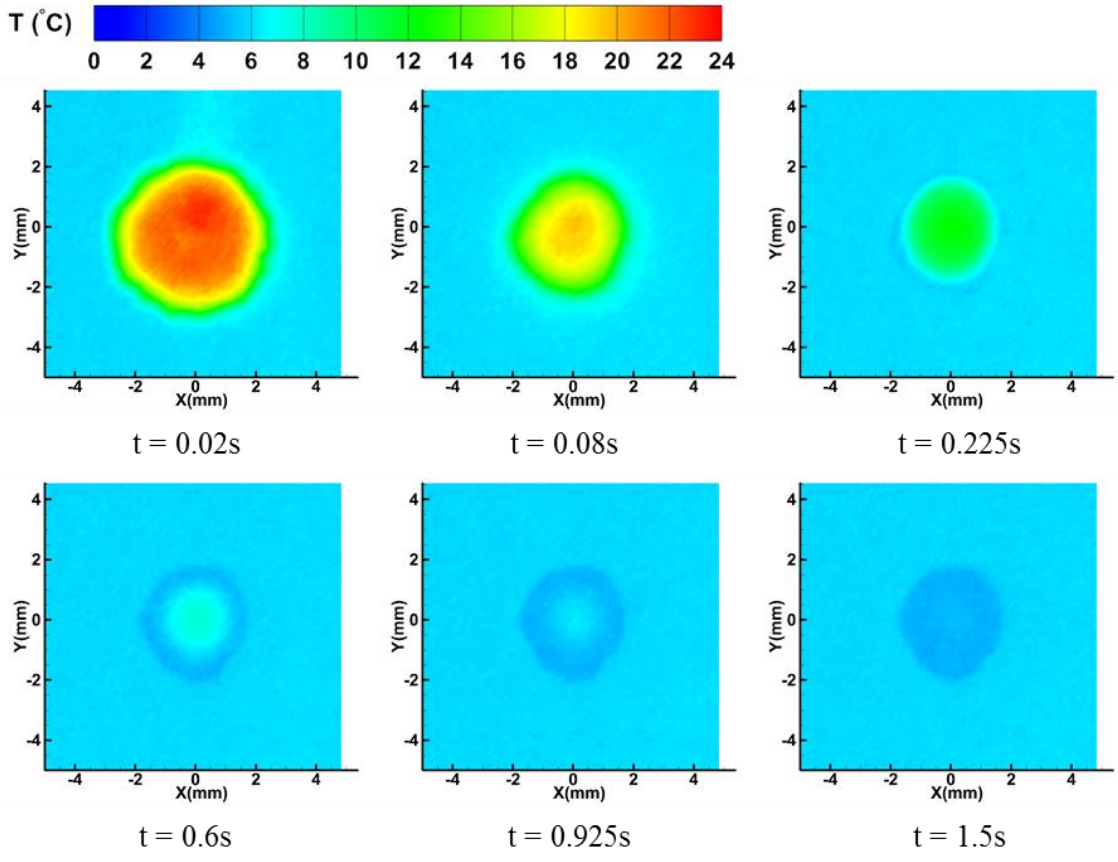

(a) Hydrophilic

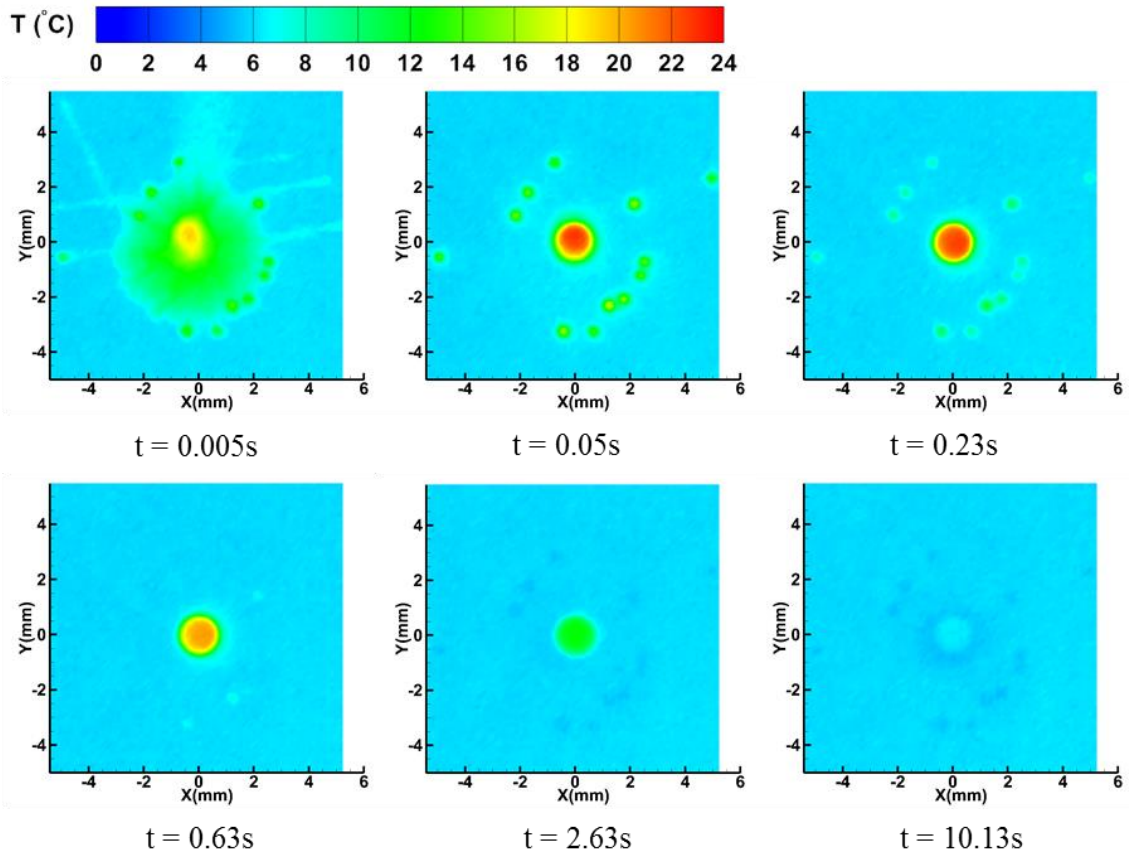

(b) Superhydrophobic

Figure 3.6 The surface temperature variation of the impact droplet on the normal temperature substrates

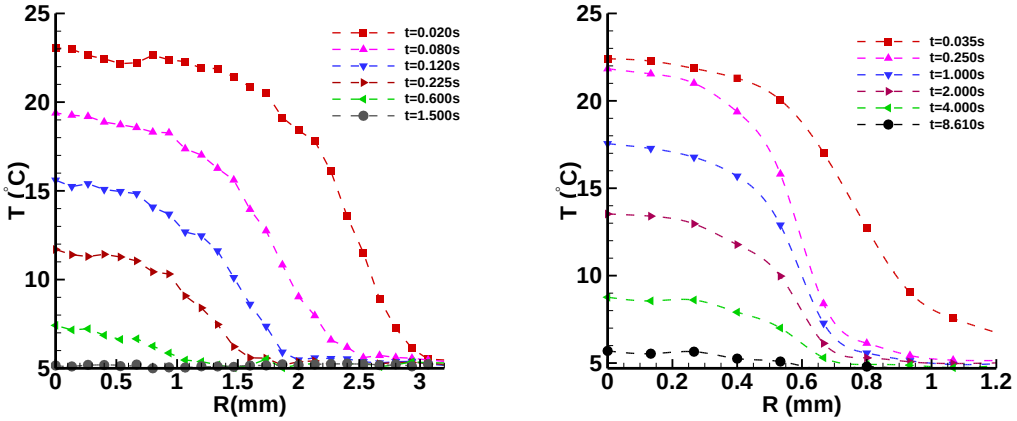

(a) Hydrophilic (b) Superhydrophobic

Figure 3.7 The circumferentially-averaged surface temperature on the normal temperature surfaces of the impact droplet during cooling process

Figure 3.8 shows the temperature variation at the central point of the surface of the impact droplet on hydrophilic and superhydrophobic surfaces under normal temperature. It shows that both of the central point (top point) temperature decreased gradually without obvious temperature fluctuation, while the time needed to cool the droplet on the superhydrophobic substrate is much longer than that on the hydrophilic substrate. As shown in figure 3.8, the time of the superhydrophobic situation is more than 10s, while that of the hydrophilic situation is only about 1.5s. As the above discussions, the time needed to cool the impact droplet is much longer than the droplet dynamic impact time, so that the contact area between the impact droplet and the cool substrate after the dynamic impact process is a very important parameter to the heat transfer speed between the water and the surface. With a much more obvious receding process (as discussed in part 3.3.1), the droplet impacting on superhydrophobic surface could reduce to a much smaller diameter, thus, the diameter of the droplet when it was static on the superhydrophobic surface is much smaller than that on the hydrophilic surface. As shown in table 3.3, the final diameter D_f of the impact droplet on superhydrophobic is only 1.67mm, and the corresponding final contact area A_f was 1.22mm^2, while the final diameter of the impact droplet on hydrophilic surface is 3.96mm, and the corresponding contact area was 12.30mm^2. With a much smaller contact area, the height of the droplet when it was static on the superhydrophobic surface was larger than that on hydrophilic surface, as shown in Table 3.3, the heightswere 1.22mm and 0.44mm on the superhydrophobic and hydrophilic surfaces, respectively. Thus, with a much smaller heat transfer area and a longer heat

transfer distance, the heat transfer speed in the droplet on superhydrophobic surface was smaller than that on hydrophilic surface.

Table 3.3 The final receding diameter/area/height of the impingement droplet on hydrophilic and superhydrophobic surfaces under normal temperature

Surface	D_f (mm)	A_f (mm^2)	Height (mm)
Hydrophilic	3.96	12.32	0.44
Superhydrophobic	1.46	1.67	1.22

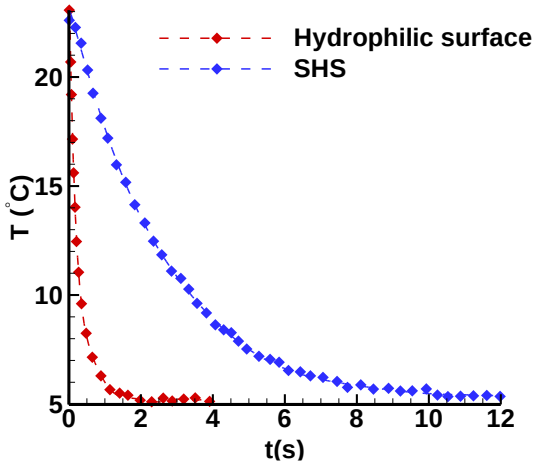

Figure 3.8 The temperature variation of the central point of the surface of the impact droplet on hydrophilic and superhydrophobic surface (SHS)

3.3.3 Droplet impact on hydrophilic and superhydrophobic surfaces under icing temperature

In this part, the normal temperature water droplet (i.e. $T_s = 23.5℃$) dynamic impact process recorded by using high speed imaging technique and the impact water droplet upper surface temperature variation process recorded by using thermometry imaging technique during the impact and cooling processes on the icing temperature (i.e. $T_s = -5℃$) hydrophilic and superhydrophobic substrates would be discussed. Both of the

environment temperature (air in the experimental cell) and droplet temperature before impacting were measured as 23.5℃. The droplet diameter is 1.64mm with an impact velocity of 3.7m/s, which made the Reynolds number and Weber number be 6109 and 319, respectively.

Figure 3.9(a) shows the droplet dynamic impact process on the hydrophilic surface under icing temperature. The dynamic impact process was similar to that on the normal temperature hydrophilic surface except the receding process. When droplet impact on the normal temperature hydrophilic surface, it would recede back a little after reaching the maximum spreading diameter, however, when the droplet impact on the icing temperature hydrophilic surface, the interface between droplet and solid surface would freeze, thus, the droplet bottom part wouldn't recede back, so that the final diameter of the droplet after the impact process on the icing temperature hydrophilic surface would larger than that on the normal temperature hydrophilic surface.

Figure 3.9(b) shows the droplet dynamic impact process on the superhydrophobic surface under icing temperature. Comparing with that on the normal temperature superhydrophobic surface, the dynamic process on the icing temperature superhyophobic surface seems similar, except the disappear of the splash phenomenon. Even though with an icing temperature substrate, the droplet still showed an obvious receding process when impacting on the superhyrophobic surface compare with that on the hydrophilic substrate, which illustrated that the superhydrophoic surface could effectively reduce the icing process at the bottom of the droplet.

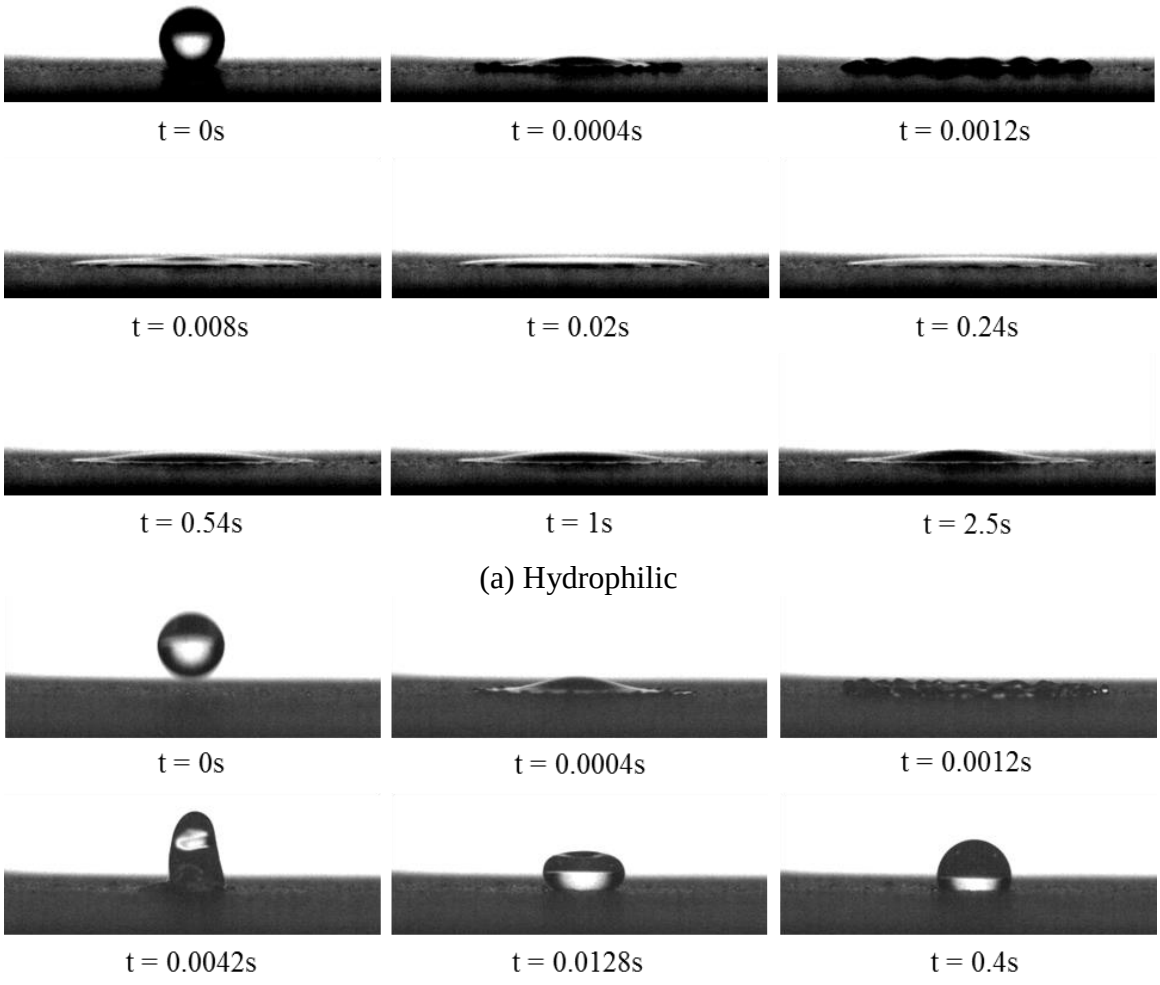

(a) Hydrophilic

(b) Superhydrophobic

Figure 3.9 Droplet impact process on the icing temperature substrates

Figure 3.10(a) shows the surface temperature variation of the impingement droplet on the hydrophilic surface under icing temperature during the droplet dynamic impact process and icing process, while the figure 3.11(a) shows the circumferentially-averaged surface temperature of the impact droplet on the hydrophilic surface under icing temperature. As discussed in the above sections, at 0.02s, the impact droplet just finished its second spreading process and started the second receding process, which could also be verified by

the infrared image. As shown in the image of t=0.02s in figure 3.10(a) and figure 3.11(a), the temperature of the center part of the impingement droplet was lower than that around the center part, which means that the surface of the center part was lower than that around the center part. From the time of 0.02s to the time of 0.27s, the central part temperature kept decreasing to about -1.5˚C, while the part around the central part temperature would decrease to a temperature lower than 0˚C and then went back to 0˚C. For example, from 0.095s to 0.175s, the temperature of the part about 1.75mm away from the central point decreased from about 2.5˚C to about -2˚C, and then increased to 0˚C at 0.27s. After all the temperature of the water in the impingement droplet decreased to 0˚C, the temperature of the water would keep at 0˚C before freezing. The temperature lower than 0˚C means that the surface part already frozen, and the temperature increased to 0˚C again means that the water not frozen yet covered the frozen part in the second receding process. At 0.535s, the temperature of the central point on the surface of the impingement droplet increased to 0˚C again, which means that the water not frozen yet receded back to the central point. From 0.535s to about 3s, the central point temperature would keep at 0˚C for about 2.5s while the part around the central point would decrease to the temperature lower than 0˚C from outside part to the central part. After the time of 3s, the central point temperature would decrease, which means that all the water in the impingement droplet frozen. After 3s, all the ice would be cooled to -5˚C in a relatively short time. The impingement droplet would be cooled to -5˚C after a short morphologic change process and a relatively long phase change process at the time of 3.35s. By comparing with the temperature variation process

on the hydrophilic surface under normal temperature, the temperature variation process was much more complicated for the phase change during the process.

Figure 3.10(b) shows the surface temperature variation of the impingement droplet on the superhydrophobic surface under icing temperature during the droplet morphologic change process and phase change process, while the figure 3.11(b) shows temperature variation of the impingement droplet on the superhydrophobic surface under icing temperature. The infrared images show that the surface temperature variation after 0.03s was quite gradually, and the time needed for the impingement droplet to cool down on superhydrophobic surface was relatively longer than that on hydrophilic surface. Figure 3.11(b) shows that the temperature on the surface of the impingement droplet was still -3˚C at the time of 10s, which is higher than the substrate temperature. By comparing with the high-speed images in figure 3.9(b), the morphologic change process for the impingement droplet on superhydrophobic surface was much shorter than the phase change process or the temperature variation process. With a much shorter morphologic process, the temperature variation process was much easier for the superhydrophobic situation than that of the hydrophilic situation. Figure 3.11(b) shows that the temperature decreased gradually without any temperature fluctuation even after the temperature was lower than 0˚C.

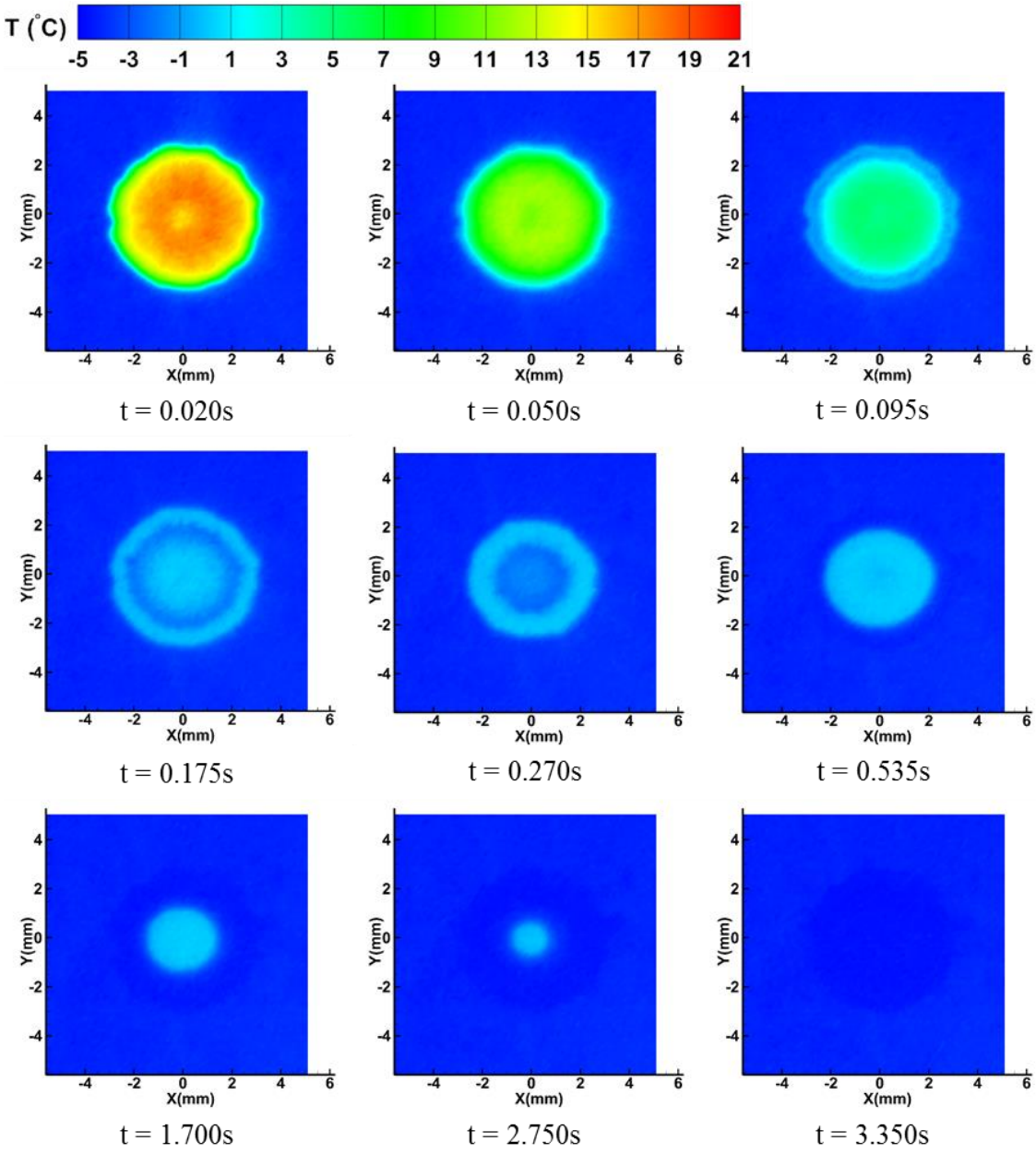

(a) Hydrophilic

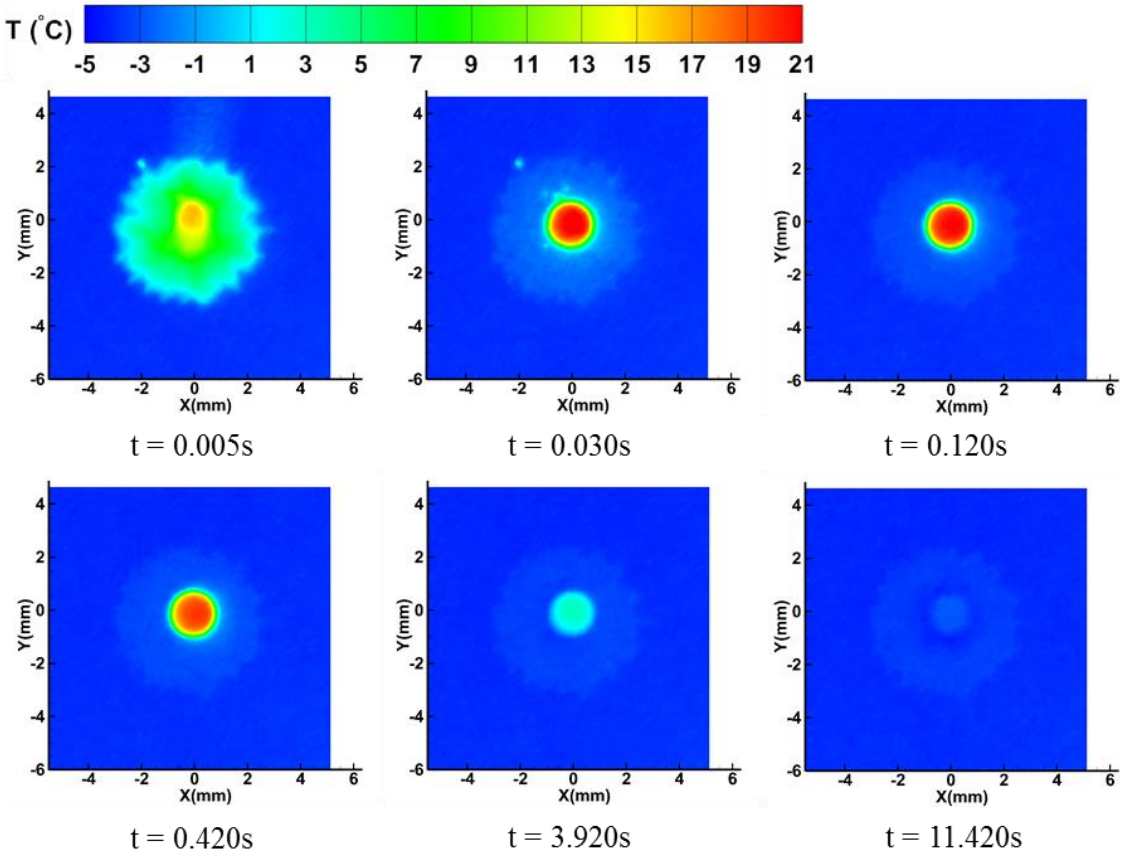

(b) Superhydrophobic

Figure 3.10 The surface temperature variation of the impact droplet on the icing temperature substrates

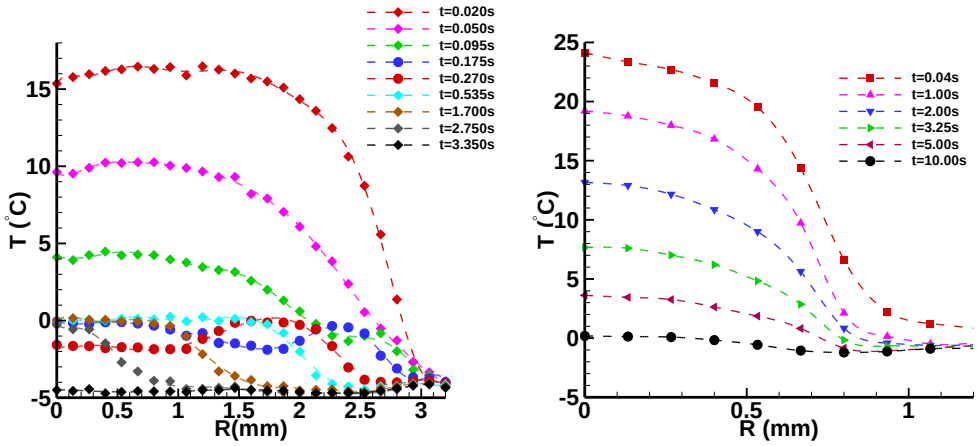

(a) Hydrophilic (b) Superhydrophobic

Figure 3.11 The circumferentially-averaged surface temperature of the impact droplet during the cooling process

Figure 3.12 shows the heat transfer direction during the phase change process of icing for the impingement droplet on the icing substrate. The substrate temperature was -5˚C, the temperature of the interface of water and ice was 0˚C, the water temperature was also 0˚C, and the air temperature around the impingement droplet (the infinity temperature) was 23.5˚C. Based on the second law of thermodynamics, all the latent heat released by the icing at the interface would transfer to the bottom ice without transferring to the water above the interface, otherwise the water temperature above the icing interface would increase to a temperature higher than 0˚C, which leads to the stop of the phase change of icing. Moreover, the heat transfer directions are - from the warm air to the cold water and cold ice, from the water to the water/ice interface, from the water/ice interface to the bottom ice, and from the bottom ice to the substrate. Based on the heat transfer directions, the water above the interface could keep at 0˚C, and then the water/ice interface could keep increasing until all the water frozen. Based on the heat transfer directions, the icing would start at the bottom and end at the top point of the impingement droplet.

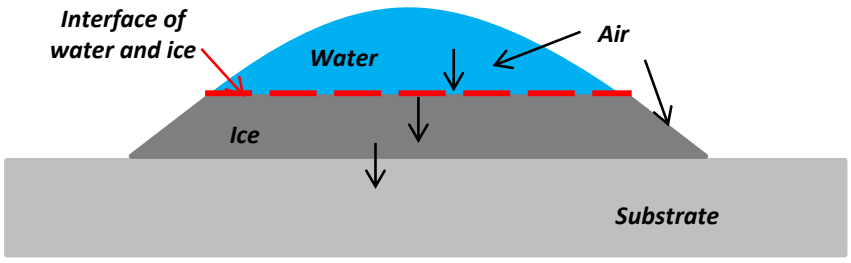

Figure 3.12 Heat transfer directions during the phase change process of icing

Figure3.13 shows the temperature variation of the central point on the surface of the impingement droplet on hydrophilic and superhydrophobic surfaces under icing temperature. For the hydrophilic situation, the temperature would decrease to about -2˚C

in about 0.27s, then increased back to 0˚C in 0.25s and kept at 0˚C for about 2.5s, and finally decreased to -5˚C in a very short time. The total time needed for the cooling process was 3.35s. As above discussions, the water not frozen yet covered the frozen part during the second receding process led to the temperature increasing back to 0˚C, and the reason for the temperature kept at 0˚C was the combined effect of the phase change process of icing and the cooling process. For the superhydrophobic situation, the temperature decreased gradually without obvious temperature fluctuation, and the temperature decreased to about -3.5˚C in 14s. As shown in Table 3.4, the final receding diameter of the impingement droplet on hydrophilic is 5.97mm, which led to a contact area of 28mm^2, while for the superhydrophobic surface, the final receding diameter was 1.73mm, and the contact area was 1.25mm^2. The height of the impingement droplet after the morphologic variation was 0.30mm and 1.25mm for the hydrophilic surface and the superhydrophobic surface, respectively. With a smaller heat transfer area and a longer heat transfer distance, the heat transfer speed between the impingement droplet and the cold surface was much lower.

Table 3.4 The final receding diameter/area/height of the impingement droplet on hydrophilic and superhydrophobic surfaces under icing temperature

Surface	D_r (mm)	A_f (mm^2)	Height (mm)
Hydrophilic	5.97	27.99	0.30
Superhydrophobic	1.73	2.35	1.25

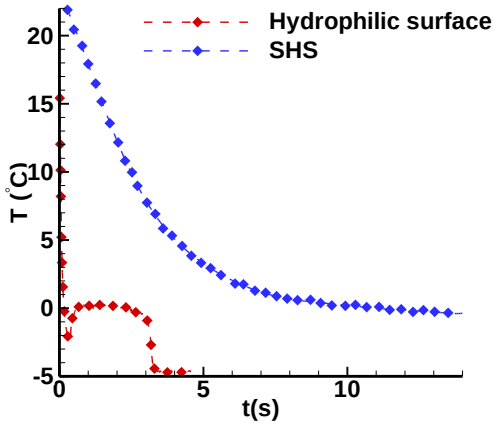

Figure 3.13 The comparison of the temperature variation processes at the central point of the droplets impacting on icing temperature hydrophilic and superhydrophobic substrates (SHS)

3.3.4 Influence of substrate temperature on heat transfer during droplet impingement process

In this part, the temperature variation of the impingement droplet surface central point on the hydrophilic surface under different temperature would be discussed. The hydrophilic surface temperature was set as 5˚C, -1.5˚C, and -5˚C, respectively. The environment temperature (in the experimental cell) and droplet before impinging was 23.5˚C, and the droplet diameter was 1.64mm with an impingement velocity of 3.7m/s, which made the Reynolds number and Weber number be 6109 and 319, respectively.

Table 3.5 The final receding diameter/area/height of the impingement droplet on hydrophilic surfaces under different temperature

Temperature (˚C)	Ds (mm)	D_r (mm)	A_f (mm^2)
5	6.21	3.96	12.32
-1.5	6.19	5.73	25.79
-5	6.19	5.97	27.99

Table 3.5 shows the biggest spreading diameter, the final receding diameter and the contact area of the impingement droplet under different temperature. The biggest spreading diameter of the situations of 5˚C, -1.5˚C and -5˚C was 6.21mm, 6.19mm and 6.19mm, respectively, which was nearly equal to each other, and this means that the temperature did not has obviously influence to the first spreading process of the impingement droplet. However, the final receding diameter of the three situations had relatively big difference, especially between the normal temperature situation and the icing temperature situations. The final receding diameter of the -1.5˚C and -5˚C situation was 5.97mm and 5.73mm, respectively, while that of the 5˚C situation was 3.96mm. The phase change of icing at the bottom of the impingement droplet prevented the water/ice recede continually led to the big difference of the final receding diameter between normal and icing situations. With a big difference of the final receding diameter, the final contact area between impingement droplet and substrate had relatively bigger difference. The final contact area for the three situations was 12.3mm^2, 25.8 mm^2 and 28 mm^2, respectively. For a same initial diameter impingement droplet, if the contract area increased, the height of the impingement on the substrate would decrease, which led to a higher heat transfer speed from the bottom of the impingement to the cold substrate, and this could verify from figure 3.14. Figure 3.14 shows the temperature variation of the central point on the hydrophilic surfaces under different temperature. The central point temperature decreasing speed of the 5˚C case was obviously slower than the other icing temperature cases. For the -1.5˚C case, the central point temperature decreased to -1.5˚C at about 0.75s, then increased back to 0˚C at about 1.95s, and kept 0˚C for a long time till about 7.2s, and finally decreased to

-1.5˚C at about 7.3s. For the case of -5˚C, its icing process is similar to the -1˚C case, while the phase change of icing and the unsteady heat transfer process was much faster. The results show that with the decreasing of icing surface temperature, there was no big difference for the biggest spreading diameter of the impingement droplet, while the final receding diameter would increase, moreover, for the icing situations, the water temperature decreasing speed would increase while the phase change of icing process would be faster too.

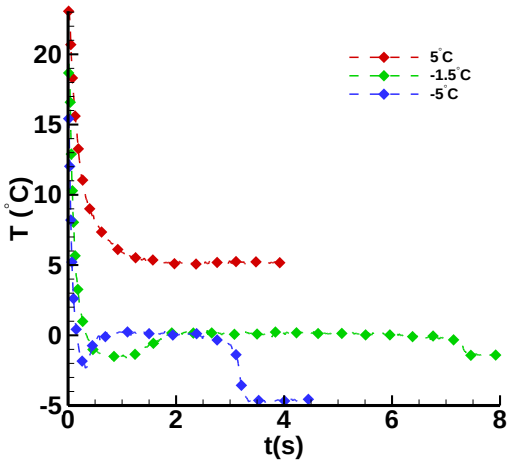

Figure 3.14 The temperature variation of the impact droplet surface central point on the hydrophilic surfaces under different temperature

3.3.5 Influence of impingement velocity on heat transfer during droplet impingement process

In this part, the temperature variation of the impingement droplet surface central point on the hydrophilic surface under different temperature and different impingement velocity would be discussed. As shown in table 3.6, the temperature of the hydrophilic surface was set as 5˚C, and -5˚C, while there were two different impingement velocity set as 3.7m/s and 2.3m/s for each temperature. The environment temperature (in the experimental cell)

and droplet before impinging was 23.5˚C, and the droplet diameter was 1.64mm with an impingement velocity of 3.7m/s. For the 3.7m/s cases, the Reynolds number and Weber number were 6109 and 319, respectively, while the Reynolds number and Weber number for the 2.3m/s cases were 3708 and 117, respectively.

Table 3.6 The final receding diameter/area/height of the impingement droplet on hydrophilic surfaces under different temperature and different droplet impingement velocity

Temperature (˚C)	Velocity (m/s)	Ds (mm)	D_r (mm)	A_f (mm^2)	Height(mm)
5	3.7	6.21	3.96	12.3	0.44
5	2.3	4.87	3.97	12.38	0.43
-5	3.7	6.19	5.97	27.99	0.30
-5	2.3	4.92	4.91	19.01	0.32

Table 3.6 shows the biggest spreading diameter, the final receding diameter, the contact area of between the impingement droplet and the substrate, and the height after the morphologic change process for the four cases. For the two cases of 5˚C, although the biggest spreading diameter had relatively big difference, the final receding diameter were nearly equal to each other, which means that the contact area between the impingement droplet and the substrate were nearly the same during the most time of the heat transfer process for these two cases had different impingement velocity. The temperature variation process of the central point shown in figure 3.15 also verified the result. For the 5˚C cases, the temperature decreasing speed of the 2.3m/s case was relatively slower than that of the 3.7m/s before the time of about 1s, while the total time for cooling the impingement droplet

to 5˚C was nearly the same. For the two cases of -5˚C, both of the biggest spreading diameter and the final receding diameter between them had big difference. The biggest spreading diameter and the final receding diameter of the 3.7m/s case was 6.19mm and 5.97mm, respectively, while that of the 2.3m/s case was 4.92mm and 4.91mm, respectively. As shown in figure 14, the temperature decreasing speed of the 2.3m/s case was slower than that of the 3.7m/s case before decreasing to 0˚C, moreover, the icing process of the 2.3m/s case was slower than that of the 3.7m/s case, which led to a longer total time for the cooling of the impingement droplet. Another big difference between them was that the 2.3m/s case didn't have a big temperature fluctuation (decreased to a negative temperature and increased back to 0˚C) during the cooling process while the 3.7m/s case did. The reason was that for the 2.3m/s case, the second receding process was faster than that of the 3.7m/s case, which made the receding water cover the central point before the central point icing. The results show that smaller droplet impingement velocity would lead to a slower cooling process and a slower icing process. Moreover, the temperature fluctuation at the surface center of the impingement droplet during the cooling process would decrease for a shorter water receding time.

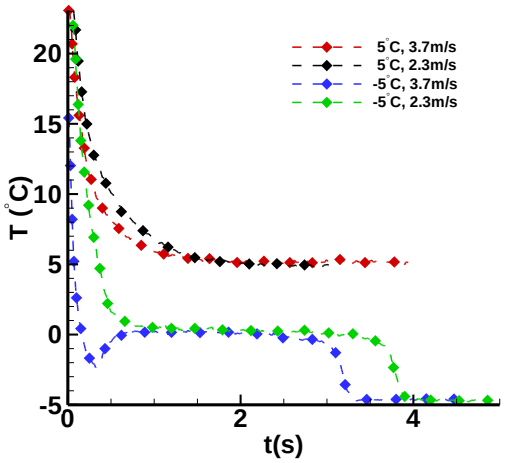

Figure 3.15 The temperature variation of the central point on the hydrophilic surfaces under different temperature and different droplet impact velocity

3.4 Conclusions

Droplets with different impact velocities impacted on the hydrophilic and superhydrophobic substrates under normal and icing temperature was investigated experimentally by using high-speed image and infrared image techniques. The morphologic change of the impact droplet, the phase change of icing, and the heat transfer during the impact process were analyzed based on the experimental results.

When droplet impact on superhydrophobic surface, the time needed for the droplet to be static is much shorter than that on hydrophilic surface, while the time needed for cooling the droplet is much longer than those on hydrophilic surface. When droplet impact on the icing temperature surfaces, the droplets upper surface temperature would decrease gradually, while obvious temperature fluctuation was observed on the droplets impacting on the hydrophilic surfaces.

Compare with that on the superhydrophobic surface, the substrate temperature can severely influence the droplet impact and icing process on the hydrophilic surface. When droplet impact on superhydrophobic surface, the bottom of the droplet would recede to a smaller diameter before icing, while it wouldn't on hydrophilic surface. With a bigger heat transfer area, the cooling speed on hydrophilic surface was much faster.

Compare with that on superhydrophobic surface, droplet impact velocity can severely influence the droplet impacted on the hydrophilic surface. With the increasing of the impact velocity, the bottom area of the droplet would increase, thus, the cooling speed would increase as well.

References

[1] Report, A. A., "National Transportation Safety in-Flight Icing Encounter and Loss of Control," vol. 1, 1994.

[2] Cober, S. G., Isaac, G. A., and Ratvasky, T. P., "Assessment of aircraft icing conditions observed during AIRS," *AIAA 40th Aerospace Sciences Meeting & Exhibit, Reno, NE*, 2002.

[3] Cao, L., Jones, A. K., Sikka, V. K., Wu, J., and Gao, D., "Anti-Icing superhydrophobic coatings," *Langmuir*, vol. 25, 2009, pp. 12444–12448.

[4] Maitra, T., Tiwari, M. K., Antonini, C., Schoch, P., Jung, S., Eberle, P., and Poulikakos, D., "On the nanoengineering of superhydrophobic and impalement resistant surface textures below the freezing temperature (Supporting Material)," *Nano Letters*, vol. 14, 2014, pp. 172–182.

[5] Vorobyev, A. Y., and Guo, C., "Multifunctional surfaces produced by femtosecond laser pulses," *Journal of Applied Physics*, vol. 117, 2015, p. 033103.

[6] Antonini, C., Villa, F., and Marengo, M., "Oblique impacts of water drops onto hydrophobic and superhydrophobic surfaces: outcomes, timing, and rebound maps," *Experiments in Fluids*, vol. 55, 2014, p. 1713.

[7] Bartolo, D., Bouamrirene, F., Verneuil, É., Buguin, A., Silberzan, P., and Moulinet, S., "Bouncing or sticky droplets: Impalement transitions on superhydrophobic micropatterned surfaces," *Europhysics Letters (EPL)*, vol. 74, 2006, pp. 299–305.

[8] Blossey, R., "Self-cleaning surfaces--virtual realities.," *Nature materials*, vol. 2, 2003, pp. 301–306.

[9] Dorrer, C., and Rühe, J., "Some thoughts on superhydrophobic wetting," *Soft Matter*, vol. 5, 2009, p. 51.

[10] Miwa, M., Nakajima, A., Fujishima, A., Hashimoto, K., and Watanabe, T., "Effects of the surface roughness on sliding angles of water droplets on superhydrophobic surfaces," *Langmuir*, vol. 16, 2000, pp. 5754–5760.

[11] Ruff, G. A., and Berkowitz, B. M., "Users manual for the improved NASA Lewis ice accretion code LEWICE 1.6," 1995.

[12] Wright, B., *Version for the NASA Code LEWICE Ice Accretion*, 2002.

[13] Potapczuk, M. G., John, N., and Field, L., "Ice Mass Measurement: Implications For The Ice Accretion Process," *AIAA 41th Aerospace Sciences Meeting & Exhibit, Reno, NE*, 2003.

[14] Waldman, R., and Hu, H., "High-Speed Imaging to Quantify the Transient Ice Accretion Process on a NACA 0012 Airfoil," *53rd AIAA Aerospace Sciences Meeting*, 2015, pp. 1–9.

[15] Liu, Y., Waldman, R., and Hu, H., "An Experimental Investigation on the Unsteady Heat Transfer Process Over an Ice Accreting NACA 0012 Airfoil," *53rd AIAA Aerospace Sciences Meeting*, 2015, pp. 1–16.

[16] Zhang, K., Wei, T., and Hu, H., "An experimental investigation on the surface water transport process over an airfoil by using a digital image projection technique," *Experiments in Fluids*, vol. 56, 2015, p. 173.

[17] Wright, W., and Potapczuk, M., "Semi-Empirical Modelling of SLD Physics," *42nd AIAA Aerospace Sciences Meeting and Exhibit*, 2004.

[18] Tan, S. C., "a Tentative Mass Loss Model for Simulating Water Droplet Splash," 2004, pp. 1–12.

[19] Boinovich, L., Emelyanenko, A. M., Korolev, V. V., and Pashinin, A. S., "Effect of wettability on sessile drop freezing: When superhydrophobicity stimulates an extreme freezing delay," *Langmuir*, vol. 30, 2014, pp. 1659–1668.

[20] Xingcheng, X., Yang Tse, C., Sheldon, B. W., and Rankin, J., "Condensed water on superhydrophobic carbon films," *Journal of Materials Research*, vol. 23, 2008, pp. 2174–21782178.

[21] Waldman, R. M., Li, H., Guo, H., Li, L., and Hu, H., "An Experimental Investigation on the Effects of Surface Wettability on Water Runback and Ice Accretion over an Airfoil Surface," 2016, pp. 1–16.

[22] bartolo D, Josserand D, B. D., "Retraction dynamics of aqueous drops upon impact on non-wetting surfaces," vol. 545, 2005, pp. 329–338.

CHAPTER 4
QUANTIFICATION OF DYNAMIC WATER DROPLET IMPACT ONTO A HYDROPHILIC SOLID SURFACE BY USING A DIGITAL IMAGE PROJECTION TECHNIQUE

4.1 Introduction

Aircraft icing is widely recognized as a significant hazard to aircraft operations in cold weather. When an aircraft or rotorcraft flies in a cold climate, some of the supercooled droplets impact and freeze on the exposed aircraft surfaces to form ice shapes. Ice may accumulate on every exposed frontal surface of an airplane, not only on the wing, propeller and windshield, but also on the antennas, vents, intakes, and cowlings. Icing accumulation can degrade the aerodynamic performance of an airplane significantly by decreasing lift while increasing drag. In moderate to severe conditions, the ice accretions may become so severe that continued flight is impossible. The airplane may stall at much slower speeds and lower angles of attack than normal. It could roll or pitch uncontrollably, and recovery may be impossible. Ice can also cause engine stoppage by either icing up the carburetor or, in the case of a fuel-injected engine, blocking the engine's air source. The importance of proper ice control for aircraft operation in cold climate was highlighted by many aircraft crashes in recent years like the ATR-72 aircraft of American Eagle flight that crashed in Roselawn, Indiana, due to ice buildup on its wings, killing all 66 people aboard on October 31, 1994. After investigation, it was found that the aircraft encountered a supercooled large droplets (SLD) icing environment, which was not defined in Appendix C of Part 25 of Federal Aviation Regulations (FAR25 Appendix C), and the aircraft crashed from

abnormal icing on airfoils[1] (Ice Protection Harmonization Working Group-IPHWG, 2005). A number of previous studies showed that the ice accretion over airfoil surfaces under different icing conditions are significantly different, especially with different impact velocity and icing temperature[2,3,4]. Further research about droplet impact is highly desirable in order to uncover the underlying physics pertinent to aircraft icing phenomena.

Droplet impact, such as the fingering of an inkblot or a coffee stain, is familiar to everyone. Droplet impact, which has been studied extensively since 1876[5], has a very wide range of applications, including atomization processes[6], raindrop dynamics[7], inkjet printing[8], blood pattern and drop trajectories[9], and micro-fabrication[10]. While it also involves most of the key issues of surface flows, droplet impact is characteristic of multiphase flows[11]. In the previous studies, a typical droplet impact process usually includes an early contact stage that considers the central bubble[12] and skating on air[13], a spreading or splash stage[14,15], and a receding or rebounding stage[16,17]. While most of the previous studies were concentrated on the air layer radius or thickness[12,13], maximum spreading radius[16,17,18], minimal thickness of the water layer[19], and whether the impacting droplet would splash[15,20] or rebounding[16,17], very few studies considered the droplet shape evolution during the impact process. Since the droplet shape evolution during the impact process can directly influence the final shape of the impact droplet under icing conditions[21], e.g. droplet impact and icing on the airfoil, and then influence the impact surface for the subsequent droplet, the accurate measurement of the droplet shape or the film thickness of the impact droplet could help reveal the underlying physics and improve the theoretical physics models used in the airfoil icing.

The most frequently-used method to measure the droplet shape is using high speed camera to record the impact process from the side view[22,23]. When a droplet normally impacts on a flat surface, it is acceptant to assume that the impact droplet is axially symmetric, and a 2-D profile can represent the real shape of the droplet. However, if the impact direction was not perpendicular to the impact surface, or the surface was not flat enough, then the real droplet shape during the impact process would be much more complicated, and a 2-D profile cannot represent of the real shape[22]. Moreover, in some moments during the droplet impact process, especially during the droplet spreading stage, the central region of the droplet is lower than the outer region[24], and thus the central region information is blocked by the outer region, which leads to the failure of obtaining droplet shape information by side view. A method which can record real 3-D shape information of impact droplet is needed. At present, there are several techniques can collect the thickness information of objects, e.g., using multi-transducer ultrasonic pulse-echo technique was used to measure the film flow thickness[25], and using space-time-resolved Fourier transform profilometry technique (FTP) to measure the 3-D shape of objective[26,27]. The ultrasonic pulse-echo technique can just do point thickness measurement, while the FTP technique need several different successive fringe patterns to achieve high accuracy measurement, which leads to the limitation of the time resolution. Since the droplet impact process, especially the spreading stage is quite fast and needs high time resolution 3-D shape information to analyze the dynamics during the impact process, a method which can achieve both thickness measurement of the full droplet and high time resolution is needed.

In the present study, an experimental investigation was conducted to quantify the shape evolution of the droplet during the impact process on a solid surface in order to elucidate underlying physics to improve our understanding of the important microphysical processes pertinent to aircraft icing phenomena. A digital image projection (DIP) technique[28] was used to achieve time-resolved measurements of the droplet thickness during the entire droplet impact process, including the spreading, receding and oscillating stages. Since the DIP technique just need one single pattern to obtain the thickness information of the full droplet, a high time resolution of the droplet thickness measurement is achieved. By comparing the droplet shape evolution under different impact velocities, the dynamics of droplet impact under different Weber numbers or Reynolds numbers was analyzed in detail. A better understanding of the droplet impact process would be helpful to improve the icing accretion model for more accurate prediction of ice formation and accretion over aircraft wings and to develop effective and robust anti-/de-icing strategies to ensure safer and more efficient operation of aircraft in cold weather.

4.2 Water Film / Droplet Thickness Measurements Using DIP Technique

During the experiment, a reference fringe pattern of the clean surface and the distorted patterns of the droplet shape were recorded with a high-speed imaging system. The droplet thickness information was extracted from the pattern-images using the image processing described here.

Figure 4.1 shows the process of extracting droplet shape data from the recorded images. Figure 4.1(a) shows the reference image that was recorded before the droplet impact. Figure 4.1(b) shows the image during the droplet impact onto the surface and illustrates how the projected light lines appear distorted in the camera view. The lines in the reference and deformed images were digitized, yielding the position information as shown in figures 4.1(c) and (d).

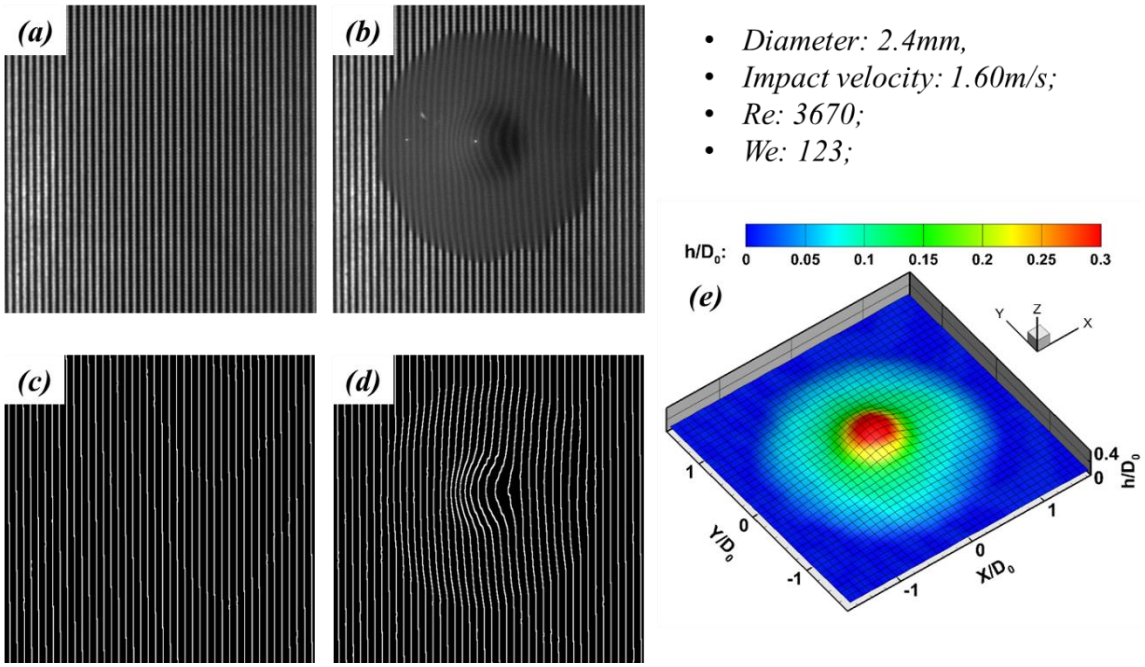

Figure 4.1 Droplet thickness extracted from the recorded images by using the DIP technique.

(a) Acquired reference raw image; (b) Acquired raw image after water droplet impact onto the surface; (c) Projected lines positions of the reference image; (d) Projected lines positions after droplet impacts; (e) Reconstructed droplet shape or film thickness over the test plate.

By comparing the position of the digitized lines in figure 4.1(c) and (d), the image displacement of the projected pattern in the droplet region was obtained. Based on the DIP

calibration (figure 4.2), the droplet shape during the impact process was reconstructed from the displacements of the projected lines relative to the reference image. Figure 4.2 shows that the displacement-to-thickness factor is

$$K = 0.0196 mm / pixel \tag{4.1}$$

Figure 4.1(e) shows the thickness data extracted from the image pair.

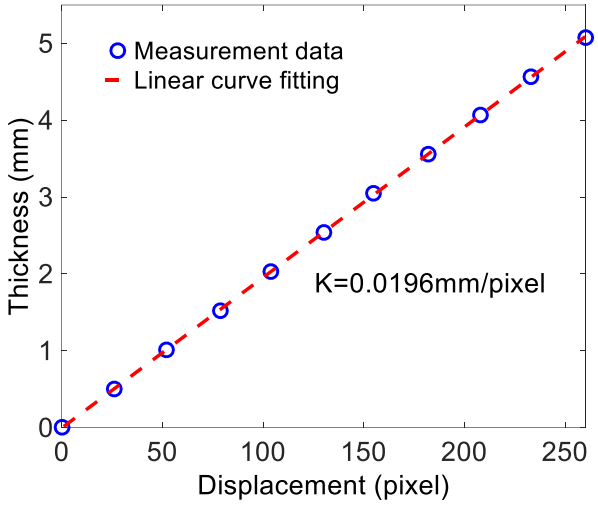

Figure 4.2 The displacement-to-thickness factor obtained through a DIP calibration procedure

4.3 Experimental setup

Figure 4.3 shows the schematic of the experimental setup used in present study to implement the DIP technique to quantify the shape evolution of the droplet during the impact process. The experimental setup was comprised of a droplet generator, an environmental chamber containing the solid substrate, a projector and lens system, a high-speed camera, and a host computer controlling both the projector and high-speed camera.

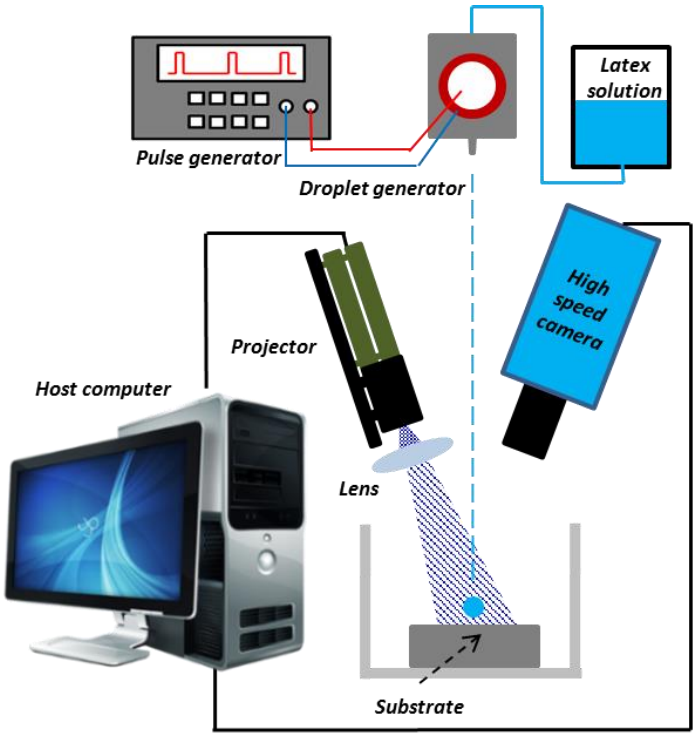

Figure 4.3 Experimental setup for the measurement of droplet 3D shape during the impact process

A volume-type droplet generator system was used to generate single water droplets. The system includes three parts: a piezo-actuated cavity, a pulse generator (Rigol 1074Z-S), and a water reservoir bottle. The main part of the droplet generator system includes a water cavity, a piezoelectric plate, and a droplet nozzle. The water cavity and droplet nozzle were rapid prototyped. Upon receiving a pulse signal from the pulse generator, the piezoelectric plate would warp and squeeze the water cavity, which would extrude a droplet from the nozzle. With suitable pulse voltage and duration, the droplet generator could eject a single droplet from each pulse. The droplet size was controlled by the nozzle inner diameter and the pulse voltage, and the droplet impingement velocity was controlled by the initial ejection velocity and the height between the droplet generator and the solid substrate. The size variation of the generated droplets when using the same pulse shape

and the same nozzle was less than 0.05mm. The droplet size can be controlled from about 1.5mm to 3.0mm by using different inner diameter nozzles and different pulse voltages.

A DLP projector (Young Optics Light Crafter) was used to project the fringe pattern on the test plate for the DIP measurement. The distance between each two adjacent lines was set to be about 0.15 mm to satisfy the measurement resolution requirement (in our study, the droplet initial diameter is about 2.4mm, and the maximum spreading diameter of the droplet was more or around 5mm). A high-speed camera (PCOtech Dimax S4) was used for recording the light pattern images. The frame rate of the high-speed camera was set to 5,000fps and the exposure time was set to $100\mu s$ to adequately time-resolve the dynamic process and minimize motion blur. The recorded images had a spatial resolution between $624\ pixels \times 620\ pixels$ to $912\ pixels \times 900\ pixels$, and a physical measurement window size between $9.2mm \times 9.1mm$ to $13.4mm \times 13.2mm$. The window sizes were selected depending on the expected spreading diameter for a particular trial.

To enhance the light diffusion on the droplet surface, a low concentration (5% by volume) of latex flat wall & trim paint (ColorPlace, Interior Flat, Light Base, 5040C) was added to water. The impact substrate was mounted in a relatively closed experimental chamber to minimize the environmental disturbances. The main part of the substrate is an aluminum plate ($2inch \times 2inch \times 1/4inch$). The plate surface was coated with white paint (Rustoleum enamel), and was wet-sanded with 2000 grit sandpaper. The advancing and receding contact angles on the surface were measured as more than 50 degrees and less than 20 degrees respectively.

Three different impact velocities (0.76m/s, 1.58m/s, and 2.08m/s) were tested. The impact velocity was set by adjusting the droplet release height.

4.4 Results and Discussions

In present study, all of the experimental data was recorded at room temperature, T = 21°C. The droplet diameter was kept at around 2.4mm, while the impact velocity was varied from about 0.7m/s to 2.1 m/s; Since the droplet was 5% (by volume) latex solution, the surface tension of the solution was measured as $55\mathrm{mN/m}$, and the viscosity is $1.05\mathrm{N\cdot s/m^2}$, while the density is $1.01\mathrm{g/\mu L}$. Therefore, the Reynolds number varied from about 1700 to 4900 and the Weber number varied from about 25 to 200, respectively. The Reynolds number and Weber number are defined as:

$$\mathrm{Re} = \frac{\rho U_0 D_0}{\mu} \tag{4.2}$$

$$\mathrm{We} = \frac{\rho U_0^{\,2} D_0}{\gamma} \tag{4.3}$$

Where Re is the Reynolds number, ρ is the droplet density, $U_0$is the droplet impact velocity, $\mathrm{D_0}$ is the droplet diameter, μ is the droplet dynamic viscosity, We is the Weber number, and γ is the droplet surface tension.

4.4.1 Three stages of the droplet impact process

Using the DIP technique, the time-resolved thickness of the droplet throughout the impact process was measured in detail. Based on the time-resolved droplet shape results, three distinct dynamical stages during the impact process were identified: the spreading stage, the retracting stage, and the oscillating stage. It is needed to note that these three

stages are different from those in previous studies. The early contact stage in the previous studies wouldn't be studied in present study, while the receding or rebounding stage in the previous studies was divided into two stages – receding and oscillating stages in this study. To explain the three distinct dynamical stages, the droplet impact process under a single impact condition is discussed in detail. Here, the droplet initial diameter is $D_0 = 2.41mm$ and the impact velocity is $U_0 = 1.58m/s$. The corresponding Reynolds and Weber numbers are $Re = 3674$ and $We = 111$, respectively.

a. Spreading stage

As the first stage of the droplet impact process, the spreading stage begins when the droplet contacts the solid surface, and it ends when the up surface center of the droplet decreases to the minimal thickness, as shown in figure 4.4(b). Figure 4.4(a) shows the time evolution of droplet ($D_0 = 2.41mm$, $U_0 = 1.58m/s$, $Re = 3674$, $We = 111$) 3D shape during this stage, thus the film thickness at all parts of the droplet have been measured precisely. In this study, all the droplets impact perpendicularly to the solid surface, therefore, we assumed that the droplets are axially symmetric. Figure 4.4(c) shows the circumferentially-averaged thickness of the droplet versus the radial position. While the average thickness is defined as:

$$\bar{h}(t) = 1/(2\pi)\int_0^{2\pi} h(r,\theta,t)d\theta \tag{4.4}$$

Where r and θ are the usual cylindrical coordinates, t is the time after the onset of the droplet impact.

After the initial contact with the solid surface, the droplet continues to flatten and expand, and the edge advances until reaching the maximum spreading diameter, and then

the outside part of the droplet except the contact line of liquid, air and solid exhibits a slight retraction from the maximum spreading location, while the contact line would stay at the maximum location with no retraction in the remaining impact process because of the hydrophilic property (the receding contact angle is less than 20 degree) of the solid surface. Then the center of the droplet reaches the minimum thickness at the center, which defines the end of the first stage. As shown in figure 4.4(a) and (c), at the time t=2.8ms, the edge of the droplet reached the maximum spreading diameter, while the center of the droplet reached the minimum thickness after another 1ms.

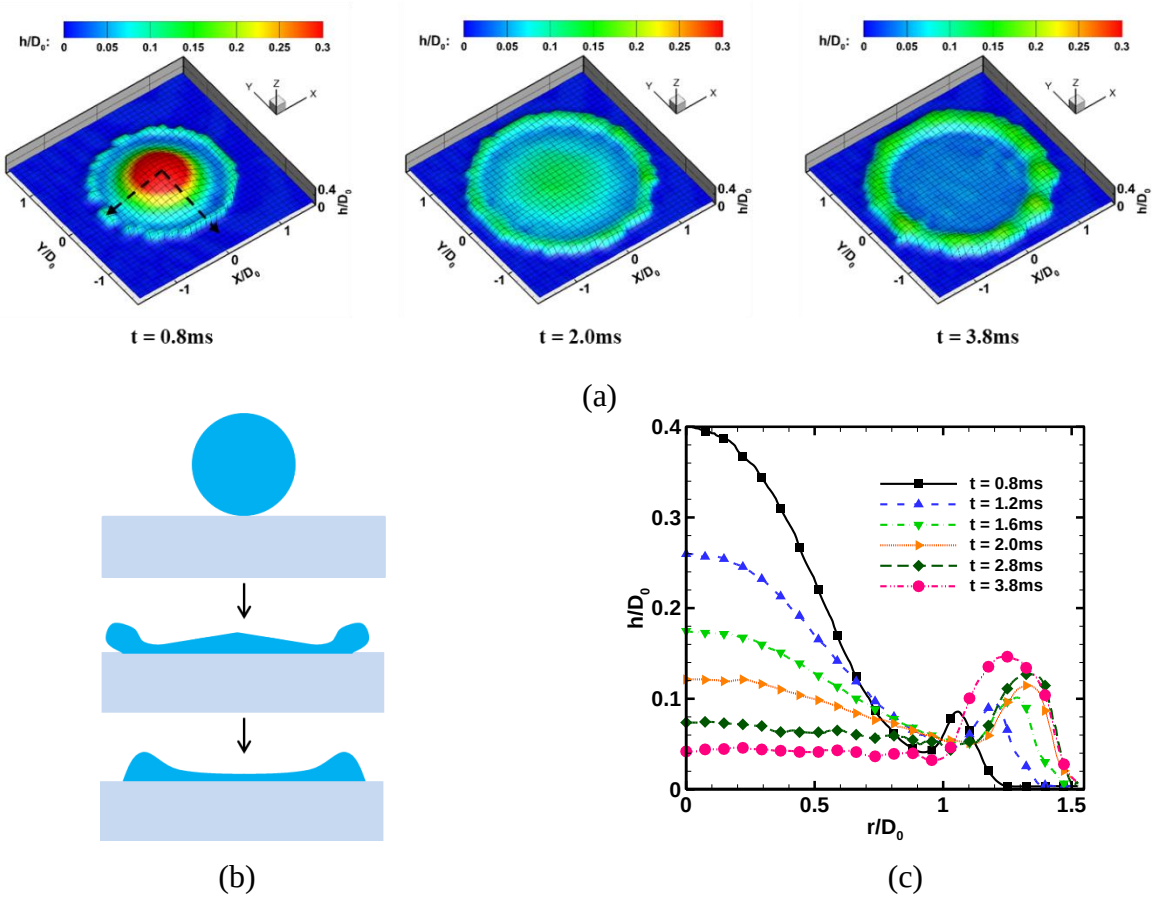

Figure 4.4 Spreading stage of the droplet impact process

(a) The time evolution of droplet shape during spreading stage; (b) Diagram of droplet spreading stage; (c) The mean thickness profile of the droplet during spreading stage.

Usually, the spreading stage includes three regimes, the pressure impact regime, the self-similar inertial regime, and the plateau regime, which have been described theoretically, numerically and experimentally[19,29,30]. Figure 6 shows the time evolution of the droplet ($D_0 = 2.46mm$, $U_0 = 1.58m/s$, $Re = 3674$, $We = 111$) central point thickness. In the early time regime, which refers to the pressure impact regime, the droplet apex continues falling at the impact velocity U_0corresponding to the freefall of the top of the droplet, and is in good agreement with the linear decrease observed in figure 4.5. As discussed in the previous studies 1-3, the following regime after the pressure regime is a called self-similar inertial regime, and the central point thickness could be predicted by

$$h_c(t) = A\frac{D_0^{\,3}}{U_0^{\,2}t^2} \tag{4.5}$$

Where A is a constant, and was given as $A = 0.492 \pm 0.030$. The red curve in figure 4.5 is the best fit of the $h_c(t) = AD_0^{\,3}/(U_0^{\,2}t^2)$ during the self-similar inertial regime, while A was set as 0.2, which is much smaller than 0.492 given in the previous study[19]. The good agreement with the measured results evaluates the validity of the theoretical law while the constant A needed to be further revised.

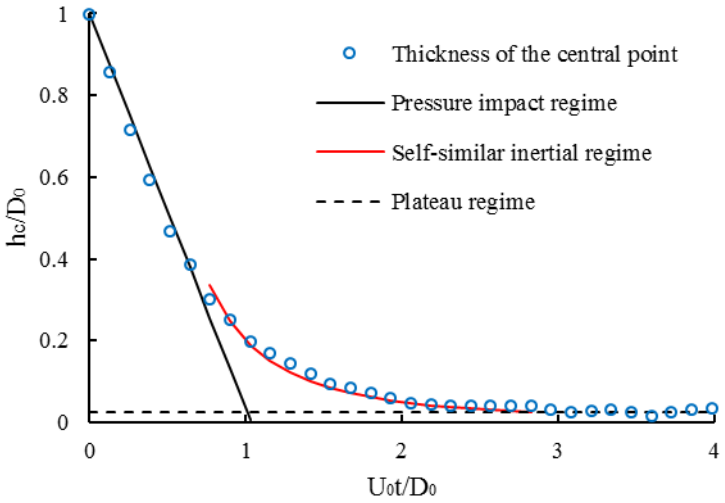

Figure 4.5 Time evolution of the droplet central point thickness during the spreading stage

The solid black line indicates the freefall or pressure impact regime. The red curve is the best fit of $h_c(t) = AD_0{}^3/(U_0{}^2t^2)$ during the self-similar inertial regime. The black dash line corresponds to the plateau minimal thickness.

At the end of the self-similar inertial regime, the thickness of the central point would decrease to a minimal value, which indicates the beginning of the plateau regime. During the plateau regime, the central point thickness would keep at the minimal value until the liquid retracting from the edge of the droplet, and the black dash line corresponds to the minimal value. This minimal thickness can directly influence the precision of the 3-D printing or spray coating, and a precise prediction of the minimal thickness is needed. By assuming that liquid motion in the droplet can be represented by axisymmetric stagnation point flow[31], the minimal thickness is given by

$$h_p \sim \mathrm{Re}^{-1/2} D_0 \tag{4.6}$$

While a simplified model of the impact dynamics deduced from the numerical simulations[30] suggests that

$$h_p \sim \mathrm{Re}^{-2/5} D_0 \tag{4.7}$$

As shown in figure 4.4(a) at the time t=3.8ms, the central point of the droplet already decreased to the minimal value, and the droplet central part was relatively flat. Thus, in present study, the minimal thickness of the central point during the plateau regime was defined as the average thickness of the central flat part. To evaluate the minimal thickness scale shown in formula (4.6) and (4.7), we measured the minimal thickness of different impact droplets with different viscosity and surface tension. Three different water-glycerol-latex paint mixtures (95%-0%-5%, 55%-40%-5%, and 35%-60%-5% by volume, respectively) were used in the measurement, and the dynamic viscosities are 1.05mPa s, 4.66mPa s, and 15.77mPa s, respectively, while the surface tensions are 55.06mN/m, 42.55mN/m and 52.31mN/m, respectively. Thus, the Reynolds number and Weber number varied from about 130 to 4900, and 25 to 200, respectively. Figure 4.6 shows the variation of h_p with the Reynolds number. The best fit of the measured results gives that $h_p \propto Re^{-0.407}$, in good quantitative agreement with the $Re^{-2/5}$ law, which also verified by another measured results[19]. In present study, the best fit of the measured results gives that $h_p = CRe^{-0.407}$, where $C = 0.71 \pm 0.01$.

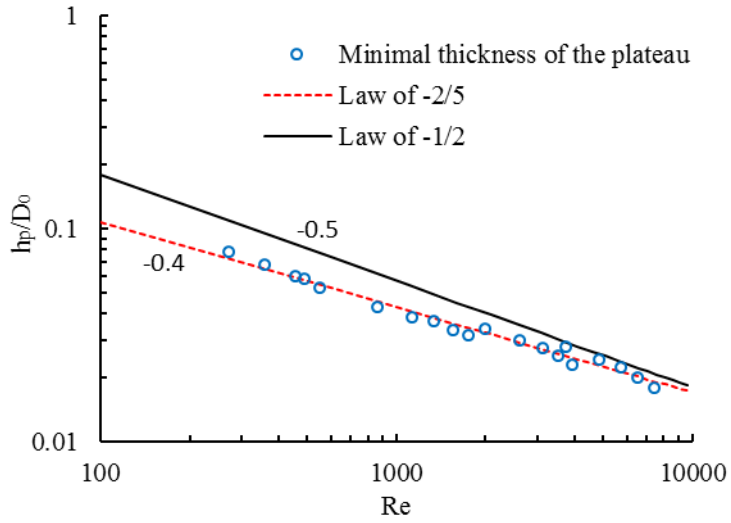

Figure 4.6 Minimal thickness of the plateau h_p as a function of the Reynolds number Re, and the two suspected laws $Re^{1/2}$ and $Re^{2/5}$ are shown as a guide.

b. Retracting stage

After the spreading stage, the droplet begins receding. During the retracting stage, the droplet center thickness would increase again due to the surface tension drawing water back toward the droplet center. The receding stage begins after the droplet center achieves the minimum thickness, and ends when the droplet center reaches the largest post-spreading-stage thickness, as shown in figure 4.7(b). Because the receding contact angle on the solid surface is less than 20 degrees the contact line between the latex paint mixture and the surface remain pinned at the maximum spreading diameter; thus, the mass available to flow during the receding stage is reduced because the contact line remains fixed.

Figure 4.7(a) shows the time evolution of droplet shape during the retracting stage. The time needed for the center thickness to increase to a secondary maximum is about 6.4ms. During this stage, the mass flow inside the droplet is radially inward. The

circumferentially-averaged thickness (figure 4.7(c)) shows this process more clearly. The reversed flow toward the droplet center can be explained by using the Young-Laplace law defined as:

$$\Delta p = \gamma \left(\frac{1}{R_1} + \frac{1}{R_2} \right) \tag{4.8}$$

Where Δp is the pressure difference at the interface between the latex solution and the air around the droplet, and when Δp is positive, the pressure in the liquid is higher than that in the air. Similarly, when Δp is negative, the pressure in the liquid is lower than that in the air. R_1 and R_2 are called the principal radii of curvature, and if the radius was in the liquid, then the radius was positive, otherwise, the radius was negative[32]. From figure 4.7(a) and (c), at the time t=7.6ms, for the central part of the droplet, both of the two principal radii of curvature are in the air, so that both R_1 and R_2 are negative; therefore, Δp is also negative, which indicates that the pressure in the liquid at the center is lower than the pressure in the air. Similarly, it shows that the pressure in the liquid at the outside edge of the droplet is higher than the pressure in the air. Since the air pressure around the droplet is equal to the room ambient pressure, the liquid pressure at the edge is higher than at the center. The fluid flows from higher pressure to lower pressure, thus the droplet center accumulates water and grows in thickness while the outside loses water mass and shrinks. The center increases to a thickness of about $0.35D_0$ (0.84mm) under this impacting condition.

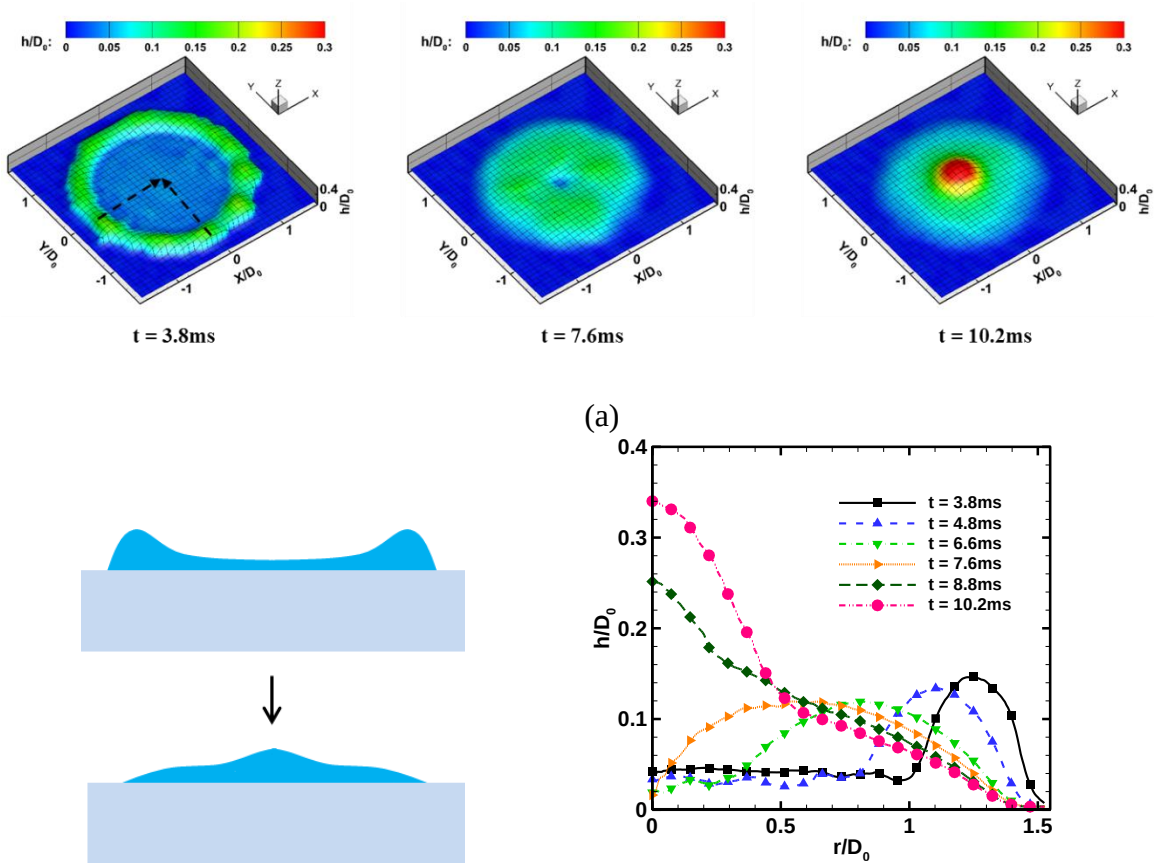

Figure 4.7 Receding stage of the droplet impact process

(a) The time evolution of droplet shape during receding stage; (b) Diagram of droplet spreading stage; (c) The mean thickness profile of the droplet during spreading stage.

c. Oscillating stage

After the receding stage, the droplet begins the oscillating stage. The oscillating stage begins when the droplet central point reaches the largest post-spreading-stage thickness, and ends when the droplet is finally at rest on the solid surface. As shown in figure 4.8(b), the oscillating stage is a process switching between spreading and receding processes. However, these spreading processes and receding processes are less pronounced than in the initial spreading and receding stages.

As shown in figure 4.8(a) at the time t=10.2ms, when the center reaches the maximum thickness at the end of the receding stage, the pressure at the center would exceed the pressure at the outside edge, so that the mass in the central part of the droplet would flow outward. This would lead to the decrease of the center thickness, and the increase of the edge thickness. At the time t=23.0ms, the droplet center decreases to a minimum thickness again. At this point, using the Laplace-Young law shown in formula (4.8), then we can predict that the cycle will repeat again. This spreading and receding process would keep repeating until the droplet is finally at rest on the surface, as shown in figure 4.8(a) at the time t=71.8ms. The circumferentially averaged thickness shown in figure 4.8(c) shows this oscillation more clearly. At the time t=10.2ms, the central part thickness (1st maximum thickness after the spreading stage) is about $0.35D_0$, at the time t=35.8ms, the central part thickness (2nd maximum thickness after the spreading stage) is about $0.16D_0$, while at the time t=23.0ms, the central part thickness (1st minimum thickness after the spreading stage) is about $0.12D_0$, and at the time t=71.8ms, the central part thickness finally gets to an equilibrium value, these thicknesses shows that the oscillating amplitude becomes less and less pronounced. This amplitude decay can be explained through energy analysis. Since the droplet has viscosity, energy is dissipated due to the internal flow inside the droplet. The energy dissipated by the viscosity could be calculated by[33]:

$$E_d = \int_0^t \int_V \phi dV dt \tag{4.9}$$

where E_d is the energy dissipated by the viscosity, V is the volume in which viscous dissipation occurs, and $\emptyset$ is the viscous function defined as[34]:

$$\phi = \frac{\mu}{2}\left(\frac{\partial U_y}{\partial x} + \frac{\partial U_x}{\partial y}\right)^2 \tag{4.10}$$

During the droplet impact process, internal fluid flow continuously dissipates the kinetic energy until the droplet rests motionless on the solid surface.

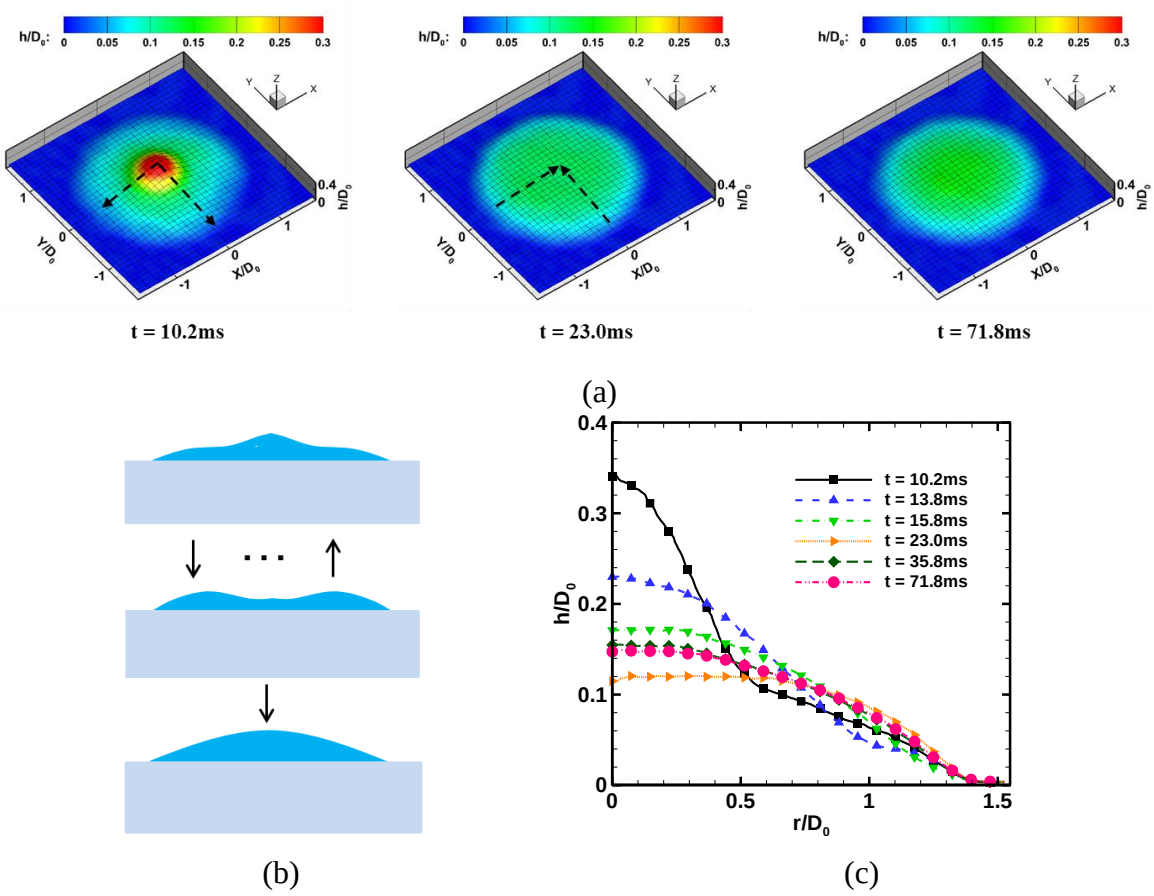

Figure 4.8 Oscillating stage of the droplet impact process

(a) The time evolution of droplet shape during oscillating stage; (b) Diagram of droplet spreading stage; (c) The mean thickness profile of the droplet during spreading stage.

4.4.2 The dynamic processes of droplet impact under different Weber and Reynolds number

To investigate the droplet impact dynamics under different impact velocities (i.e., different Reynolds numbers and Weber numbers), the droplet impact process analyzed in last section will be repeated with two other cases at different impact conditions. Table 1 shows the basic impact conditions of the three cases. The initial droplet diameter before impacting the solid surface is the around 2.4mm, while the impact velocities are different. The Reynolds number and Weber number for these three cases are summarized in Table 4.1.

Table 4.1 The initial diameter before droplet impact on the solid surface, the impact velocity, and corresponding Reynolds and Weber number under three different conditions

	D_0 (mm)	U_0 (m/s)	Re	We
Case 1	2.38	0.76	1741	25
Case 2	2.41	1.58	3674	111
Case 3	2.42	2.08	4851	192

Figure 4.9 shows the average thickness along radius at three distinct moments during the droplet impact process. Figure 4.9(a) shows the moment at the end of the spreading stage, figure 4.9(b) shows the moment at the end of the receding stage, and figure 4.9(c) shows the moment at the end of the oscillating stage. Based on the time resolved thickness profiles along radius, the impact velocity or the Weber and Reynolds numbers' influence to the dynamics of the impact droplet could be discussed carefully.

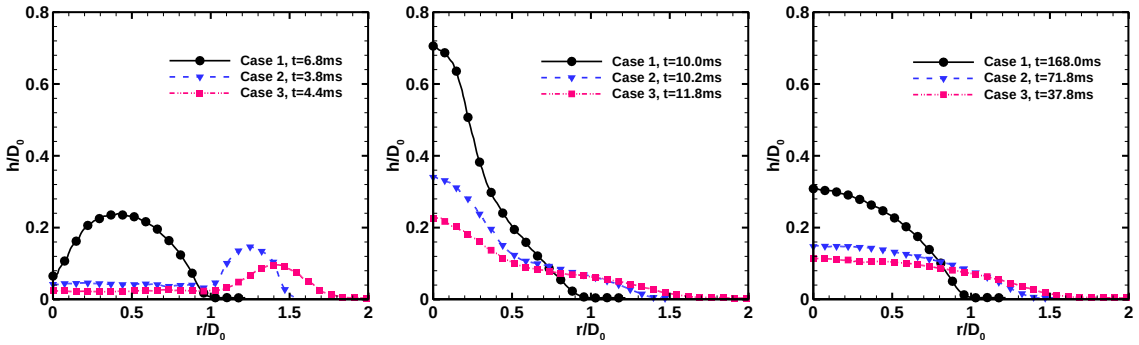

(a) (b) (c)

(a) End of spreading stage; (b) End of receding stage; (c) End of oscillating stage.

Figure 4.9 The average thickness along radius of the three distinct moments of three different impact cases

Figure 4.9(a) shows the average thickness profile at the end of the spreading stage, and as expected, the spreading process of the droplet under different Weber number proceeds similarly. During the spreading stage, the droplet center descends until it reaches a minimum thickness, while the droplet diameter expands until it reaches the maximum spreading diameter, and the mass flow direction is radially outward. However, there still are some differences in the dynamics. First, with the larger Weber number, the central decent speed is larger during the early time regime (i.e., first 2ms) due to the larger impact velocity of the droplet. Larger Weber number also accompanies a larger spreading speed. The time for the droplet to reach the minimum thickness should decrease, however, the spreading stage for these three cases are 6.8ms, 3.8ms, and 4.4ms, which does not agree with the analysis, and the explanation requires additional study. Moreover, at the end of the spreading stage the shapes of the droplet in these three cases have obvious differences, especially at the center. When the droplet center decreases to a minimum thickness, all of these three cases have similar ridge shape at the outside edge of the droplet, and the bottom width of the ridge for case 1 is from 0 D_0 to about 1 D_0, while that for case 2 is from about

0.9 D_0 to about 1.5 D_0, and that for case 3 is from about 1.1 D_0 to about 1.7 D_0. When considering the central part of the droplet, the shape has obvious differences. For case 2 and 3, when the Weber number increase to 111 and 192, the spreading droplet has obvious flat liquid plate, which is called a plateau. The plateau radius for case 2 is about 0.9 D_0, and that for case 3 is about 1 D_0, while there is no such plateau in case 1. This is because when the Weber number is small, the descent speed of the droplet center and the expanding speed is small and the droplet does not have enough energy to overcome surface tension during the spreading process. Therefore, when the droplet center decreases to the minimum thickness, the outside edge already begins receding and the center will reverse direction. However, when the Weber number increases to a certain value, the droplet has enough energy to overcome the surface tension during the spreading process, and will achieve a larger spreading diameter, so that when the droplet center reaches the minimum thickness, the receding liquid from the outside part is still far away, thus these impact droplets will have a so called plateau at the central part. Figure 4.10 shows the 3D shape instead of the average one. As shown in figure 4.10, the ridge becomes a thin ring, and from the 3D shape, we even could find that the rings in case 2 and case 3 are different. With the increase of the Weber number (i.e., from 111 to 192), the relative smooth ring becomes rough. The stability of the droplet would decrease due to the interactions among the droplet, the solid surface and the air around the droplet[20]. When the Weber number or the impact velocity increases to a certain value, the stability of the droplet would become unstable enough, which leads to the droplet splash during the spreading stage. Another phenomenon that was observed is the maximum spreading diameter. The droplet

maximum spreading diameter D_0 would increase with the increase of the Weber number, and the spreading factors $\beta = D_{max}/D_0$ agree well with the predicted values[35] defined by

$$\beta \propto We^{1/4} \tag{4.11}$$

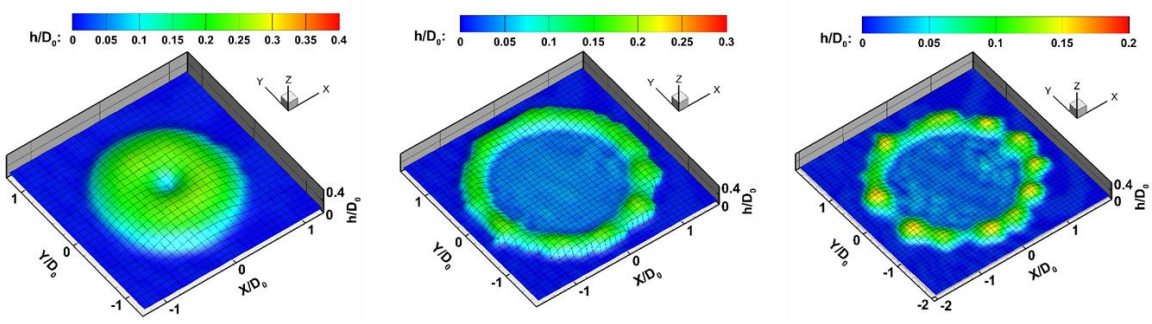

(a) Case1, t=6.8ms (b) Case 2, t=3.8ms (c) Case 3, t=4.4ms

Figure 4.10 The impact droplet shape at the end of the spreading stage under different impact conditions

Figure 4.9(b) shows the average thickness profile at the end of the receding stage. At the end of the spreading stage, when the droplet center reaches minimum thickness, the magnitude of the principal radii of curvature R_1 and R_2 at the droplet central part would increase with the Weber number, while those at the outside edge are small. Based on equation (4.8), the pressure difference between the center and edge would decrease, so that the receding phenomenon become less drastic. Thus, it shows that the maximum thickness of the droplet central part for case 1 is about $0.75D_0$, while that for case 2 is about 0.36 D_0, and that for case 3 is just about 0.24 D_0.

Figure 4.9(c) shows the average thickness profile at the end of the oscillating stage. When the droplet finally comes to rest on the solid surface, the shape of the droplet would look like a spherical cap, and with the increase of the Weber number, the cap becomes flatter and wider. For case 1, the central part thickness of the droplet is about $0.3D_0$, and

the bottom radius of the droplet is about $1D_0$, while those for case 2 are about $0.16D_0$, $1.3D_0$, for case 3 are about $0.12D_0$ and $1.5D_0$ respectively. As discussed in last section, due to the small receding contact angle, the bottom of the droplet would not retract, thus the contact line between droplet and solid surface would stay at the maximum spreading position. Therefore, when the droplet finally rests on the solid surface, the shape of the droplet would remain flatter and wider with the increase of the droplet impact velocity or the Weber number.

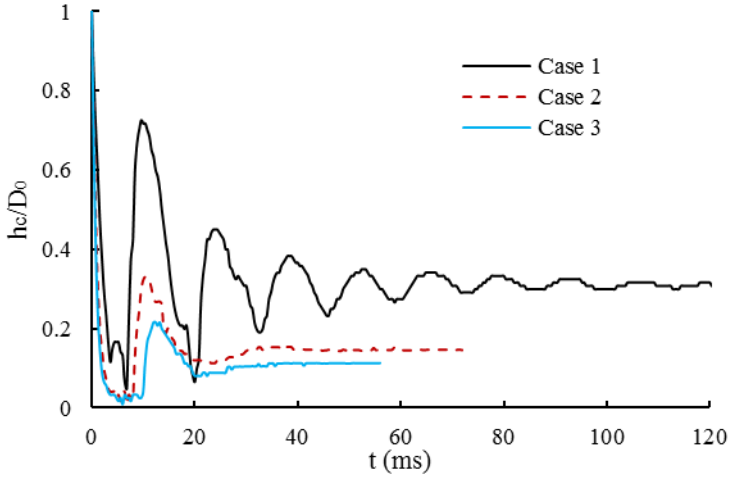

Figure 4.11 Time evolution of the droplet central point thickness under different impact conditions

Meanwhile, with the increase of the Weber number, the total time needed for the droplet finally rest on the solid surface would decrease; specifically, the total time for case 1 is about 168.0ms, while those for case 2 and 3 are 71.8ms and 37.8ms, respectively. From figure 4.9(b), the total time for the droplet spreading and receding stages are nearly same, the time for all of these three cases varies from 10ms to 12ms, so that the main difference is in the oscillating stage. Figure 4.11 shows the oscillatory spreading and receding process clearly. The peaks of the curve mean that the droplet is at the end of the

receding phases, and the valleys means that the droplet is at the end of the spreading phases. It can be seen that the spreading and receding stages looks similar in main shape variation, except for the central thickness fluctuation due to the capillary waves[36] in case 1, and the obvious plateau at the central part in case 2 and 3. However, there is significantly different dynamics in the oscillating stage. For case 1, it shows at least 7 obvious spreading and receding cycles during the oscillating stage, while for case 2 and case 3, only 1 obvious spreading and receding cycle could be seen during the oscillating stage. To uncover the physics under this kind of phenomenon, more detailed analysis is needed. At the end of the spreading stage, the kinetic energy inside the droplet is nearly 0, thus the main energy at this moment inside the droplet is surface energy[37]. Thus, the surface energy dominates the motion of the droplet during the oscillating stage, and the oscillating of the droplet could be assumed as damped harmonic oscillator defined as[38,39]

$$m\ddot{x} = -kx - c\dot{x} \tag{4.12}$$

where, x is the deflection from a neutral (the central point thickness when the droplet is finally rest on the solid surface), $\dot{x}$ and $\ddot{x}$ are, respectively, the first- and second-order time derivatives. m is the mass of the system (the droplet mass), k is a spring constant which related with the surface tension of the droplet, and c is a damping coefficient which related with the viscosity of the droplet. To solve this second-order differential equation, the required initial conditions are the initial displacement $x(0)$ and the initial velocity $\dot{x}(0)$. The general solution for equation (4.12) is

$$x(t) = e^{-(\alpha t/2)}[A\cos(\eta t) + B\sin(\eta t)] \tag{4.13a}$$

$$\alpha = c/m,\ \eta = \sqrt{\omega^2 - (\alpha/2)^2},\ A = x(0),\ B = \frac{1}{\eta}\left[\dot{x} + \frac{\eta}{2}x(0)\right] \tag{4.13b}$$

Where α is the viscous damping factor, ω is the corresponding un-damped angular frequency of the oscillator. The damping coefficient determines the decay in the amplitude, whereas both constant and the damping coefficient govern the frequency of oscillator, and the viscous damping coefficient α can be scaled and correlated as a function of Reynolds number $\alpha = f(Re)$, while the frequency of oscillation ω can be scaled by the Reynolds and We numbers $\omega = f(We, Re)$[38].

As the droplet central point reaches its post-impact maximum thickness at end of the retracting stage or at the beginning of the oscillating stage, the contact line velocity and the rate of change in thickness become zero. Thus, because the damped harmonic systems model begins at the instant of post-impact maximum thickness, for the subsequent damped oscillator motion the initial conditions are given by

$$h_c(0)/D_0 = h_{c\max}/D_0,\ \dot{h}_c(0)/D_0 = 0 \tag{4.14}$$

By referencing the time-dependent response to the equilibrium condition (the condition when the droplet is finally rest on the impact surface), the variation of the central point thickness can be obtained as

$$h_c(t)/D_0 = h_{ceq}/D_0 + \exp(-\alpha t/2)[A\cos(\eta t) + B\sin(\eta t)] \tag{4.15a}$$

Where

$$\eta = \sqrt{\omega^2 - (\alpha/2)^2},\ A = \left(h_c(0) - h_{ceq}\right)/D_0,\ B = \frac{1}{\eta}\left[\dot{h}_c(0) + \frac{\alpha}{2}\left(h_c(0) - h_{ceq}\right)\right]/D_0 \tag{4.15b}$$

The damping factor α can be related to the ratio of the amplitude between successive peaks, while the frequency ω can be related to the time difference between successive peaks.

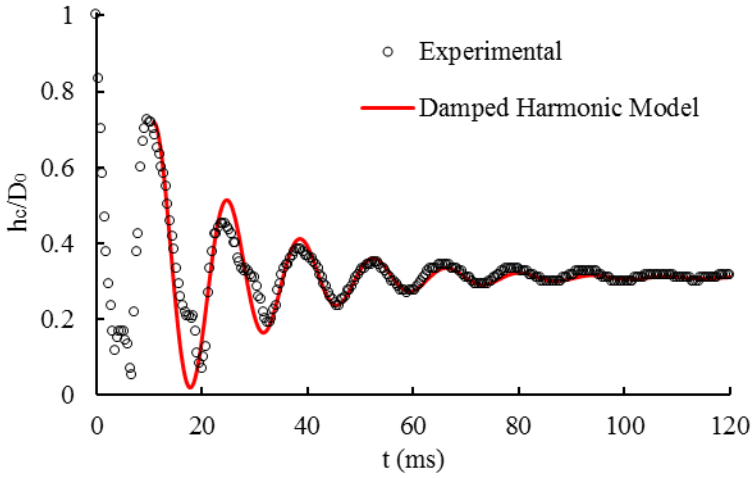

(a)

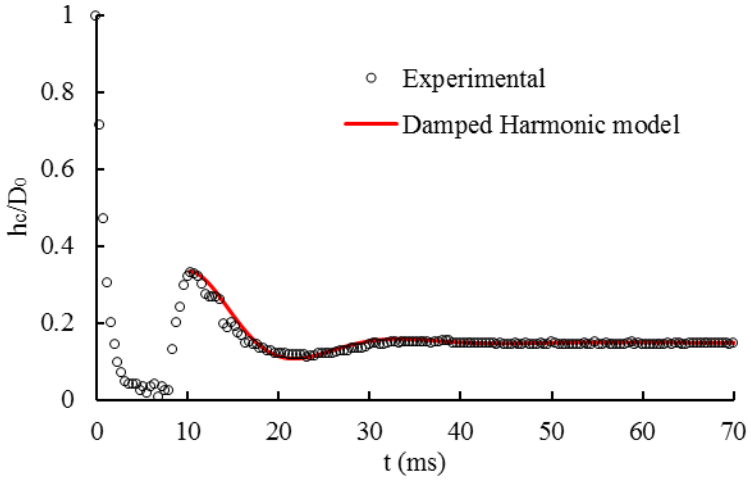

(b)

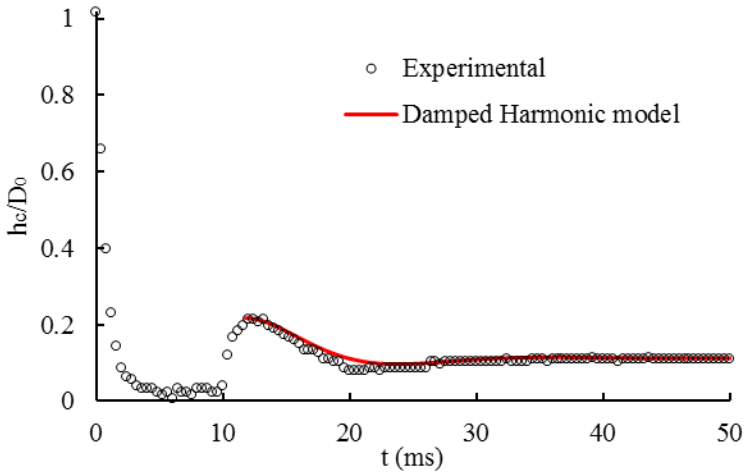

(c)

(a) case 1; (b) case 2; (c) case 3.

Figure 4.12 Comparison of experimental and the damped harmonic model results of the time evolution of the droplet central point thickness under different impact conditions during the oscillating stage.

Figure 4.12 shows the comparison of the experimental and the damped harmonic model results of the time evolution of the droplet central point thickness under different impact conditions during the oscillating stage. The good agreement of the experimental and modeled results verified that the oscillating stage of the impact droplet can be represented by a damped harmonic model. Comparing the damped harmonic oscillator under different conditions, it is found that when droplet impact on a hydrophilic solid surface, with the increase of the impact velocity, Reynolds number, the time needed for the oscillator to be finally rest become shorter, thus the damping coefficient would grow, which is contrary to that on the hydrophobic solid surface[38]. As shown in previous study, when droplet impact on a hydrophobic surface, the time needed for the oscillator to be finally rest become longer with the increase of the droplet Reynolds number. This opposite phenomenon is due to the motion of the contact line between the droplet, solid surface and

air. When droplet impact on hydrophobic surface, the contact line would retract back and spread out during the retracting stage and the oscillating stage, and a higher impact velocity or bigger Reynolds number means a bigger spreading diameter, which leads to stronger retracting and spreading process; however, when the droplet impact on a hydrophilic surface, the contact line would stay at the maximum spreading position during the retracting and oscillating stages, and the bigger spreading diameter due to the higher impact velocity or bigger Reynolds number would reduce the droplet retracting upon the bottom. The decreasing of the frequency corresponding to the increasing of the impact velocity agree well with that on hydrophobic surface.

4.4.3 Discussions on Measurement Uncertainty

Figure 4.13 shows the DIP technique measurement accuracy in droplet thickness measurement. Figure 4.13(a) shows droplet volume during the entire impacting process measured by DIP technique and the volume calculated based on initial droplet size before the droplet impact on the solid surface. The droplet initial diameter is 2.41mm, the impact velocity is 1.58m/s, and the Reynolds and Weber numbers are 3674 and 111 respectively. This shows that the DIP technique measurement results agree well with the calculated volume based on the initial droplet size, except between about 1.5–4ms. This is because the DIP technique can only measure the top surface of the droplet, while it cannot measure the air thickness under the droplet, as shown in figure 4.13(b). In the time between about 1.5–4ms, the droplet was in the spreading stage, and during this stage, the droplet spreading speed at the edge was faster than the contact line between droplet and the solid surface. Therefore, the air underneath the droplet, which is occluded from the view in the

DIP image, was erroneously considered as part of the droplet during the thickness measurement. Thus, during the spreading process, the droplet volume measured by DIP technique is a little higher than that calculated based on initial droplet size before droplet impact on the surface. After the spreading stage, the volume measured by DIP technique is continually a little smaller than that calculated based on initial droplet size, and this is due to the penetration of the light through the droplet surface. Even though the latex paint adds into the water significantly increase the light scattering on the droplet surface, the projected light still can penetrate the droplet surface due to the character of liquid. The compared results show that the maximum measurement error of the volume is less than 8%(during the spreading stage), and the relative mean error during the whole impact process is 2.63%, while the measurement uncertainty is 0.94%.

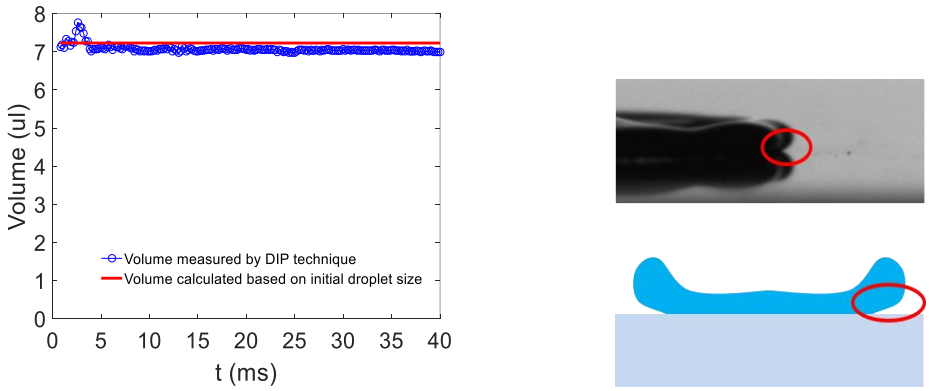

(a) Measured droplet volume (b) Droplet contact line during the spreading process.

Figure 4.13 DIP technique measurement accuracy

4.5 Conclusions

In the present study, an experimental investigation was conducted to quantify the shape evolution of the droplet during the impact process on solid surface in order to elucidate underlying physics to improve our understanding of the important microphysical

processes pertinent to aircraft icing phenomena. A digital image projection (DIP) technique was used to achieve time-resolved measurements of the droplet thickness during the entire droplet impact process, including the spreading, receding and oscillating stages. By comparing the droplet shape evolution under different impact velocities, the dynamics of droplet impact under different Weber numbers or Reynolds numbers were analyzed in detail.

By comparing the droplet volume measure by digital image projection technique during the impact process with the droplet volume calculated based on the initial diameter of the droplet before contacting on the surface, the digital image projection technique measurement error and uncertainty was validated. The compared result shows that the measurement error of the technique is less than 5%, while the measurement uncertainty is less than 2%.

Based on the time-resolved droplet film thickness, the droplet impact on a solid surface could be divided into three distinct stages: the spreading stage, which begins when the droplet first contacts the surface and ends when the droplet center reaches the minimum thickness; the retracting stage, which begins following the end of the spreading stage and ends when the droplet center achieves a secondary maximum thickness; and the oscillating stage, which begins following the end of the receding stage and ends when the droplet finally comes to rest on the solid surface. The three successive regimes, i.e., pressure impact regime, self-similar inertial regime and the plateau regime during the spreading stage investigated in previous studies was verified in present study.

By comparing the droplet shape evolution under different impact velocities, it was found that with the increase of the impact velocity, Weber and Reynolds number, the maximum spreading diameter of the droplet would increase, as would with the spreading speed. Additionally, the droplet has a plateau at the center under high Weber number conditions, while under the low Weber condition, no plateau was observed. Also, with a much longer oscillation stage compared with the higher Weber number cases, the total time for the droplet to finish the impact process under the lower Weber number condition is longer. The oscillating stage was simulated by a damped harmonic oscillator, and shows good agreement with the experimental results. It found that the oscillating stage on hydrophilic surface is different from that on hydrophobic surface, with the increase of the impact velocity, or Reynolds number, the time needed for the oscillator to be finally rest become shorter.

References

[1] Report, A. A., "National Transportation Safety in-Flight Icing Encounter and Loss of Control," vol. 1, 1994.

[2] Potapczuk, M. G., John, N., and Field, L., "Ice Mass Measurement: Implications For The Ice Accretion Process," *AIAA 41th Aerospace Sciences Meeting & Exhibit, Reno, NE*, 2003.

[3] Waldman, R., and Hu, H., "High-Speed Imaging to Quantify the Transient Ice Accretion Process on a NACA 0012 Airfoil," *53rd AIAA Aerospace Sciences Meeting*, 2015, pp. 2–5.

[4] Liu, Y., Waldman, R., and Hu, H., "An Experimental Investigation on the Unsteady Heat Transfer Process Over an Ice Accreting NACA 0012 Airfoil," *53rd AIAA Aerospace Sciences Meeting*, 2015, pp. 1–16.

[5] Worthington, "On the forms assumed by drops of liquids falling vertically on a horizontal plate," 1876, pp. 261–272.

[6] Eggers, J., and Villermaux, E., “Physics of liquid jets,” vol. 71, 2008.

[7] Planchon, O., “A Physical Model for the Action of Raindrop Erosion on Soil Microtopography,” vol. 74, 2010.

[8] Minemawari, H., Yamada, T., Matsui, H., Tsutsumi, J., Haas, S., Chiba, R., Kumai, R., and Hasegawa, T., “Inkjet printing of single-crystal films,” *Nature*, vol. 475, 2011, pp. 364–367.

[9] Attinger, D., Moore, C. B., Donaldson, A., and Stone, H. A., “Fluid dynamics topics in bloodstain pattern analysis : Comparative review and research opportunities,” 2013.

[10] Antkowiak, A., Audoly, B., and Josserand, C., “Instant fabrication and selection of folded structures using drop impact,” vol. I.

[11] Rein, M., “Phenomena of liquid drop impact on solid and liquid surfaces,” vol. 12, 1993, pp. 61–93.

[12] Engineering, M., Drive, E., and Engineering, E., “The air bubble entrapped under a drop impacting on a solid surface,” vol. 545, 2005, pp. 203–212.

[13] Street, G., and Street, G., “Air cushioning with a lubrication/inviscid balance,” vol. 482, 2003, pp. 291–318.

[14] Eggers, J., Fontelos, M. A., Josserand, C., Zaleski, S., Eggers, J., Fontelos, M. A., Josserand, C., and Zaleski, S., “Drop dynamics after impact on a solid wall : Theory and simulations Drop dynamics after impact on a solid wall : Theory and simulations,” vol. 062101, 2016.

[15] Chr. Mundo, M. Sommerfeld, C. T., “Droplet-Wall Collisions: Experimental Studies of the Deformation and Breakup Process,” vol. 21, 1995.

[16] Rioboo, R., Heat, E., and Sa, P., “Outcomes from a Drop Impact on Solid Surfaces,” 2001.

[17] Statistique, P., and Lhomond, R., “Retraction dynamics of aqueous drops upon impact on non-wetting surfaces,” vol. 545, 2005, pp. 329–338.

[18] Roisman, I. V, Berberović, E., Tropea, C., Roisman, I. V, Berberovi, E., and Tropea, C., “Inertia dominated drop collisions . I . On the universal flow in the lamella Inertia dominated drop collisions . I . On the universal flow in the lamella,” vol. 052103, 2016.

[19] Lagubeau, G., Fontelos, M. A., Josserand, C., Maurel, A., Pagneux, V., and Petitjeans, P., “Spreading dynamics of drop impacts,” 2012, pp. 50–60.

[20] Xu, L., Zhang, W. W., and Nagel, S. R., “Drop Splashing on a Dry Smooth Surface,” vol. 184505, 2005, pp. 1–4.

[21] Zhang, C., and Liu, H., “Effect of drop size on the impact thermodynamics for supercooled large droplet in aircraft icing Effect of drop size on the impact thermodynamics for supercooled large droplet in aircraft icing,” vol. 062107, 2016.

[22] Josserand, C., and Thoroddsen, S. T., “Drop Impact on a Solid Surface,” pp. 365–393.

[23] Bartolo, D., Josserand, C., and Bonn, D., “Singular Jets and Bubbles in Drop Impact,” vol. 124501, 2006, pp. 1–4.

[24] Li, H., Waldman, R. M., and Hu, H., “An Experimental Investigation on Unsteady Heat Transfer and Transient Icing Process upon Impingement of Water Droplets,” 2016, pp. 1–18.

[25] Liu, Y., Chen, W., Bond, L. J., and Hu, H., “An experimental study on the characteristics of wind-driven surface water film flows by using a multi-transducer ultrasonic pulse-echo technique An experimental study on the characteristics of wind-driven surface water film flows by using a multi-transducer ultrasonic pulse-echo technique,” vol. 012102, 2017.

[26] Hu, H., Wang, B., and Zhang, K., “Quantification of transient behavior of wind-driven surface droplet / rivulet flows using a digital fringe projection technique,” *Journal of Visualization*, 2015, pp. 705–718.

[27] Dai, J., Li, B., and Zhang, S., “High-quality fringe pattern generation using binary pattern optimization through symmetry and periodicity,” *Optics and Lasers in Engineering*, vol. 52, 2014, pp. 195–200.

[28] Zhang, K., Wei, T., and Hu, H., “An experimental investigation on the surface water transport process over an airfoil by using a digital image projection technique,” *Experiments in Fluids*, vol. 56, 2015, p. 173.

[29] Roisman, I. V, and Roisman, I. V, “Inertia dominated drop collisions . II . An analytical solution of the Navier – Stokes equations for a spreading viscous film Inertia dominated drop collisions . II . An analytical solution of the Navier – Stokes equations for a spreading viscous film,” vol. 052104, 2010.

[30] Eggers, J., Fontelos, M. A., Josserand, C., and Zaleski, S., “Drop dynamics after impact on a solid wall : Theory and simulations,” 2010, pp. 1–13.

[31] Fard, M. P., Qiao, Y. M., Chandra, S., Mostaghimi, J., Qiao, Y. M., Chandra, S., and Mostaghimi, J., "Capillary effects during droplet impact on a solid surface Capillary effects during droplet impact on a solid surface," vol. 650, 1996.

[32] Lautrup, B., *Physics of Continuous Matter*, Institute of physics Publishing Ltd, 2005.

[33] Chandra, S., and Avedisian, C. T., "On the collision of a droplet with a solid surface," *Proc. R. Soc. London, Ser. A*, vol. 432, 1991, pp. 13–41.

[34] Qian, T., Wang, X., and Sheng, P., "A variational approach to moving contact line hydrodynamics," *J. Fluid Mech.*, vol. 564, 2006, pp. 333–360.

[35] CLANET, C. S., BE´GUIN, C. D., RICHARD, D., and QU ´ ER ´E, D., "Maximal deformation of an impacting drop ´," vol. 517, 2004, pp. 199–208.

[36] RENARDY, Y., POPINET, S., DUCHEMIN, L., RENARDY, M., ZALESKI, S., JOSSERAND, C., DRUMRIGHT-CLARKE, M. A., RICHARD, D., CLANET5, C., and QUERE, D., "Pyramidal and toroidal water drops after impact on a solid surface," vol. 484, 2003, pp. 69–83.

[37] Lee, J. B., Derome, D., Dolatabadi, A., and Carmeliet, J., "Energy Budget of Liquid Drop Impact at Maximum Spreading: Numerical Simulations and Experiments," 2016.

[38] Manglik, R. M., Jog, M. A., Gande, S. K., Ravi, V., Manglik, R. M., Jog, M. A., Gande, S. K., and Ravi, V., "Damped harmonic system modeling of post-impact drop-spread dynamics on a hydrophobic surface Damped harmonic system modeling of post-impact drop-spread dynamics on a hydrophobic surface," vol. 082112, 2013.

[39] Banks, D., Ajawara, C., and Sanchez, R., "EFFECTS OF LIQUID AND SURFACE CHARACTERISTICS ON OSCILLATION BEHAVIOR OF DROPLETS UPON IMPACT," vol. 24, 2014, pp. 895–913.

CHAPTER 5
MAXIMUM DIAMETER OF IMPACTING LIQUID DROPLETS ON SOLID SURFACE

5.1 Introduction

Droplet impact, which has been studied extensively since 1876[1], has a very wide range of applications, including atomization processes[2], raindrop dynamics[3], inkjet or 3D printing[4], spray cooling of hot surfaces[5], blood pattern and drop trajectories[6], and micro-fabrication[7]. While it also involves most of the key issues of surface flows, droplet impact is characteristic of multiphase flows[8]. The subject is so important that numerous researchers have investigated the droplet impact based on numerical modeling[9–12], or experimental methods[13–17]. A typical droplet impact process can usually be divided into three stages, and early contact stage that consider the central bubble[18] and skating on air[19], a spreading or splash stage[20,21], and a receding or rebounding stage[22]. One of the most important parameters of great interests in this study is the maximum spreading diameter D_{max} which is often normalized by the initial diameter of the droplet prior to impact, resulting in a maximum spreading factor β. Since the maximum spreading diameter of the droplet can directly influence the applications of the impact droplet such as the precise of the 3D printing[4] and the micro-fabrication[7], an accurate prediction of the maximum spreading diameter is extremely needed.

To predict the maximum spreading diameter of the impact droplet, a large number of different models have been proposed for the maximum spreading factor β_{max}. For example, Scheller & Bousfield[23] proposed an empirical law based on experimental results;

Pasandideh-Fard et al.[24] developed a spreading factor model based on detailed energy balance between the initial droplet prior impact and the droplet at the maximum spreading; Ukiwe & Kwok[25] extended the above model with an approximated static contact angle and a cylinder assumption; Clanet et al.[26] came up with a spreading factor scale by considering the mass balance using the impact capillary length; Roisman[27] and Eggers et al.[9] raised the spreading factors using dynamical model for the spreading of the droplet involving a viscous boundary layer. Comparing with those spreading factor models based on mass balance or using dynamical model, the spreading factor models based on detailed energy balance give explicit values, while most of the others give scales and need more conditions and analyses to obtain the explicit values. However, those spreading factors based on the energy balance need more accurate experimental data instead of assumptions to improve the prediction accuracy. For example, Pasandideh-Fard et al.[24] assumed that the shape of the droplet at the maximum spreading was a circle, while Ukiwe & Kwok[25] assumed it as a cylinder, while the real shape of the droplet at the maximum spreading was much more complex than just a circle or cylinder, especially under low Reynolds and Weber numbers impacting conditions. The Weber number and Reynolds number are defined in equations (5.1) and (5.2). To increase the prediction accuracy, a method is needed to precisely measure the shape of the impact droplet at the maximum spreading.

$$\mathrm{Re} = \frac{\rho U_0 D_0}{\mu} \tag{5.1}$$

$$\mathrm{We} = \frac{\rho U_0^{\,2} D_0}{\gamma} \tag{5.2}$$

The most frequently-used method to measure the droplet shape is using high speed camera to record the impact process from the side view[28,29]. When a droplet normally impacts on a flat surface, it is acceptant to assume that the impact droplet is axially symmetric, and a 2-D profile can represent the real shape of the droplet. However, if the impact direction was not perpendicular to the impact surface, or the surface was not flat enough, then the real droplet shape during the impact process would be much more complicated, and a 2-D profile cannot represent of the real shape[28]. Moreover, in some moments during the droplet impact process, especially during the droplet spreading stage, the central region of the droplet is lower than the outer region[30], and thus the central region information is blocked by the outer region, which leads to the failure of obtaining droplet shape information by side view. A method which can record real 3-D shape information of impact droplet is needed. At present, there are several techniques can collect the thickness information of objects, e.g., using multi-transducer ultrasonic pulse-echo technique was used to measure the film flow thickness[31], and using space-time-resolved Fourier transform profilometry technique (FTP) to measure the 3-D shape of objective[32,33]. The ultrasonic pulse-echo technique can just do point thickness measurement, while the FTP technique need several different successive fringe patterns to achieve high accuracy measurement, which leads to the limitation of the time resolution. Since the droplet impact process, especially the spreading stage is quite fast and needs high time resolution 3-D shape information to analyze the dynamics during the impact process, a method which can achieve both thickness measurement of the full droplet and high time resolution is needed.

In the present study, a revised impact droplet maximum spreading diameter model based on detailed energy balance was proposed by precisely measure the droplet shape at the maximum spreading. A digital image projection (DIP) technique[34] was used to achieve the precise measurement of the impact droplet shape. Since the DIP technique can only measure the upper surface shape of the droplet, a side-view of the impact droplet was imported to help measure the bottom part shape of the droplet at the maximum spreading. Based on the precise droplet shape by combining the DIP technique and side-view results, a surface area factor was proposed, and by applying this factor in the droplet maximum spreading diameter model, a revised model was developed. This revised model can sufficiently reduce the prediction error caused by the shape assumption in the energy balance analysis. To validate the prediction accuracy, the predicted results were compared with the experimental data in present study and that in several previous researches, meanwhile, several prediction models proposed in previous studies were analyzed as well.

5.2 Experimental Setup

Figure 5.1 shows the schematic of the experimental setup used in present study to obtain the precise shape of the impact droplet at the maximum spreading. The DIP setup (as shown in figure 5.1 (a)) was comprised of a droplet generator, an experimental chamber containing the solid impact substrate, a projector and a relevant lens system, a high-speed camera, and a host computer controlling both the projector and high-speed camera. Comparing with the DIP setup, a 20W LED spotlight and relevant scattering glass was set at the rear part of the experimental chamber for side-view setup (as shown in figure

5.1 (b)), and the high-speed camera was configured parallel to the surface of the solid substrate.

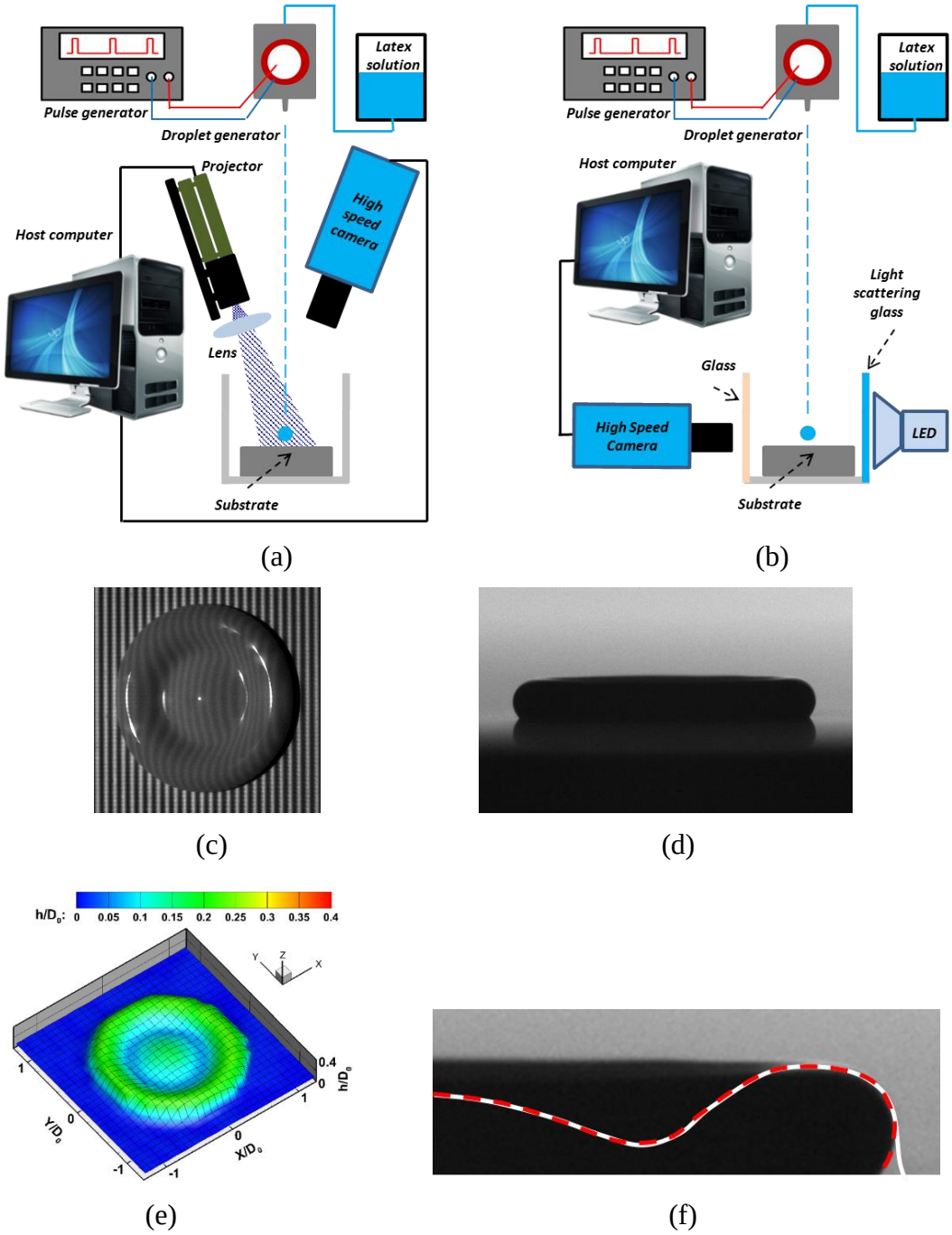

Figure 5.1 Experimental setup for measurement of the maximum spreading of the impacting droplet

(a) Setup for 3-D reconstruction of the impacting droplet by using DIP technique; (b) Setup for 2-D profile measurement of the impacting droplet; (c) The projected line pattern modulated by the impact droplet reaches the maximum spreading ($D_0 = 2.36mm, U_0 = 0.76m/s$, $\mathrm{Re} = 1727, \mathrm{We} = 25$); (d) Side-view of the impact droplet reaches the maximum spreading; (e) The 3D shape of the droplet measured by using DIP technique. (f) The averaged 2-D profile of the impact droplet, the white solid line is the averaged 2-D profile based on the 3-D reconstruction droplet shape, and the red dashed line is the averaged 2-D profile revised by the side-view of the droplet.

A volume-type droplet generator system was used to generate single water droplets. The system includes three parts: a piezo-actuated cavity, a pulse generator (Rigol 1074Z-S), and a water reservoir bottle. The main part of the droplet generator system includes a water cavity, a piezoelectric plate, and a droplet nozzle. The water cavity and droplet nozzle were rapid prototyped. Upon receiving a pulse signal from the pulse generator, the piezoelectric plate would warp and squeeze the water cavity, which would extrude a droplet from the nozzle. With suitable pulse voltage and duration, the droplet generator could eject a single droplet from each pulse. The droplet size was controlled by the nozzle inner diameter and the pulse voltage, and the droplet impingement velocity was controlled by the initial ejection velocity and the height between the droplet generator and the solid substrate. The size variation of the generated droplets when using the same pulse shape and the same nozzle was less than 0.05mm. The droplet size can be controlled from about 1.5mm to 3.0mm by using different inner diameter nozzles and different pulse voltages.

A DLP projector (Young Optics Light Crafter) was used to project the fringe pattern on the test plate for the DIP measurement. The distance between each two adjacent lines was set to be about 0.15 mm to satisfy the measurement resolution requirement (in our

study, the droplet initial diameter is about 2.4mm, and the maximum spreading diameter of the droplet was more or around 5mm). A high-speed camera (PCOtech Dimax S4) was used for recording the light pattern images. The frame rate of the high-speed camera was set to 5,000fps and the exposure time was set to $100\mu s$ to adequately time-resolve the dynamic process and minimize motion blur. The recorded images had a spatial resolution between $624\ pixels \times 620\ pixels$ to $912\ pixels \times 900\ pixels$, and a physical measurement window size between $9.2mm \times 9.1mm$ to $13.4mm \times 13.2mm$. The window sizes were selected depending on the expected spreading diameter for a particular trial.

Table 5.1 The impact conditions of the droplets

	D_0 (mm)	U_0 (m/s)	ρ (kg/m^3)	μ $(mPa \cdot s)$	γ (mN/m)	Re	We	θ_a (deg)
1	2.39 ± 0.04	0.76~ 2.79	1011	1.05	55.1	1725~ 6450	25~345	80
2	2.33 ± 0.01	0.76~ 2.45	1104	4.66	42.5	425~ 1365	36~367	74
3	2.31 ± 0.01	0.76~ 3.08	1163	15.75	52.3	135~ 536	32~495	82

The impact conditions of the droplets were shown in table 5.1. Three different kinds of liquid mixture of Latex, glycerol and water were used in this study, the mixture percent were 5%Latex - 95%water, 5%Latex - 40%glycerol - 55%water, and 5%Latex - 60%glycerol - 35%water, respectively. To enhance the light diffusion on the droplet

surface, a low concentration (5% by volume) of latex flat wall & trim paint (ColorPlace, Interior Flat, Light Base, 5040C) was added to the water-glycerol solutions. A Stormer viscometer was used to measure viscosity of those three liquid mixture, and the measured results also validated that the mixture still shew Newtonian properties. With the percent increase of glycerol, the viscosity of the droplet increased from 1.05 $mPa \cdot s$ to 15.75 $mPa \cdot s$, while the surface tension were 55.1 mN/m, 42.5 mN/m and 52.3 mN/m, respectively. The impact substrate was mounted in a relatively closed experimental chamber to minimize the environmental disturbances. The main part of the substrate is an aluminum plate ($2inch \times 2inch \times 1/4inch$). The plate surface was coated with white paint (Rustoleum enamel), and was wet-sanded with 2000 grit sandpaper. The advancing and receding contact angles on the surface were measured as about 80 degrees and less than 20 degrees respectively. By adjusting the droplet release height, the impact velocity varied from 0.76m/s to about 3m/s.

Figure 5.1(c) shows the projected line pattern modulated by the impact droplet reaches the maximum spreading, and figure 5.1(e) shows the 3D shape of the droplet measured by the DIP technique. The droplet diameter before impact was 2.36mm, the impact velocity was 0.76m/s, and the density, viscosity and surface tension was 1011 kg/m^3 ,1.05 $mPa \cdot s$ and 55.1 mN/m, respectively, so that the corresponding Reynolds number and Weber number were 1727 and 25, respectively. The reconstructed 3D shape reflected most of the characteristics shown in figure 5.1(c), validating that the DIP technique can effectively work in this study. Since the high-speed camera was set to record the droplet impact process from a certain angle (15°comparing with the vertical

direction in this study) comparing with the vertical direction, the movement of the lower or bottom part of the droplet couldn't been recorded by the camera if the bottom or lower part of the droplet is smaller than the upper part, since the lower or bottom part would be blocked by the upper part. In this study, it was found that when the impact droplet reached the maximum spreading, the instantaneous contact angle was bigger than 90 degrees, so that the upper part was bigger than the lower part, and leading to the blocking of the lower part. The circumferentially-averaged 2D profile (cross section) of the droplet deduced from the 3D shape measured by the DIP technique as shown in figure 5.1(e) shows this blocking effectiveness, since it failed to show the lower profile of the droplet. In this study, all the droplets impact perpendicularly to the solid surface, therefore, we assumed that the droplets are axially symmetric, and the averaged thickness of the droplet is defined as:

$$\bar{h} = 1/(2\pi)\int_0^{2\pi} h(r,\theta)d\theta \tag{5.3}$$

Where r and θ are the usual cylindrical coordinates. To correct this blocking effectiveness, a side-view of the droplet was imported to obtain the 2D profile of the impact droplet blocking part (lower or bottom part), as shown in figure 5.1 (d). After combing the averaged 2D profile deduced from DIP measurement results and the 2D profile measured by the side-view, a revised 2D profile of the droplet as shown in figure 5.1(e) was achieved. It is needed to notice that the 3D shape based on the DIP technique and the 2D profile based on the side-view were not measured simultaneously to avoid the disturbance of the LED light to the projected pattern used in the 3D measurement by the DIP technique. To validate the repeatability of the experiment, each impact condition was tested at least three times, and the comparison results shows that the uncertainty was less than 3% based on

the instantaneous contact angle (advancing contact angle) when the droplet reached the maximum spreading.

5.3 Results and Discussions

5.3.1 Maximum spreading factor model development

Before droplet impact on the solid surface, there are three different kinds of energy as the kinetic, potential and surface energy needed to be considered. And when the droplet reaches the maximum spreading, the energy needed to be considered are the three kinks of energy considered before impacting besides the dissipated energy due to the viscosity. To find the maximum spreading factor, in principle the equations of energy conservation

$$E_{k0} + E_{p0} + E_{s0} = E_{k1} + E_{p1} + E_{s1} + W \tag{5.4}$$

and mass conservation

$$m_0 = m_1 \tag{5.5}$$

have to be solved[20]. Where, E_{k0}, E_{p0}, E_{s0} and m_0 are the kinetic, potential ,surface energy and mass of the droplets before impact, and E_{k1}, E_{p1}, E_{s1}, W and m_1 are the kinetic, potential, surface energy, dissipated energy and mass after impact. The kinetic, and surface energy before impact can be described by

$$E_{k0} = \frac{1}{2} m v_0^{\,2} = \frac{\pi}{12} D_0^{\,3} \rho U_0^{\,2} \tag{5.6}$$

$$E_{s0} = \gamma_1 S_0 = \pi D_0^{\,2} \gamma_{la} \tag{5.7}$$

where D_0, ρ, γ_{la} are the initial diameter, the density, and the surface tension of the impacting droplet between liquid droplet and air. The potential energy is due to the gravity

of the droplet, and the potential energy at the impact solid surface was set as 0, thus the potential energy can be presented as

$$E_{p0} = mgh_0 = \frac{\pi}{12}\rho g D_0^{\,4} \tag{5.8}$$

where g is the gravitational acceleration. Since the droplet diameter is quite small, normally less than 3mm, so that the potential energy is much smaller (normally less than two percent of the total energy) than other kinds of energy. And after impact, the potential energy would decrease due to the decrease of the height, thus, the potential energy was neglected in this study.

After impact, when the droplet reaches the maximum spreading diameter, the remaining kinetic energy is almost zero[35], since most of the kinetic energy before impact transferred to the surface energy and the energy dissipated due to the viscosity during the spreading process, thus the kinetic energy was assumed to be zero when the droplet reaches the maximum spreading diameter. Based on the work presented by Chandra and Avedisian[36], Pasandideh-Fard et al.[24] proposed a model estimating the dissipated energy

$$W = \frac{\pi}{3}\rho U_0^{\,2} D_0 D_{\max}^{\,2} \frac{1}{\sqrt{\mathrm{Re}}} \tag{5.9}$$

by assuming that liquid motion in the droplet can be represented by axisymmetric stagnation point flow[37]. Where D_{max} is the maximum spreading diameter.

There are three different kinds of surface energy as the energy between liquid droplet and air, the energy between liquid droplet and solid surface and the energy between air and solid surface needed to be considered when the droplet reaches the maximum spreading diameter. At this moment, the surface energy between air and solid surface is

replaced by that between liquid droplet and solid surface at the bottom of the droplet, thus, the surface energy was calculated as

$$E_{s0} = A\gamma_{la} + \frac{\pi}{4} D_{\max}{}^{2}\gamma_{ls} - \frac{\pi}{4} D_{\max}{}^{2}\gamma_{sa} \tag{5.10}$$

where A is the surface area between liquid droplet and air, γ_{la}, γ_{ls} and γ_{sa} are the surface tension between liquid droplet and air, between liquid droplet and solid surface, and between solid surface and air, respectively. In equation 5.10, the surface tension γ_{ls} and γ_{sa} are hard to be measured directly, however, based on Young's equation[38]

$$\gamma_{la}\cos\theta_Y = \gamma_{sa} - \gamma_{ls} \tag{5.11}$$

the equation 5.10 can be simplified as

$$E_{s0} = A\gamma_{la} - \frac{\pi}{4} D_{\max}{}^{2}\gamma_{la}\cos\theta_Y \tag{5.12}$$

where θ_Y is the Young contact angle. Most of the previous work assumed that the shape of the droplet as a cylinder when the droplet reaches the maximum spreading diameter, so that the equation can be furtherly simplified[36] as

$$E_{s0} = \frac{\pi}{4} D_{\max}{}^{2}\left(1-\cos\theta_Y\right)\gamma_{la} \tag{5.13}$$

and in this equation, the surface area considered is just the upper surface of the cylinder, neglecting the side area. Combining the equations for the different energy terms, results in an expression for the maximum spreading factor as[24]

$$\beta_{\max} = \sqrt{\frac{We+12}{3\left(1-\cos\theta_Y\right)+4\left(We/\sqrt{\mathrm{Re}}\right)}} \tag{5.14}$$

In this model, the θ_Y was represented by the "advancing" contact angle at the maximum spreading. The later research by Ukiwe et al.[25] proposed that the experimental advancing contact angle can be a better approximation of θ_Y[39], so after considering the side area of the cylinder neglected in the previous study, he extending the model 5.14 by using the experimental advancing contact angle θ_a to represent θ_Y as

$$\left(We+12\right)\beta_{\max}=8+\beta_{\max}{}^{3}\left[3\left(1-\cos\theta_{Y}\right)+4\frac{We}{\sqrt{\mathrm{Re}}}\right] \tag{5.15}$$

Although the cylinder assumption seems reasonable in some certain conditions, it is not precise enough, especially when the Re and We are small. As shown in figure 5.1 (c) and (d), the shape of the droplet is much more complicated than just a cylinder. In this study, the real surface area between liquid droplet and air was obtained based on the precise measurement of the droplet 3D shape, thus, the prediction discrepancy of the maximum spreading factor due to surface energy error caused by the cylinder assumption can be eliminated.

To apply the precise measurement results in the maximum spreading factor model, the surface area between liquid droplet and air was represented by the droplet bottom area between liquid droplet and solid surface with a specific factor *f* when the droplet reaches the maximum spreading diameter. The f was calculated as $f = S_u/S_b$, where S_u is the surface area between droplet and air, and S_b is the surface area between droplet and solid surface. For a liquid droplet normally impact on a solid surface, the impact process will be affected by the droplet size, impact velocity, the liquid viscosity and the liquid surface tension. Those parameters can be represented by the droplet Reynolds number and Weber

number, thus, finding the relationship between the specific factor *f* and the Re and We is a consequent step to apply the precise measurement results in the spreading factor model.

Figure 5.2 shows the surface area factor *f*-1 as a function of Reynolds number and Weber number for three different liquid mixture droplets, and the droplet parameters of the droplets were shown in table 1. As shown in figure 5.2(a), with the increase of the Weber number, *f*-1would decrease nearly linearly under logarithmic coordinate system, and similar variation tendency can be seen in figure 5.2 (b). With the increase of Weber number, *f*-1would also decrease nearly linearly under the logarithmic coordinate system. Those variation tendencies agree well with the physical process. As the increase of Reynolds or Weber number, the impact droplet tends to have a bigger spreading diameter, which makes the droplet more like a thin disk or cylinder, so that the special factor *f* tends to become one, and thus the *f*-1 tends to become zero. The difference between figure 5.2 (a) and (b) is that a higher viscosity droplet tends to have a bigger special factor under same Weber number, while it tends to have a smaller special factor under same Reynolds number. Based on the comparison results from figure 5.2 (a) and (b), it validated that the special area factor *f* would be affected by both of the Weber number and Reynolds number. After a combination of (a) and (b), a more reasonable relationship between *f*-1and $We * Re^{1/2}$ as shown in figure 5.2 (c)was constructed. In this new figure, the relationship can be represented by one single linear line under the logarithmic coordinate system as

$$f-1 = C\left[We\,\mathrm{Re}^{1/2}\right]^{-2/5} = CWe^{-2/5}\,\mathrm{Re}^{-1/5} \tag{5.16}$$

where $C = 6.78 \pm 0.01$ is a fitting constant obtained by means of a least-squares fit (with the coefficient of determination $R^2 = 0.95$). After applying this result in the energy equations, a revised model prediction the maximum spreading factor was constructed

$$\beta_{\max} = \sqrt{\frac{We + 12}{3\left(1 + CWe^{-2/5}\,\mathrm{Re}^{-1/5} - \cos\theta_Y\right) + 4\left(We/\sqrt{\mathrm{Re}}\right)}} \tag{5.17}$$

In this model , the Young contact angle θ_Y was also represented by the experimental advancing contact angle θ_a.

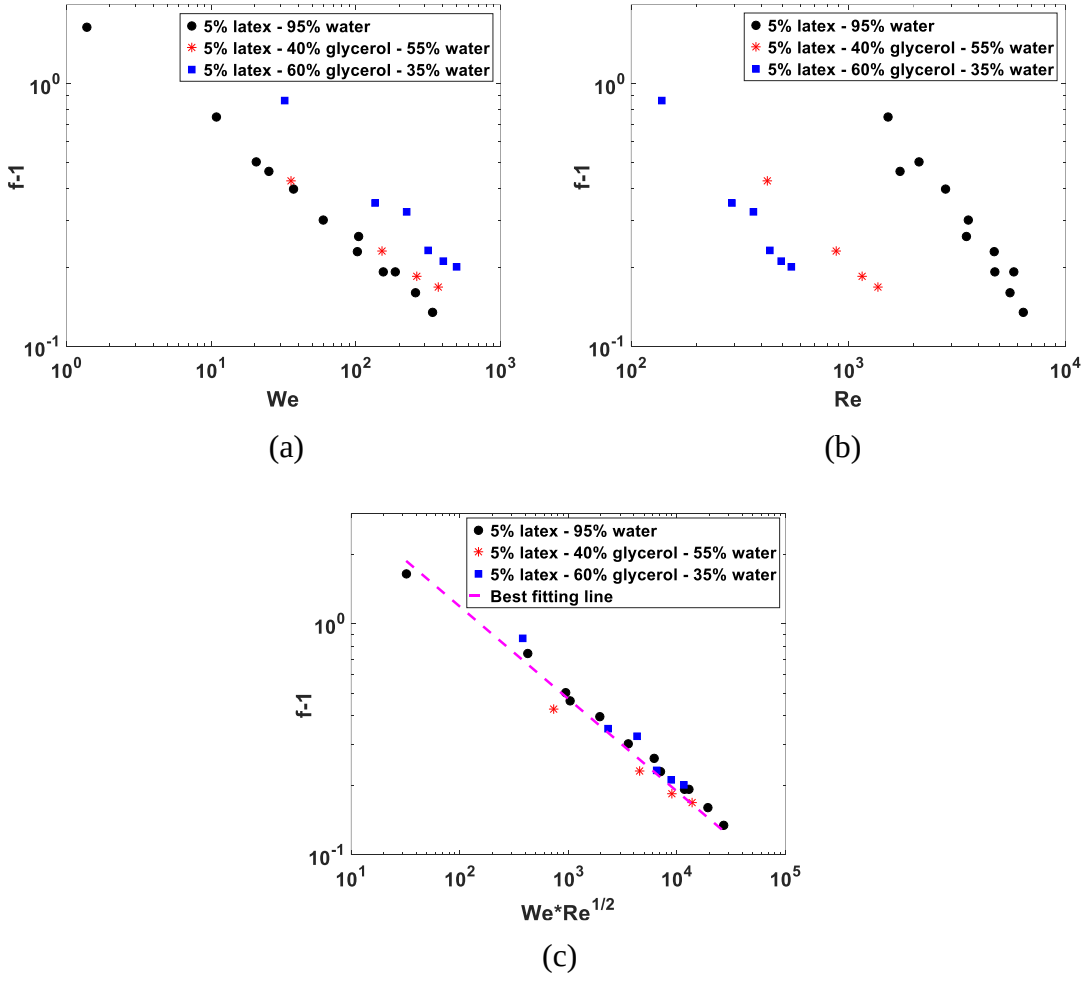

Figure 5.2 The surface area factor f as a function of Reynolds number Re, Weber number We and combination of Re and We as $We * Re^{1/2}$.

(a) The surface area factor as a function of Re; (b) The surface area factor as a function of We; (c) The surface area factor as a function of combination of Re and We as $We * Re^{1/2}$.

5.3.2 Model predictions and experimental results

To validate the revised maximum spreading factor model in this study, the model prediction results was compared with the experimental results in this study besides the experimental results from several other researchers. The comparison results were shown in figure 5.3. In this figure, the red stars represented the data from the research of Pasandideh-Fard et al.[24], the squares represented that from R.E. Ford et al.[40], the Inverted triangles represented that from H. Fukanuma et al.[41], the circles represented that from Lung Cheng[42], the hexagrams represented that from Roisman et al.[43], and the solid pentagram represented the experimental data from present work. Based on those experimental data, the ranges of the Weber number and Reynolds number are about $1\sim2300$ and $130\sim35000$, respectively.

Figure 5.3(a) is a plot of the comparison for the prediction model of equation 5.14 by pasandideh_Fard et al. with the experimental data. The model predictions agreement with the experimental data was good with a relative mean error of 8.51% and a standard deviation of 12.21%. The comparison for the prediction model of equation 5.15 with the experimental data was shown in figure 5.2(b) with a relative mean error of 8.31% and a standard deviation of 9.46%. Compare with that in figure 5.2(a), this extended model by Chijioke Ukiwe et al. has a higher prediction precision, however, the improvement is not distinct. The comparison results between the predictions of the revised model in present study of equation 5.17 and the experimental data was shown in figure 5.2(c) with a relative

mean error of 6.10% and a standard deviation of 7.63%. Compare with that in figure 5.2(b), the revised model has a much more distinct improvement in the prediction precision, especially when the Weber number and Reynolds number is small. When the Weber number or Reynolds number is small, the droplet tends to get a smaller spreading diameter, thus, the droplet shape would be much more complicated than a thin cylinder, as shown in figure 5.1 (c) and (d), and the thin cylinder assumption under those conditions can lead to relative more serious mistakes in calculating surface energy than that when the Weber number and Reynolds number are big. Moreover, the ratio of the surface energy in the total energy is bigger than that when the Weber number and Reynolds number are bigger, thus, the thin cylinder assumption was not reasonable under low Weber and low Reynolds number droplet impact conditions. The excellent agreement under low Weber number and low Reynolds number conditions ($\mathrm{We} < 50$ and $\mathrm{Re} < 3000$) shown in figure 5.2(c) shows that the revised model proposed in this study significantly reduce the error caused by the inaccurate surface energy calculation due to the cylinder assumption in previous study.

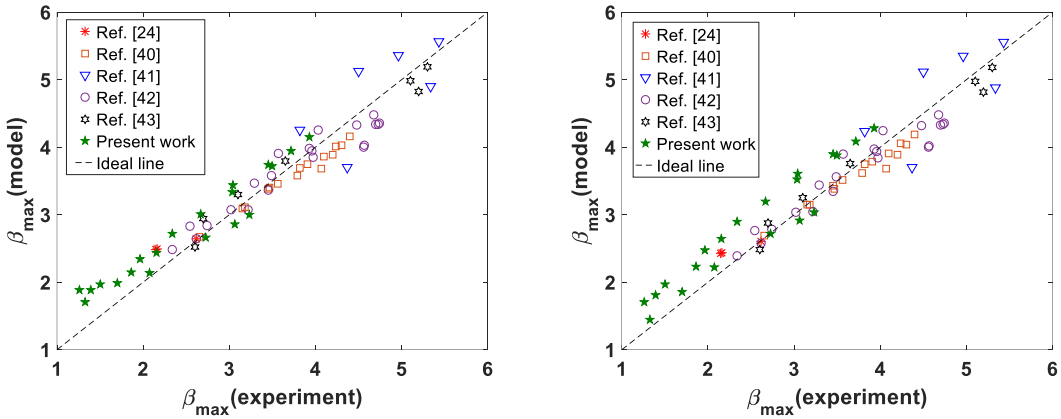

(a) (b)

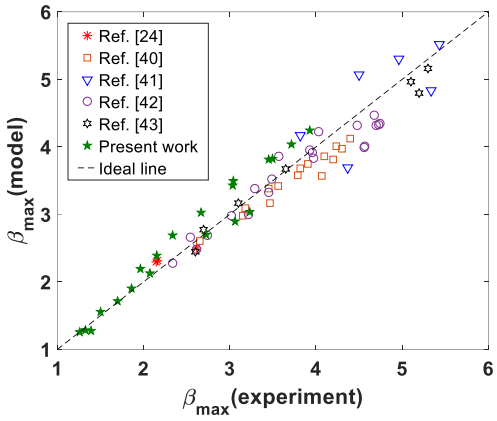

(c)

Figure 5.3 Comparison of the model (based on energy balance) prediction results with the experimental data

(a) Comparison of the Passandideh-Fard et al. model (ref 24) with the experimental data, with a relative mean error as $8.51\% \pm 12.21\%$; (b) Comparison of the Chijioke Ukiwe et al. model (ref 25) with the experimental data, with a relative mean error as $8.31\% \pm 9.46\%$; (c) Comparison of the revised model in present study with the experimental data, with a relative mean error as $6.10\% \pm 7.63\%$;

The models shown in figure 5.3 were based on the energy balance during the droplet impact process, and to further validate the revised model proposed in present study, two models without using energy balance were imported. Based on the assumption on the universal flow in the lamella[44] with the help of the expression for the residual film thickness, Ilia V. Roisman[27] develop a new scaling relation for the drop maximum spreading diameter as

$$\beta_{max} \approx 0.87\,\mathrm{Re}^{1/5} - 0.4\,\mathrm{Re}^{2/5}\,We^{-1/2} \tag{5.18}$$

Similar approach to Ilia V. Roisman, Jens Eggers et al.[9] gave a maximum spreading scale as

$$\beta_{max} \propto \mathrm{Re}^{1/5}\ f\left(We\,\mathrm{Re}^{-2/5}\right) \tag{5.19}$$

and then Nick Laan et al.[45] furtherly confirmed the equation 5.19 to be

$$\beta_{\max} = \mathrm{Re}^{1/5} P^{1/2} / (A + P^{1/2}) \tag{5.20}$$

where $\mathrm{P} \equiv \mathrm{We}Re^{-2/5}$, and $\mathrm{A} = 1.24 \pm 0.01$. Figure 5.4 shows the comparison results of these two models. As shown in figure 5.4(a), the model of equation 5.18 can predict well when the Weber number and Reynolds number were bigger, however, when the Weber number or Reynolds number were small, the model performed badly, it even shows negative diameter. The relative mean error is 16.16%, and the standard deviation is 18.27%, which shows that this model is not reasonable under low Weber number and Reynolds number impact conditions. Actually, the author explained that this model was suitable for high speed drop impact. Similar result can be found in figure 5.4(b). This figure shows the comparison of the model prediction of equation 5.20 with the experimental data, with a relative mean error of 8.13% and a standard deviation of 7.48%. Although this model performed much better than that of equation 5.18, however, the prediction under low Weber number and Reynolds number conditions needed to be improved.

Based on the comparison results with the experimental data and with other models, the revised model in present study can reasonablely predict the maximum spreading diameter in a wide range of Weber number and Reynolds number (1<We<2300, 130<Re<35000), especially under low Weber number and low Reynolds number droplet impact conditions (We<50, Re<3000).

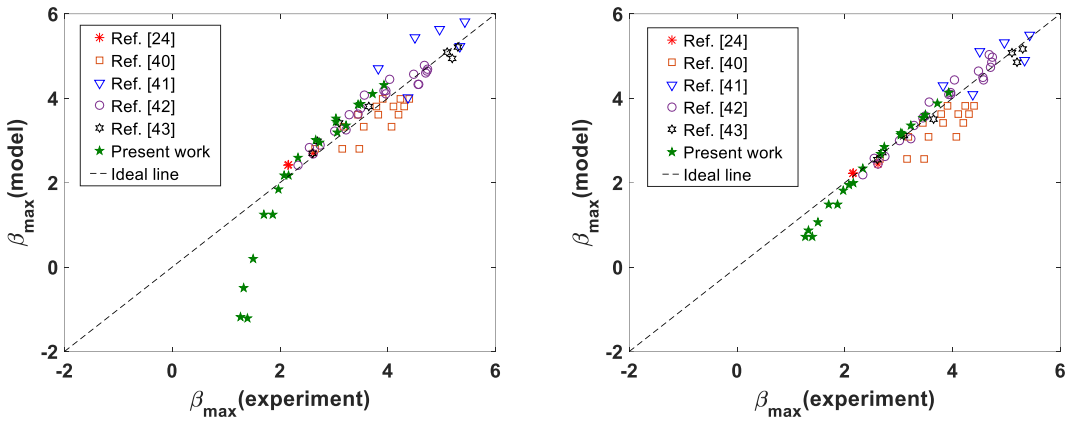

Figure 5.4 Comparison of the model (not based on energy balance) prediction results with the experimental data

(a) Comparison of the Ilia V. Roisman et al. model (ref 27) with the experimental data, with a relative mean error as $16.16\% \pm 18.27\%$; (b) Comparison of the Nick Laan et al. model (ref 45) with the experimental data, with a relative mean error as $8.13\% \pm 7.48\%$.

5.3.3 Discussions on Measurement Uncertainty

Figure 5.5 shows the measurement accuracy of the DIP technique in droplet thickness measurement. It shows the droplet volume calculated based on the 3D droplet shape based on the DIP technique during the entire impact process, the calculated based on the revised 3D droplet shape by combining the DIP measured results and side-view measured results, and the volume calculated based on initial droplet size before the droplet impact on the solid surface. In this case, the droplet initial diameter is 2.41mm, the impact velocity is 1.58m/s, and the corresponding Reynolds and Weber numbers are 3674 and 111 respectively. It shows that the DIP technique measurement results agree well with the calculated volume based on the initial droplet size, except that between about 1.5–4ms. This is because the DIP technique can only measure the top surface of the droplet, while it cannot measure the air thickness under the droplet, as shown in figure 5.1(c) and (d). In

the time between about 1.5–4ms, the droplet was in the spreading stage, and during this stage, the droplet spreading speed at the edge was faster than the contact line between droplet and the solid surface. Therefore, the air underneath the droplet, which is occluded from the view in the DIP image, was erroneously considered as part of the droplet during the thickness measurement. Thus, during the spreading process, the droplet volume measured by DIP technique is a little higher than that calculated based on initial droplet size before droplet impact on the surface. After combining the side-view measured results, the calculated volume become much more reasonable, as the red line shown in figure 5.5, which shows that the side-view revise can sufficiently reduce the measurement error caused by the blocking effect. During the impact process, the volume calculated based on DIP technique and side-view revise is continually a little smaller than that calculated based on initial droplet size, and this is due to the penetration of the light through the droplet surface. Even though the latex paint adds into the water significantly increase the light scattering on the droplet surface, the projected light still can penetrate the droplet surface due to the character of liquid. The compared results show that the relative measurement error of the volume was 2.56%, while the standard deviation was 0.94%.

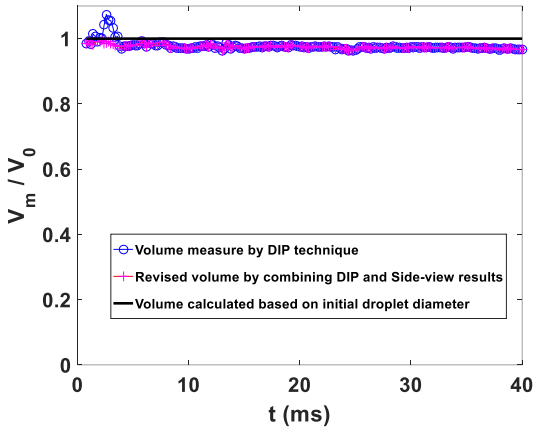

(a) Measured droplet volume (b) Droplet contact line during the spreading process.

Figure 5.5 Measurement accuracy of the DIP technique

5.4 Conclusions

In the present study, a digital image projection (DIP) technique was imported to measure the 3D shape of the droplet during the impact process. To measure the bottom or the blocked part' shape of the droplet during the spreading stage including the state when the droplet reaches the maximum spreading diameter, a side-view measurement was used. The comparison results between the volume calculated based on the 3D shape measured by combining DIP technique and side-view technique and the volume calculated by the initial size of the droplet before impact show that the using of the DIP technique in present study is reasonable, and the side-view technique can reduce the measurement error caused by the blocking effect. The relative mean error of the droplet volume during whole impact process was 2.56%, while the standard deviation was 0.94%.

Based on the precise droplet shape by combining the DIP technique and side-view results, a surface area factor representing the relationship between droplet upper surface area (surface between liquid droplet and air) and bottom surface area (surface between

liquid droplet and solid surface) was proposed. The analysis results shows that the factor has a linear relationship with $We Re^{1/2}$ under logarithmic coordinate system. By applying this factor in the droplet maximum spreading diameter model in the previous study, a revised model was developed.

By using the precise surface area calculated directly from measured results, the revised model can sufficiently reduce the prediction error caused by the shape assumption in the energy balance analysis. To validate the prediction precise, the predicted results were compared with the experimental data in present study and that in several previous researches, meanwhile, several prediction models proposed in previous studies were analyzed as well. Based on the comparison results with the experimental data and with other models, the revised model in present study can predict the maximum spreading diameter in a wide range of Weber number and Reynolds number ($1<We<2300$, $130<Re<35000$) reasonably, especially under low Weber number and low Reynolds number droplet impact conditions ($We<50$, $Re<3000$).

References

[1] Worthington, “On the forms assumed by drops of liquids falling vertically on a horizontal plate,” 1876, pp. 261–272.

[2] Eggers, J., and Villermaux, E., “Physics of liquid jets,” vol. 71, 2008.

[3] Planchon, O., “A Physical Model for the Action of Raindrop Erosion on Soil Microtopography,” vol. 74, 2010.

[4] Minemawari, H., Yamada, T., Matsui, H., Tsutsumi, J., Haas, S., Chiba, R., Kumai, R., and Hasegawa, T., “Inkjet printing of single-crystal films,” *Nature*, vol. 475, 2011, pp. 364–367.

[5] Ghodbane, M., Holman, J. P., and Sutherland, I., “Ex ~~ ri ~ e ~ tai study of spray cooping with Freon- ? 13,” 1990.

[6] Attinger, D., Moore, C. B., Donaldson, A., and Stone, H. A., “Fluid dynamics topics in bloodstain pattern analysis : Comparative review and research opportunities,” 2013.

[7] Antkowiak, A., Audoly, B., and Josserand, C., “Instant fabrication and selection of folded structures using drop impact,” vol. I.

[8] Rein, M., “Phenomena of liquid drop impact on solid and liquid surfaces,” vol. 12, 1993, pp. 61–93.

[9] Eggers, J., Fontelos, M. A., Josserand, C., and Zaleski, S., “Drop dynamics after impact on a solid wall : Theory and simulations,” 2010, pp. 1–13.

[10] Raman, K. A., Jaiman, R. K., Lee, T., and Low, H., “International Journal of Heat and Mass Transfer Lattice Boltzmann simulations of droplet impact onto surfaces with varying wettabilities,” *International Journal of Heat and Mass Transfer*, vol. 95, 2016, pp. 336–354.

[11] Lunkad, S. F., Buwa, V. V, and Nigam, K. D. P., “Numerical simulations of drop impact and spreading on horizontal and inclined surfaces,” vol. 62, 2007, pp. 7214–7224.

[12] Choi, M., Son, G., and Shim, W., “Numerical simulation of droplet impact and evaporation on a porous surface,” *International Communications in Heat and Mass Transfer*, vol. 80, 2017, pp. 18–29.

[13] Ruiter, J. De, Ende, D. Van Den, and Mugele, F., “Air cushioning in droplet impact . II . Experimental characterization of the air film evolution Air cushioning in droplet impact . II . Experimental characterization of the air film evolution,” vol. 012105, 2015.

[14] Liu, J., Vu, H., Yoon, S. S., Jepsen, R., and Aguilar, G., “SPLASHING PHENOMENA DURING LIQUID DROPLET IMPACT,” vol. 20, 2010, pp. 297–310.

[15] Riboux, G., and Gordillo, J. M., “Experiments of Drops Impacting a Smooth Solid Surface : A Model of the Critical Impact Speed for Drop Splashing,” vol. 024507, 2014, pp. 1–5.

[16] Gao, H., and Rose, J. L., “Ice detection and classification on an aircraft wing with ultrasonic shear horizontal guided waves,” *Ultrasonics, Ferroelectrics and Frequency Control, IEEE Transactions on*, vol. 56, 2009, pp. 334–344.

[17] Visser, C. W., Frommhold, P. E., Wildeman, S., Mettin, R., Lohse, D., and Sun, C., “Soft Matter numerical simulations and experiments at frame-,” *Soft Matter*, vol. 00, 2015, pp. 1–15.

[18] Engineering, M., Drive, E., and Engineering, E., “The air bubble entrapped under a drop impacting on a solid surface,” vol. 545, 2005, pp. 203–212.

[19] Street, G., and Street, G., “Air cushioning with a lubrication/inviscid balance,” vol. 482, 2003, pp. 291–318.

[20] Chr. Mundo, M. Sommerfeld, C. T., “Droplet-Wall Collisions: Experimental Studies of the Deformation and Breakup Process,” vol. 21, 1995.

[21] Rioboo, R., Heat, E., and Sa, P., “Outcomes from a Drop Impact on Solid Surfaces,” 2001.

[22] Statistique, P., and Lhomond, R., “Retraction dynamics of aqueous drops upon impact on non-wetting surfaces,” vol. 545, 2005, pp. 329–338.

[23] Scheller, B. L., and Bousfield, D. W., “Newtonian Drop Impact with a Solid Surface,” vol. 41, 1995, pp. 1357–1367.

[24] Fard, M. P., Qiao, Y. M., Chandra, S., Mostaghimi, J., Qiao, Y. M., Chandra, S., and Mostaghimi, J., “Capillary effects during droplet impact on a solid surface Capillary effects during droplet impact on a solid surface,” vol. 650, 1996.

[25] Ukiwe, C., and Kwok, D. Y., “On the Maximum Spreading Diameter of Impacting Droplets on Well-Prepared Solid Surfaces,” 2005, pp. 666–673.

[26] CLANET, C. S., BE´GUIN, C. D., RICHARD, D., and QU ´ ER ´E, D., “Maximal deformation of an impacting drop ´,” vol. 517, 2004, pp. 199–208.

[27] Roisman, I. V, and Roisman, I. V, “Inertia dominated drop collisions . II . An analytical solution of the Navier – Stokes equations for a spreading viscous film Inertia dominated drop collisions . II . An analytical solution of the Navier – Stokes equations for a spreading viscous film,” vol. 052104, 2010.

[28] Josserand, C., and Thoroddsen, S. T., “Drop Impact on a Solid Surface,” pp. 365–393.

[29] Bartolo, D., Josserand, C., and Bonn, D., “Singular Jets and Bubbles in Drop Impact,” vol. 124501, 2006, pp. 1–4.

[30] Li, H., Waldman, R. M., and Hu, H., “An Experimental Investigation on Unsteady Heat Transfer and Transient Icing Process upon Impingement of Water Droplets,” 2016, pp. 1–18.

[31] Liu, Y., Chen, W., Bond, L. J., and Hu, H., "An experimental study on the characteristics of wind-driven surface water film flows by using a multi-transducer ultrasonic pulse-echo technique An experimental study on the characteristics of wind-driven surface water film flows by using a multi-transducer ultrasonic pulse-echo technique," vol. 012102, 2017.

[32] Hu, H., Wang, B., and Zhang, K., "Quantification of transient behavior of wind-driven surface droplet / rivulet flows using a digital fringe projection technique," *Journal of Visualization*, 2015, pp. 705–718.

[33] Dai, J., Li, B., and Zhang, S., "High-quality fringe pattern generation using binary pattern optimization through symmetry and periodicity," *Optics and Lasers in Engineering*, vol. 52, 2014, pp. 195–200.

[34] Zhang, K., Wei, T., and Hu, H., "An experimental investigation on the surface water transport process over an airfoil by using a digital image projection technique," *Experiments in Fluids*, vol. 56, 2015, p. 173.

[35] Lee, J. B., Derome, D., Dolatabadi, A., and Carmeliet, J., "Energy Budget of Liquid Drop Impact at Maximum Spreading: Numerical Simulations and Experiments," 2016.

[36] Chandra, S., and Avedisian, C. T., "On the collision of a droplet with a solid surface," *Proc. R. Soc. London, Ser. A*, vol. 432, 1991, pp. 13–41.

[37] "38-Frank M. White viscous_fluid_flow_frank_m_white_second_edition.pdf."

[38] Young, T., "An Essay on the Cohesion of Fluids," 1805, pp. 65–87.

[39] Neumann, A. W., "ANGLES AND THEIR TEMPERATURE DEPENDENCE : THERMODYNAMIC INTERPRETATION with a solid yields , as has been verified several times in recent years6- ', the Laplace equation of capiflarity," 1974.

[40] "Impact and spreading of spray drops on foliar surfaces," *in Wetting*, 1967, pp. 417–432.

[41] Ohmori, H. F. and A., "Behavior of molten droplets impinging on flat surfaces," *the 7th National Thermal Spray Conference, Boston, MA*, 1994, pp. 563–568.

[42] Cheng, L., "Dynamic Spreading of Drops Impacting onto a Solid Surface," *Ind. Eng. Chem*, vol. 16, 1977.

[43] Roisman, B. I. V, "Normal impact of a liquid drop on a dry surface :," 2002, pp. 1411–1430.

[44] Roisman, I. V, Berberović, E., Tropea, C., Roisman, I. V, Berberovi, E., and Tropea, C., “Inertia dominated drop collisions . I . On the universal flow in the lamella Inertia dominated drop collisions . I . On the universal flow in the lamella,” vol. 052103, 2016.

[45] Laan, N., Bruin, K. G. De, Bartolo, D., Josserand, C., and Bonn, D., “Maximum Diameter of Impacting Liquid Droplets,” vol. 044018, 2014, pp. 1–7.

CHAPTER 6
DAMPED HARMONIC SYSTEM MODELING OF DROPLET OSCILLATING DYNAMICS DURING THE OSCILLATING STAGE ON A HYDROPHILIC SURFACE

6.1 Introduction

Droplet impact, which has been studied extensively since 1876[1], has a very wide range of applications, including atomization processes[2], raindrop dynamics[3], inkjet or 3D printing[4], spray cooling of hot surfaces[5], blood pattern and drop trajectories[6], and micro-fabrication[7]. While it also involves most of the key issues of surface flows, droplet impact is characteristic of multiphase flows[8]. The subject is so important that numerous researchers have investigated the droplet impact based on numerical modeling[9–12], or experimental methods[13–17]. A typical droplet impact process can usually be divided into three stages, a spreading or splash stage[18,19], a receding or rebounding stage[20], and a oscillating stage . In certain conditions, the oscillating stage is much longer than the spreading and receding stage, thus the predictions of the dynamics of the impact droplet during the oscillating stage can help enable higher-precision three-dimensional printing or enhanced droplet and spray cooling. While many of the previous researches focused on the spreading and receding stages, as developing tools to predict the maximum spreading diameter of the droplet, few attempts have been made to investigate the transient droplet behavior during the oscillating stage.

When predicting the dynamic droplet behavior, the computational modeling is an attractive means, however, the process is challenging as it requires accurate tracking and

prediction of the continuously deforming gas-liquid interface. Moreover, the contact line velocity along with impact substrate and liquid properties has not been universally successful in achieving the level of accuracy that is needed for simulations. Thus, a simple model that can predict the dynamic behaviors during oscillating stage is desirable. A few previous studies already proposed some models, for example, for example, Manglik[21]developed a damped harmonic system model to predict the dimensionless spread factor β $(= \mathrm{D}/D_0)$ and flatness factor δ $(= \mathrm{h}/D_0)$, where D and h are the droplet diameter and the height of upper surface central point of the droplet during the droplet post-impact process, and D_0 is the initial diameter of the droplet before impacting. In this damped harmonic system model, the damping coefficient and frequency of the oscillation were calculated based on semi-empirical models derived from measured experimental results, and the Reynolds number and Weber number as in equation 6.1 and 6.2 were set as the variables in the semi-empirical models.

$$\mathrm{Re} = \frac{\rho U_0 D_0}{\mu} \sim \frac{inertia}{viscous\ force} \tag{6.1}$$

$$\mathrm{We} = \frac{\rho {U_0}^2 D_0}{\gamma} \sim \frac{inertia}{surface\ tension} \tag{6.2}$$

Where U_0 is the droplet initial impacting velocity, ρ, μ and γ are the density, the viscosity of the droplet and the surface tension on the interface between liquid droplet and gas, respectively. To further illustrate the complex interplay of the inertial, viscous, and capillary forces during droplet impact process, two more dimensionless numbers as Capillary number and Ohnesorge number were imported

$$Ca = \frac{\mu U_0}{\gamma} = \frac{We}{\mathrm{Re}} \sim \frac{viscous\ force}{surface\ tension} \tag{6.3}$$

$$Oh = \frac{\mu}{\sqrt{\rho \gamma D_0}} = \frac{\sqrt{We}}{\mathrm{Re}} \sim \frac{viscous\ force}{surface\ tension} \times \frac{viscous\ force}{inertia} \tag{6.4}$$

Manglik's study help find a simple model that predicts the dynamics of droplet during the oscillating stage, however, this model was proposed based on the experimental results when droplet impacting on hydrophobic surface, and only suitable for predicting the droplet behavior on hydrophobic surface. Thus, a simple model that can predict the droplet behavior during oscillating stage when impacting hydrophilic surface is desired.

In previous studies, the most frequently used method to record the droplet impact process was the so called "side-view" technique. For the side-view technique, a high speed camera was set parallel to the surface of the solid substrate, thus, the camera can record the 2D profile of the droplet during the impact process. When a droplet normally impacts on a flat surface, it is acceptant to assume that the impact droplet is axially symmetric, and a 2-D profile can represent the real shape of the droplet. However, if the impact direction was not perpendicular to the impact surface, or the surface was not flat enough, then the real droplet shape during the impact process would be much more complicated, and a 2-D profile cannot represent of the real shape[22]. Moreover, in some moments during the droplet impact process, the central region of the droplet is lower than the outer region[23], and thus the central region information is blocked by the outer region, which leads to the failure of obtaining droplet shape information by side view. A method which can record real 3-D shape information of impact droplet is needed. At present, there are several techniques can collect the thickness information of objects, e.g., using multi-transducer

ultrasonic pulse-echo technique was used to measure the film flow thickness[24], and using space-time-resolved Fourier transform profilometry technique (FTP) to measure the 3-D shape of objective[25,26]. The ultrasonic pulse-echo technique can just do point thickness measurement, while the FTP technique need several different successive fringe patterns to achieve high accuracy measurement, which leads to the limitation of the time resolution. Since the droplet impact process, especially the spreading stage is quite fast and needs high time resolution 3-D shape information to analyze the dynamics during the impact process, a method which can achieve both thickness measurement of the full droplet and high time resolution is needed.

In the present study, a damped harmonic system modeling of oscillating stage of droplet impacting on hydrophilic surface reflecting flatness factor β was proposed based on the experimental results. A digital image projection (DIP) technique[27] was used to achieve the precise measurement of the impact droplet shape during the droplet impact process. The model was developed using experimental data for temporal variations in the height of droplets of three different liquids, covering a large ranges of properties (surface tension and viscosity), Weber number We, and Reynolds number Re. To validate the model prediction accuracy, the predicted results were compared with the experimental data from the present study.

6.2 Experimental Setup

Figure 6.1 shows the schematic of the experimental setup used in the present study to obtain the precise shape of the impact droplet at the maximum spreading. The DIP setup (as shown in figure 6.1 (a)) was comprised of a droplet generator, an experimental

chamber containing the solid impact substrate, a projector and a relevant lens system, a high-speed camera, and a host computer controlling both the projector and high-speed camera.

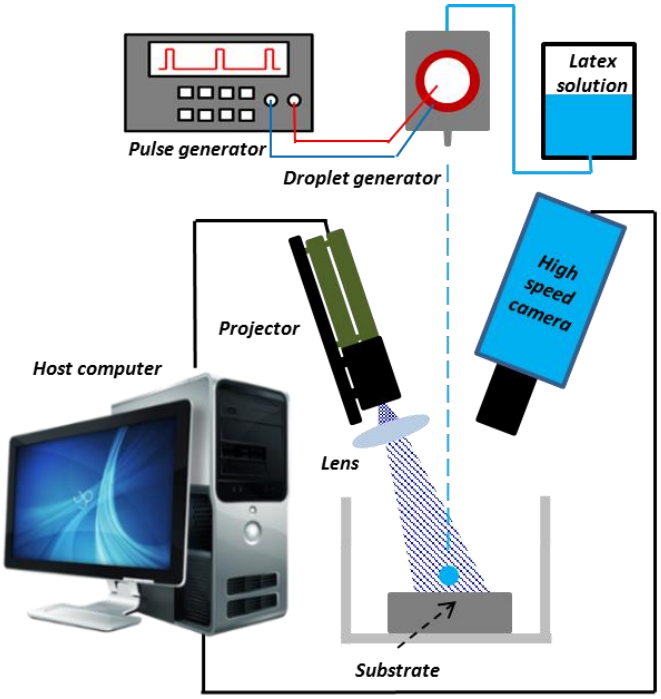

(a)

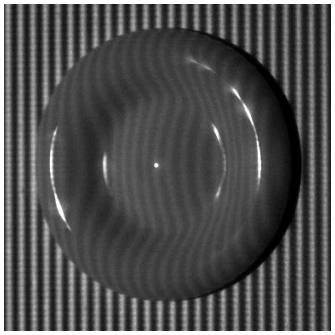

(b)

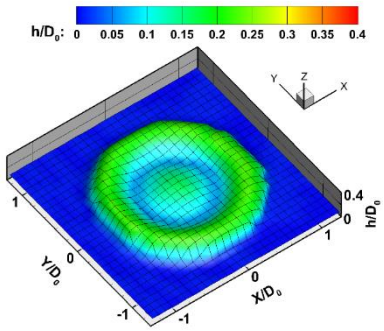

(c)

Figure 6.1 Experimental setup for measurement of the droplet shape variation during impact process

(a) Setup for 3-D reconstruction of the impacting droplet by using DIP technique; (b) The projected line pattern modulated by the impact droplet ($D_0 = 2.36mm, U_0 = 0.76m/s$, $\mathrm{Re} = 1727, \mathrm{We} = 25$); (c) The 3D shape of the droplet measured by using DIP technique.

A volume-type droplet generator system was used to generate single water droplets. The system includes three parts: a piezo-actuated cavity, a pulse generator (Rigol 1074Z-S), and a water reservoir bottle. The main part of the droplet generator system includes a water cavity, a piezoelectric plate, and a droplet nozzle. The water cavity and droplet nozzle were rapid prototyped. Upon receiving a pulse signal from the pulse generator, the piezoelectric plate would warp and squeeze the water cavity, which would extrude a droplet from the nozzle. With suitable pulse voltage and duration, the droplet generator could eject a single droplet from each pulse. The droplet size was controlled by the nozzle inner diameter and the pulse voltage, and the droplet impingement velocity was controlled by the initial ejection velocity and the height between the droplet generator and the solid substrate. The size variation of the generated droplets when using the same pulse shape and the same nozzle was less than 0.05mm. The droplet size can be controlled from about 1.5mm to 3.0mm by using different inner diameter nozzles and different pulse voltages.

A DLP projector (Young Optics Light Crafter) was used to project the fringe pattern on the test plate for the DIP measurement. The distance between each two adjacent lines was set to be about 0.15 mm to satisfy the measurement resolution requirement (in our study, the droplet initial diameter is about 2.4mm, and the maximum spreading diameter of the droplet was more or around 5mm). A high-speed camera (PCOtech Dimax S4) was used for recording the light pattern images. The frame rate of the high-speed camera was set to 5,000fps and the exposure time was set to $100\mu s$ to adequately time-resolve the dynamic process and minimize motion blur. The recorded images had a spatial resolution between $624\ pixels \times 620\ pixels$ to $912\ pixels \times 900\ pixels$, and a physical

measurement window size between $9.2mm \times 9.1mm$ to $13.4mm \times 13.2mm$. The window sizes were selected depending on the expected spreading diameter for a particular trial.

Table 6.1 The impact conditions of the droplets

	D_0 (mm)	U_0 (m/s)	ρ (kg/m^3)	μ $(mPa \cdot s)$	γ (mN/m)	Re	We	θ_a (deg)
1	2.39 ± 0.04	0.76~ 2.79	1011	1.05	55.1	1725~ 6450	25~345	80
2	2.33 ± 0.01	0.76~ 2.45	1104	4.66	42.5	425~ 1365	36~367	74
3	2.31 ± 0.01	0.76~ 3.08	1163	15.75	52.3	135~ 536	32~495	82

The impact conditions of the droplets were shown in table 6.1. Three different kinds of liquid mixture of Latex, glycerol and water were used in this study, the mixture percent were 5%Latex - 95%water, 5%Latex - 40%glycerol - 55%water, and 5%Latex - 60%glycerol - 35%water, respectively. To enhance the light diffusion on the droplet surface, a low concentration (5% by volume) of latex flat wall & trim paint (ColorPlace, Interior Flat, Light Base, 5040C) was added to the water-glycerol solutions. A Stormer viscometer was used to measure viscosity of those three liquid mixture, and the measured results also validated that the mixture still shew Newtonian properties. With the percent increase of glycerol, the viscosity of the droplet increased from 1.05 $mPa \cdot s$ to 15.75 $mPa \cdot s$, while the surface tension were 55.1 mN/m, 42.5 mN/m and 52.3 mN/m,

respectively. The impact substrate was mounted in a relatively closed experimental chamber to minimize the environmental disturbances. The main part of the substrate is an aluminum plate ($2inch \times 2inch \times 1/4inch$). The plate surface was coated with white paint (Rustoleum enamel), and was wet-sanded with 2000 grit sandpaper. The advancing and receding contact angles on the surface were measured as about 80 degrees and less than 20 degrees respectively. By adjusting the droplet release height, the impact velocity varied from 0.76m/s to about 3m/s.

Figure 6.1(b) shows the projected line pattern modulated by the impact droplet reaches the maximum spreading, and figure 6.1(c) shows the 3D shape of the droplet measured by the DIP technique. The droplet diameter before impact was 2.36mm, the impact velocity was 0.76m/s, and the density, viscosity and surface tension was $1011\,\mathrm{kg}/m^3$,1.05 $mPa \cdot s$ and 55.1 mN/m, respectively, so that the corresponding Reynolds number and Weber number were 1727 and 25, respectively. The reconstructed 3D shape reflected most of the characteristics shown in figure 6.1(b), validating that the DIP technique can effectively work in this study. With the help of the precisely reconstructing the droplet shape, the upper surface central height of the droplet was measured.

6.3 Results and Discussions

The impact solid substrate in present study is hydrophilic surface, and for the three liquid tested in present study, the receding contact angles this surface is nearly zero, so that the contact line of the droplet wouldn't recede back after the droplet reaches the maximum spreading diameter. And the dimensionless spread factor β investigated in

Manglik's work () would be a constant after the droplet reaches the maximum spreading diameter in present study. Thus, the present study would focus on the flatness factor δ.

6.3.1 Damped harmonic model development

The previous experimental results showed that the upper central height variation during the oscillating stage was similar to a damped harmonic oscillator, so that a damped harmonic model was proposed to predict the dynamic behavior of the droplet during the oscillating stage. At the end of the spreading stage, the kinetic energy inside the droplet is nearly zero, thus the main energy at this moment inside the droplet is the surface energy[28]. Thus, the surface energy dominates the motion of the droplet during the oscillating stage, and the oscillating of the droplet could be assumed as a second-order damped harmonic oscillator defined as[21,29]

$$m\ddot{x} = -kx - c\dot{x} \tag{6.5}$$

where, x is the deflection from a neutral (the central point thickness when the droplet is finally rest on the solid surface), $\dot{x}$ and $\ddot{x}$ are, respectively, the first- and second-order time derivatives. m is the mass of the system (the droplet mass), k is a spring constant which related with the surface tension of the droplet, and c is a damping coefficient which related with the viscosity of the droplet. To solve this differential equation, the required initial conditions are the initial displacement $x(0)$ and the initial velocity $\dot{x}(0)$. The general solution for equation 6.5 is

$$x(t) = e^{-(\alpha t/2)}[A\cos(\eta t) + B\sin(\eta t)] \tag{6.6a}$$

$$\alpha = c/m,\ \eta = \sqrt{\omega^2 - (\alpha/2)^2},\ A = x(0),\ B = \frac{1}{\eta}\left[\dot{x} + \frac{\eta}{2}x(0)\right] \tag{6.6b}$$

Where α is the viscous damping factor, ω is the corresponding un-damped angular frequency of the oscillator.

As the droplet central point reaches its post-impact maximum thickness at end of the retracting stage or at the beginning of the oscillating stage, the contact line velocity and the rate of change in thickness become zero. Thus, because the damped harmonic systems model begins at the instant of post-impact maximum thickness, for the subsequent damped oscillator motion the initial conditions are given by

$$h_c(0)/D_0 = h_{c\max}/D_0,\ \dot{h}_c(0)/D_0 = 0 \tag{6.7}$$

where h_{cmax} is the maximum upper central height of the droplet after the spreading and receding stage.

In the present study, for further uncovering the physics under the droplet dynamics during the oscillating stage, a dimensionless time τ defined as

$$\tau = t/\tau_0 \tag{6.8}$$

was imported to represent the time. Where t is the real time after the start of the oscillating stage, and τ_0 is the characteristic time defined as

$$\tau_0 = D_0/U_0 \tag{6.9}$$

By referencing the time-dependent response to the equilibrium condition (the condition when the droplet is finally rest on the impact surface), the variation of the central point thickness can be obtained as

$$\delta = h_c(\tau)/D_0 = h_{ceq}/D_0 + \exp(-\alpha\tau/2)[A\cos(\eta\tau) + B\sin(\eta\tau)] \tag{6.10a}$$

$$\eta = \sqrt{\omega^2 - (\alpha/2)^2}\ ,\ A = \left(h_c(0) - h_{ceq}\right)/D_0\ ,\ B = \frac{1}{\eta}\left[\dot{h}_c(0) + \frac{\alpha}{2}\left(h_c(0) - h_{ceq}\right)\right]/D_0 \qquad (6.10b)$$

where h_{ceq} is the upper central surface height of the droplet after the droplet impact process and when the droplet reaches the equilibrium state. Based on equation 6.10, to obtain the flatness factor, it is needed to find α, ω, h_{cmax}, and h_{ceq}.

The damping coefficient α determines the decay in the amplitude, whereas both constant and the damping coefficient govern the frequency ω of oscillator, and the viscous damping coefficient α can be scaled and correlated as a function of Reynolds number[21]

$$\alpha = f(\mathrm{Re}) \qquad (6.11)$$

while the frequency of oscillation ω can be scaled by the Reynolds and We numbers[21]

$$\omega = f(We, \mathrm{Re}) \qquad (6.12)$$

The damping factor α can be related to the ratio of the amplitude between successive peaks, while the frequency ω can be related to the time difference between successive peaks.

The damping coefficient α and the frequency of oscillation ω, as indicated in equation 6.11 and 6.12, are functions of Re and (We, Re), respectively. These were obtained by regression analysis of the experimental results as follows:

$$\alpha = -0.25\ln(\mathrm{Re}) + 2.14 \qquad (6.13a)$$

$$\omega = -0.12\ln(\mathrm{Re}\cdot We) + 2.66 \qquad (6.13b)$$

The predicted variations in α and ω given by equations 6.13a and 6.13b are compared with the experimental measurements in figure 6.2.

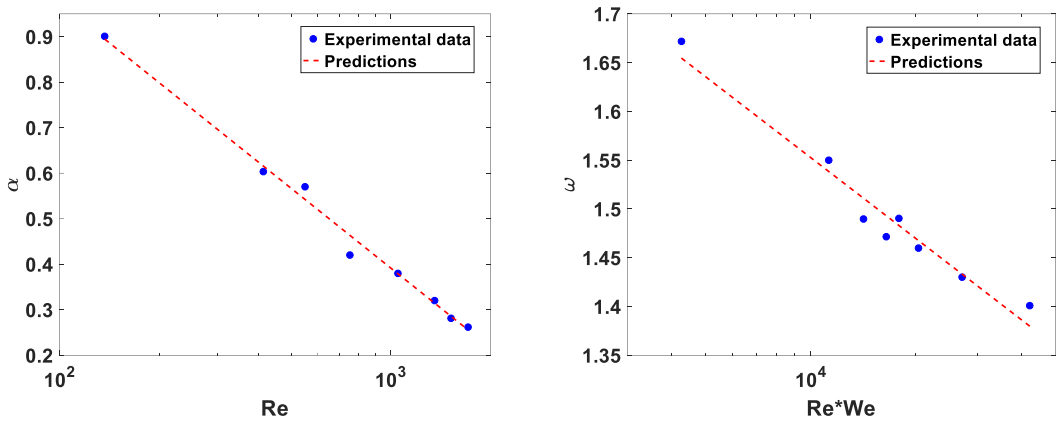

(a) (b)

Figure 6.2 Comparison of predictions of the damping coefficient α and frequency of the oscillator ω from equation 6.13a and 6.13b with experimental data.

(a) The damping coefficient α as a function of Reynolds number Re; (b) The frequency of the oscillator ω as a function of Re*We.

For predicting the maximum upper central height of the droplet after the spreading and receding stage h_{cmax}, a semi-empirical formula as

$$h_{c\max} = 19.81We^{-0.67} \tag{6.14}$$

proposed by regression analysis of the experimental data in the present study. After droplet reaching the maximum spreading diameter, the main energy inside the droplet would be the surface energy, and the surface tension of the droplet would dominate the dynamic motion (), thus, it is reasonable to assume that the characteristic maximum upper central surface height h_{cmax}/D_0 (droplet reaches the maximum upper surface central height after it reaching the maximum spreading diameter) of the droplet can be scaled and correlated as a function of weber number. This formula shows the relationship between the height and the Weber number We of the impact droplet, thus, the maximum upper central height of the droplet after the spreading and receding stages can be predicted based on the droplet

impact parameters as the droplet initial diameter D_0, impacting velocity U_0, and the surface tension γ. Figure 6.3 shows the comparison of predictions of the maximum height from equation 6.14 with the experimental data, and the excellent agreement between the two is evident.

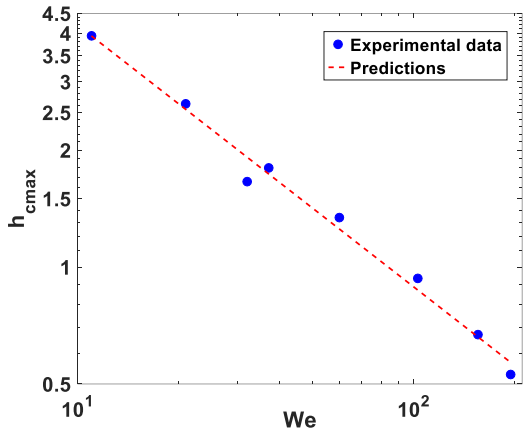

Figure 6.3 Comparison of predictions of the maximum upper central height h_{cmax}/D_0 from equation 6.14 with experimental data.

When reaches the equilibrium state, the droplet would finally be static on the solid surface. As the droplet impacting on hydrophobic surface, the upper surface central height h_{ceq} was predicted based on the static contact angle on the surface in the previous study (). However, the droplet was impacting on hydrophilic surface, and the droplet wouldn't retract back after reaching the maximum spreading diameter, so that the contact angle at the equilibrium stage cannot be represented by the static angle like that under hydrophobic condition, a new way to predict the h_{ceq} was needed. As the assumption in previous study (), the present study assumed that the shape of the droplet at the equilibrium state was a spherical crown, thus a formula calculated the h_{ceq} was proposed as

$$\frac{\pi h_{ceq}\left(\frac{3}{4}D_{eq}{}^{2}+h_{ceq}{}^{2}\right)}{6}=\frac{\pi D_{0}{}^{3}}{6} \tag{6.15}$$

In equation 6.15, the left part represents the droplet volume at the equilibrium state, the right part represents the droplet volume before impact, and the D_{eq} is the droplet diameter at the equilibrium state. As discussed in the upper part, the D_{eq} is equal to the diameter when the droplet reaches the maximum spreading diameter, so that

$$D_{eq}=D_{\max} \tag{6.16}$$

To predict the maximum spreading diameter D_{max}, a prediction model introduced in chapter 5 was imported

$$D_{\max}=D_{0}\sqrt{\frac{We+12}{3\left(1+6.78We^{-2/5}\,\mathrm{Re}^{-1/5}-\cos\theta_{Y}\right)+4\left(We/\sqrt{\mathrm{Re}}\right)}} \tag{6.17}$$

where θ_Y is the Young contact angle θ_Y represented by the experimental advancing contact angle θ_a, as shown in table 6.1. Combine equations 6.15 to 6.17, a formula predicting h_{ceq} was obtained

$$h_{ceq}\left(\frac{3}{4}D_{0}{}^{2}\frac{We+12}{3\left(1+6.78We^{-2/5}\,\mathrm{Re}^{-1/5}-\cos\theta_{Y}\right)+4\left(We/\sqrt{\mathrm{Re}}\right)}+h_{ceq}{}^{2}\right)=D_{0}{}^{3} \tag{6.18}$$

Combine the equations 6.7, 6.10, 6.13, 6.14 and 6.18, the damped harmonic oscillator predicting the droplet flatness δ was proposed as

$$\begin{cases} \delta = h_{ceq}/D_0 + \exp(-\alpha\tau/2)[A\cos(\eta\tau) + B\sin(\eta\tau)] \\ \eta = \sqrt{\omega^2 - (\alpha/2)^2}, \quad A = \left(h_{c\max} - h_{ceq}\right)/D_0, \quad B = \dfrac{\alpha}{2\eta}\left(h_{c\max} - h_{ceq}\right)/D_0 \\ \alpha = -0.25\ln\left(\mathrm{Re}\right) + 2.14 \\ \omega = -0.12\ln\left(\mathrm{Re}\cdot We\right) + 2.66 \\ h_{c\max} = 19.81We^{-0.67} \\ h_{ceq}\left(\dfrac{3}{4}D_0{}^2\dfrac{We+12}{3\left(1+6.78We^{-2/5}\,\mathrm{Re}^{-1/5}-\cos\theta_Y\right)+4\left(We/\sqrt{\mathrm{Re}}\right)} + h_{ceq}{}^2\right) = D_0{}^3 \end{cases} \tag{6.19}$$

6.3.2 Model predictions and experimental results

Figure 6.4 shows the transient variation of the flattening factor δ under different impact conditions. As shown in figure 6.4(a), the three lines represent the flattening factor under different conditions as: 5% latex 95% water mixture, we=24.7, Re=1709.5; 5% latex 40% glycerol 55% water mixture, We = 34.4, Re = 412.9; 5% latex 60% glycerol 35% water mixture, We = 31.2, Re = 137. When the Weber number is between 20 to 40, with the increase of the Reynolds number, the characteristic time τ needed for the droplet to be static would increase, it is because when the Reynolds number increase under these conditions (Weber number is between 20 to 40), the viscosity of the liquid would decrease, thus, the energy dissipated speed due to the fluid viscosity would decrease, so that the lower viscosity droplet could continue oscillate for a longer time.

Figure 6.4(b) to (c) show the comparison between the measured flattening factor and predicted flattening factor based on equation 6.19. The excellent agreement validate that the damped harmonic oscillator model can precisely predict the flattening factor under low Weber number conditions (20 < We < 40).

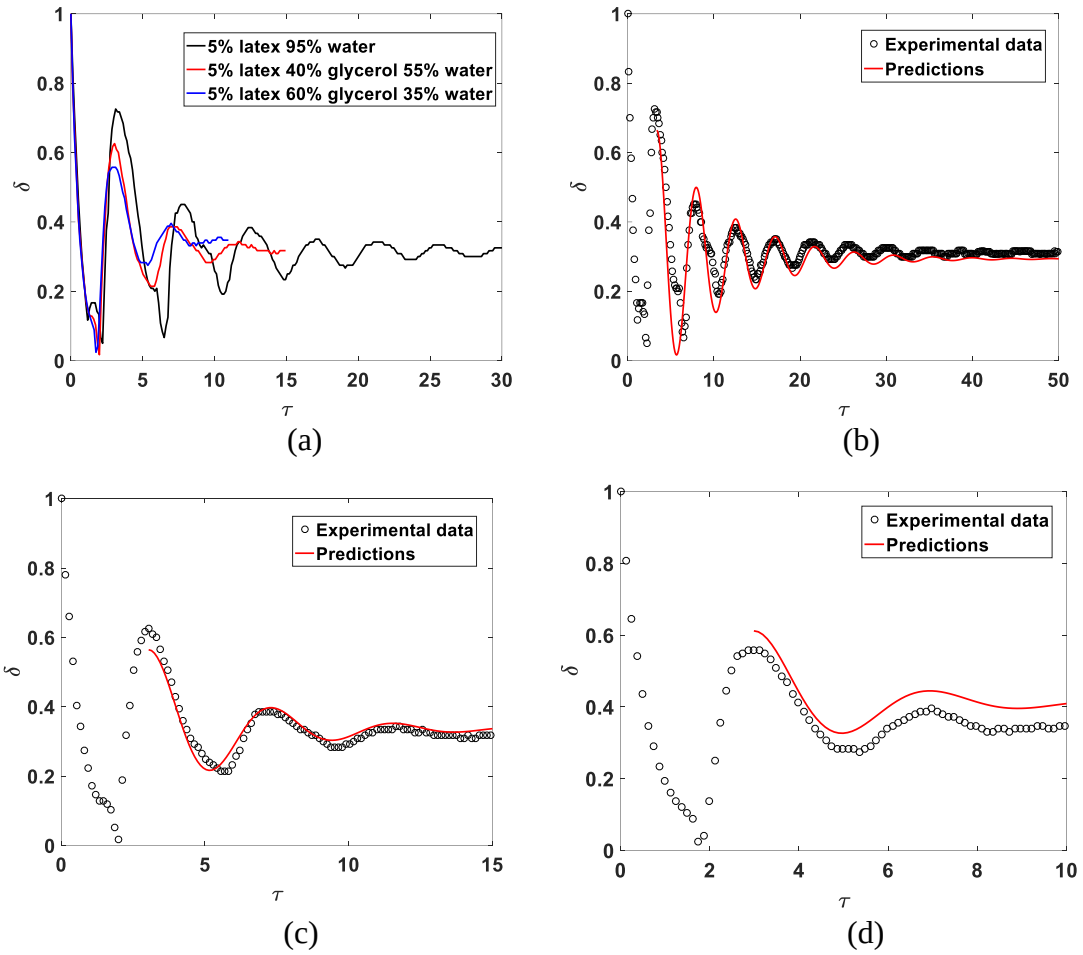

Figure 6.4 Transient variation of flattening factor δ of droplet on the solid substrate

(a) Compare of the experimental results under different conditions; (b) 5% latex 95% water mixture, We = 24.7, Re = 1709.5; (c) 5% latex 40% glycerol 55% water mixture, We = 34.4, Re = 412.9; (d) 5% latex 60% glycerol 35% water mixture, We = 31.2, Re = 137.

Figure 6.5 shows the transient variation of the flattening factor δ under different impact conditions. As shown in figure 6.4(a), the three lines represent the flattening factor under different conditions as: 5% latex 95% water mixture, we=24.7, Re=1709.5; 5% latex 95% water mixture, we=69.3, Re=2933.9; 5% latex 95% water mixture, we=110.6,

Re=3673.7. The last two cases' weber number is higher than 40, with the increase of the Reynolds number, the characteristic time τ needed for the droplet to be static would decrease, which conflicts with the conclusion got from figure 6.4. One possible reason for this conflict is that under this conditions, the viscosities of the droplets are same, however, with the increase of Reynold number, the droplet can reach a bigger spreading diameter, and the high hydrophilic of the impact surface reduce the droplet retract at the bottom boundary, and this reducing of the droplet retracting would help decrease the oscillating phenomenon of the droplet. Figure 6.5(b) shows the comparison of the measured results and the predictions based on equation 6.19, the droplet is 5% latex 95% water mixture, We = 110.6, Re = 2933.9, the huge deviation validate the conflicted conclusions in figure 6.4 and figure 6.5, a new model is desired to predict the droplet dynamics under high Weber number conditions.

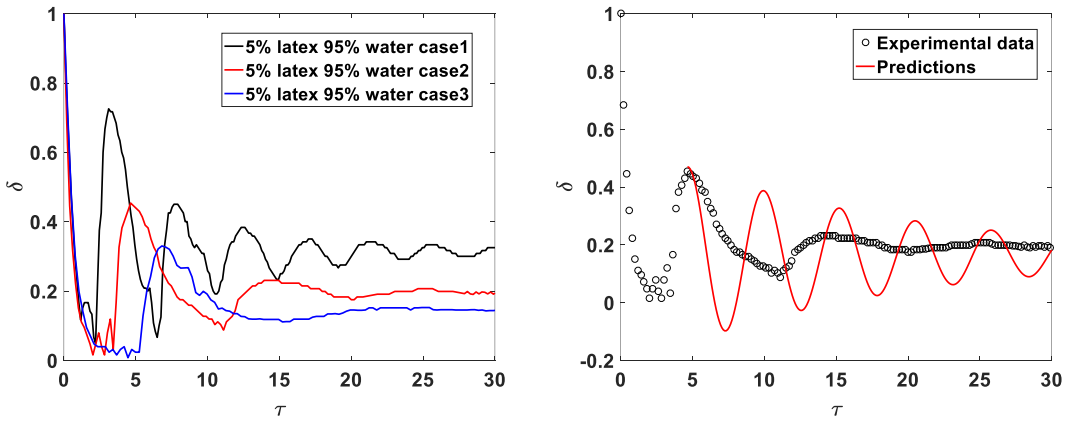

(a) (b)

Figure 6.5 Transient variation of flattening factor δ of droplet on the solid substrate with different impact velocity

(a) Compare of the experimental results under different conditions (with different impact velocity), Case1: We = 24.7, Re = 1709.5, Case2: We = 69.3, Re = 2933.9, Case3: We = 110.6, Re = 3673.7; (b) 5% latex 95% water mixture, We = 69.3, Re = 2933.9.

The comparison results show that the oscillating physics under low Weber number conditions is different from that under high Weber number conditions, and the damped harmonic oscillator model proposed equation 6.19 was only suitable for predicting low Weber number droplet impact.

6.4 Conclusions

In the present study, a digital image projection (DIP) technique was imported to measure the droplet upper surface central height during the impact process. Compare with the “side view” technique, the DIP technique could measure the central height when the droplet central part was lower than the outside part, while the “side view” technique would fail to obtain the central part information.

Based on the measurement results, it found that the oscillating dynamics under low Weber conditions ($10 < We < 40$) are different from that under high Weber number conditions. A damped harmonic oscillator model was proposed based on the experimental results under low Weber number conditions, and the comparison results shew that the model can do precise prediction in this region. To precisely predict the droplet oscillating dynamics under high Weber conditions, further investigations were needed to be done, and a new model was desired.

References

[1] Worthington, “On the forms assumed by drops of liquids falling vertically on a horizontal plate,” 1876, pp. 261–272.

[2] Eggers, J., and Villermaux, E., “Physics of liquid jets,” vol. 71, 2008.

[3] Planchon, O., “A Physical Model for the Action of Raindrop Erosion on Soil Microtopography,” vol. 74, 2010.

[4] Minemawari, H., Yamada, T., Matsui, H., Tsutsumi, J., Haas, S., Chiba, R., Kumai, R., and Hasegawa, T., “Inkjet printing of single-crystal films,” *Nature*, vol. 475, 2011, pp. 364–367.

[5] Ghodbane, M., Holman, J. P., and Sutherland, I., “Ex ~~ ri ~ e ~ tai study of spray cooping with Freon- ? 13,” 1990.

[6] Attinger, D., Moore, C. B., Donaldson, A., and Stone, H. A., “Fluid dynamics topics in bloodstain pattern analysis : Comparative review and research opportunities,” 2013.

[7] Antkowiak, A., Audoly, B., and Josserand, C., “Instant fabrication and selection of folded structures using drop impact,” vol. I.

[8] Rein, M., “Phenomena of liquid drop impact on solid and liquid surfaces,” vol. 12, 1993, pp. 61–93.

[9] Eggers, J., Fontelos, M. A., Josserand, C., and Zaleski, S., “Drop dynamics after impact on a solid wall : Theory and simulations,” 2010, pp. 1–13.

[10] Raman, K. A., Jaiman, R. K., Lee, T., and Low, H., “International Journal of Heat and Mass Transfer Lattice Boltzmann simulations of droplet impact onto surfaces with varying wettabilities,” *International Journal of Heat and Mass Transfer*, vol. 95, 2016, pp. 336–354.

[11] Lunkad, S. F., Buwa, V. V, and Nigam, K. D. P., “Numerical simulations of drop impact and spreading on horizontal and inclined surfaces,” vol. 62, 2007, pp. 7214–7224.

[12] Choi, M., Son, G., and Shim, W., “Numerical simulation of droplet impact and evaporation on a porous surface,” *International Communications in Heat and Mass Transfer*, vol. 80, 2017, pp. 18–29.

[13] Ruiter, J. De, Ende, D. Van Den, and Mugele, F., “Air cushioning in droplet impact . II . Experimental characterization of the air film evolution Air cushioning in droplet impact . II . Experimental characterization of the air film evolution,” vol. 012105, 2015.

[14] Liu, J., Vu, H., Yoon, S. S., Jepsen, R., and Aguilar, G., “SPLASHING PHENOMENA DURING LIQUID DROPLET IMPACT,” vol. 20, 2010, pp. 297–310.

[15] Riboux, G., and Gordillo, J. M., “Experiments of Drops Impacting a Smooth Solid Surface : A Model of the Critical Impact Speed for Drop Splashing,” vol. 024507, 2014, pp. 1–5.

[16] Gao, H., and Rose, J. L., “Ice detection and classification on an aircraft wing with ultrasonic shear horizontal guided waves,” *Ultrasonics, Ferroelectrics and Frequency Control, IEEE Transactions on*, vol. 56, 2009, pp. 334–344.

[17] Visser, C. W., Frommhold, P. E., Wildeman, S., Mettin, R., Lohse, D., and Sun, C., “Soft Matter numerical simulations and experiments at frame-,” *Soft Matter*, vol. 00, 2015, pp. 1–15.

[18] Chr. Mundo, M. Sommerfeld, C. T., “Droplet-Wall Collisions: Experimental Studies of the Deformation and Breakup Process,” vol. 21, 1995.

[19] Rioboo, R., Heat, E., and Sa, P., “Outcomes from a Drop Impact on Solid Surfaces,” 2001.

[20] Statistique, P., and Lhomond, R., “Retraction dynamics of aqueous drops upon impact on non-wetting surfaces,” vol. 545, 2005, pp. 329–338.

[21] Manglik, R. M., Jog, M. A., Gande, S. K., Ravi, V., Manglik, R. M., Jog, M. A., Gande, S. K., and Ravi, V., “Damped harmonic system modeling of post-impact drop-spread dynamics on a hydrophobic surface Damped harmonic system modeling of post-impact drop-spread dynamics on a hydrophobic surface,” vol. 082112, 2013.

[22] Josserand, C., and Thoroddsen, S. T., “Drop Impact on a Solid Surface,” pp. 365–393.

[23] Li, H., Waldman, R. M., and Hu, H., “An Experimental Investigation on Unsteady Heat Transfer and Transient Icing Process upon Impingement of Water Droplets,” 2016, pp. 1–18.

[24] Liu, Y., Chen, W., Bond, L. J., and Hu, H., “An experimental study on the characteristics of wind-driven surface water film flows by using a multi-transducer ultrasonic pulse-echo technique An experimental study on the characteristics of wind-driven surface water film flows by using a multi-transducer ultrasonic pulse-echo technique,” vol. 012102, 2017.

[25] Hu, H., Wang, B., and Zhang, K., “Quantification of transient behavior of wind-driven surface droplet / rivulet flows using a digital fringe projection technique,” *Journal of Visualization*, 2015, pp. 705–718.

[26] Dai, J., Li, B., and Zhang, S., “High-quality fringe pattern generation using binary pattern optimization through symmetry and periodicity,” *Optics and Lasers in Engineering*, vol. 52, 2014, pp. 195–200.

[27] Zhang, K., Wei, T., and Hu, H., “An experimental investigation on the surface water transport process over an airfoil by using a digital image projection technique,” *Experiments in Fluids*, vol. 56, 2015, p. 173.

[28] Lee, J. B., Derome, D., Dolatabadi, A., and Carmeliet, J., “Energy Budget of Liquid Drop Impact at Maximum Spreading: Numerical Simulations and Experiments,” 2016.

[29] Banks, D., Ajawara, C., and Sanchez, R., “EFFECTS OF LIQUID AND SURFACE CHARACTERISTICS ON OSCILLATION BEHAVIOR OF DROPLETS UPON IMPACT,” vol. 24, 2014, pp. 895–913.

CHAPTER 7
CONCLUSIONS AND FUTURE WORK

7.1 Conclusions

In this chapter, the major accomplishments achieved in this dissertation were summarized and discussed below. There are total of five topics: in-flight droplet temperature, velocity and size measurement; the effects of surface hydrophobicity on the icing process of impacting droplets; quantification of dynamic droplets onto solid surface; impact droplet maximum spreading diameter model; damped harmonic oscillator model of oscillating stage during droplet impact process.

7.1.1 In-flight Droplet Temperature, Velocity and Size Measurement

We presented the progress made in developing a molecular tagging technique for achieving simultaneous measurements of droplet size, flying velocity and transient temperature of in-flight liquid droplets. Phosphorescent 1-BrNp·Mβ-CD·ROH triplex molecules, which can be turned into long-lasting glowing marks upon excitation by photons of appropriate wavelength, were used as the molecular tracers for the quantitative measurements. A pulsed UV laser was used to 'tag' the phosphorescent triplex molecules premixed within in-flight droplets to emit long-lived laser-induced phosphorescence (LIP). After the same laser excitation pulse, the tagged phosphorescent triplex molecules were imaged at two successive times within the phosphorescent lifetime of the tracer molecules. While the size of the in-flight droplets was determined quantitatively based on the acquired droplet images with a pre-calibrated scale ratio between the image plane and the

object plane, the displacements of the droplets between the two image acquisitions were used to estimate the flying velocity of the in-flight droplets. The transient temperature of the in-flight droplets was derived simultaneously by taking advantage of the temperature dependence of the phosphorescence lifetime, which is estimated from the phosphorescence intensity ratio of the two interrogations.

The feasibility and implementation of the molecular tagging technique was demonstrated by conducting simultaneous measurements of droplet size, flying velocity and transient temperature of micro-sized water droplets exhausted from a piezoelectric droplet generator at different test conditions. During the experiments, while the ambient air temperature was kept constant at 22°C, the initial temperature of the micro-sized water droplet at the droplet generator exit was set at a lower temperature range from 11°C to 18°C. After injected into the ambient air, the micro-sized water droplets were convectively heated up as they flew through the ambient air, which caused the transient temperature of the micro-sized water droplets to vary dynamically along their flight trajectories. The unsteady heat transfer process between the in-flight water droplets and the ambient air were also analyzed theoretically by using the Lumped Capacitance method to predict the temperature of the in-flight water droplets along their flight trajectories. The measured temperature data was compared quantitatively with the theoretical analysis results, and the discrepancies between the measured temperature data and the theoretical prediction results were found to be within 0.80˚C.

7.1.2 The Effects of Surface Hydrophobicity on the Icing Process of Impacting Droplets

Droplets with different impact velocities impacted on the hydrophilic and superhydrophobic substrates under normal and icing temperature was investigated experimentally by using high-speed image and infrared image techniques. The morphologic change of the impact droplet, the phase change of icing, and the heat transfer during the impact process were analyzed based on the experimental results.

When droplet impact on superhydrophobic surface, the time needed for the droplet to be static is much shorter than that on hydrophilic surface, while the time needed for cooling the droplet is much longer than those on hydrophilic surface. When droplet impact on the icing temperature surfaces, the droplets upper surface temperature would decrease gradually, while obvious temperature fluctuation was observed on the droplets impacting on the hydrophilic surfaces.

Compare with that on the superhydrophobic surface, the substrate temperature can severely influence the droplet impact and icing process on the hydrophilic surface. When droplet impact on superhydrophobic surface, the bottom of the droplet would recede to a smaller diameter before icing, while it wouldn’t on hydrophilic surface. With a bigger heat transfer area, the cooling speed on hydrophilic surface was much faster.

Compare with that on superhydrophobic surface, droplet impact velocity can severely influence the droplet impacted on the hydrophilic surface. With the increasing of the impact velocity, the bottom area of the droplet would increase, thus, the cooling speed would increase as well.

7.1.3 Quantification of Dynamic Droplets onto Solid Surfaces

In the present study, an experimental investigation was conducted to quantify the shape evolution of the droplet during the impact process on solid surface in order to elucidate underlying physics to improve our understanding of the important microphysical processes pertinent to aircraft icing phenomena. A digital image projection (DIP) technique was used to achieve time-resolved measurements of the droplet thickness during the entire droplet impact process, including the spreading, receding and oscillating stages. By comparing the droplet shape evolution under different impact velocities, the dynamics of droplet impact under different Weber numbers or Reynolds numbers were analyzed in detail.

By comparing the droplet volume measure by digital image projection technique during the impact process with the droplet volume calculated based on the initial diameter of the droplet before contacting on the surface, the digital image projection technique measurement error and uncertainty was validated. The compared result shows that the measurement error of the technique is less than 5%, while the measurement uncertainty is less than 2%.

Based on the time-resolved droplet film thickness, the droplet impact on a solid surface could be divided into three distinct stages: the spreading stage, which begins when the droplet first contacts the surface and ends when the droplet center reaches the minimum thickness; the retracting stage, which begins following the end of the spreading stage and ends when the droplet center achieves a secondary maximum thickness; and the oscillating stage, which begins following the end of the receding stage and ends when the

droplet finally comes to rest on the solid surface. The three successive regimes, i.e., pressure impact regime, self-similar inertial regime and the plateau regime during the spreading stage investigated in previous studies was verified in present study.

By comparing the droplet shape evolution under different impact velocities, it was found that with the increase of the impact velocity, Weber and Reynolds number, the maximum spreading diameter of the droplet would increase, as would with the spreading speed. Additionally, the droplet has a plateau at the center under high Weber number conditions, while under the low Weber condition, no plateau was observed. Also, with a much longer oscillation stage compared with the higher Weber number cases, the total time for the droplet to finish the impact process under the lower Weber number condition is longer. The oscillating stage was simulated by a damped harmonic oscillator, and shows good agreement with the experimental results. It found that the oscillating stage on hydrophilic surface is different from that on hydrophobic surface, with the increase of the impact velocity, or Reynolds number, the time needed for the oscillator to be finally rest become shorter.

7.1.4 Impact Droplet Maximum Spreading Diameter Model

In the present study, a digital image projection (DIP) technique was imported to measure the 3D shape of the droplet during the impact process. To measure the bottom or the blocked part' shape of the droplet during the spreading stage including the state when the droplet reaches the maximum spreading diameter, a side-view measurement was used. The comparison results between the volume calculated based on the 3D shape measured by combining DIP technique and side-view technique and the volume calculated by the

initial size of the droplet before impact show that the using of the DIP technique in present study is reasonable, and the side-view technique can reduce the measurement error caused by the blocking effect. The relative mean error of the droplet volume during whole impact process was 2.56%, while the standard deviation was 0.94%.

Based on the precise droplet shape by combining the DIP technique and side-view results, a surface area factor representing the relationship between droplet upper surface area (surface between liquid droplet and air) and bottom surface area (surface between liquid droplet and solid surface) was proposed. The analysis results shows that the factor has a linear relationship with $WeRe^{1/2}$ under logarithmic coordinate system. By applying this factor in the droplet maximum spreading diameter model in the previous study, a revised model was developed.

By using the precise surface area calculated directly from measured results, the revised model can sufficiently reduce the prediction error caused by the shape assumption in the energy balance analysis. To validate the prediction precise, the predicted results were compared with the experimental data in present study and that in several previous researches, meanwhile, several prediction models proposed in previous studies were analyzed as well. Based on the comparison results with the experimental data and with other models, the revised model in present study can predict the maximum spreading diameter in a wide range of Weber number and Reynolds number ($1<We<2300$, $130<Re<35000$) reasonablely, especially under low Weber number and low Reynolds number droplet impact conditions ($We<50$, $Re<3000$).

7.1.5 Damped Harmonic Oscillator Model of Oscillating Stage during Droplet Impact Process

In the present study, a digital image projection (DIP) technique was imported to measure the droplet upper surface central height during the impact process. Compare with the “side view” technique, the DIP technique could measure the central height when the droplet central part was lower than the outside part, while the “side view” technique would fail to obtain the central part information.

Based on the measurement results, it found that the oscillating dynamics under low Weber conditions ($20 < We < 40$) are different from that under high Weber number conditions. A damped harmonic oscillator model was proposed based on the experimental results under low Weber number conditions, and the comparison results shew that the model can do precise prediction in this region. To precisely predict the droplet oscillating dynamics under high Weber conditions, further investigations were needed to be done, and a new model was desired.

7.2 Future Work

Based on the research accomplishments as discussed above, the following recommendations are made:

1) In present study, the molecular tagging technique has been developed to measure an in-flight droplet temperature. However, all the temperature measured is normal temperature (higher than zero Celsius). If it was needed to measure a supercooled droplet temperature (lower than zero Celsius), a novel calibration method which can find the relationship between the phosphorescence lifetime and the subzero temperature is desired.

2) In present study, all the droplets tested were normal temperature, however, the real droplet aircraft encountered is supercooled droplet, thus, to simulate the aircraft icing more real, a novel supercooled droplet generator was desired.

3) In present study, for increasing the light scattering on the impact droplet surface, the pure water droplet was replaced by 5% latex (volume) mixture. Although the test shew that the mixture still performed Newtonian fluids characteristics, the added adulterant may lead to the failure simulation of pure water icing. Thus, a new method which can measure pure water shape is desired.

4) In present study, a damped harmonic oscillator model was proposed to predict the dynamics during the oscillating stage of the droplet impact process, however, it can only precisely predict those when the droplet Weber number is small (< 40), for those conditions when the Weber number is bigger, a new model is needed.